UNIVERSIDADE FEDERAL DE SANTA CATARINA
DEPARTAMENTO DE FÍSICA
PROGRAMA DE PÓS-GRADUAÇÃO EM FÍSICA

Thomas Häffner

Estudo do limite quântico da termodinâmica empregando emaranhamento fotônico

Florianópolis
2022

Thomas Häffner

Estudo do limite quântico da termodinâmica empregando emaranhamento fotônico

Tese submetida ao Programa de Pós-graduação em Física da Universidade Federal de Santa Catarina para a obtenção do título de Doutor em Física.

Orientador: Prof. Dr. Paulo Henrique Souto Ribeiro.

Ficha de identificação da obra elaborada pelo autor,
através do Programa de Geração Automática da Biblioteca Universitária da UFSC.

Häffner, Thomas
Estudo do limite quântico da termodinâmica empregando emaranhamento fotônico / Thomas Häffner ; orientador, Paulo Henrique Souto Ribeiro, 2022.
117 p.

Tese (doutorado) - Universidade Federal de Santa Catarina, Centro de Ciências Físicas e Matemáticas, Programa de Pós-Graduação em Física, Florianópolis, 2022.

Inclui referências.

1. Física. 2. Ótica quântica. 3. Termodinâmica quântica. 4. Momento Angular Orbital da Luz. I. Souto Ribeiro, Paulo Henrique. II. Universidade Federal de Santa Catarina. Programa de Pós-Graduação em Física. III. Título.

Thomas Häffner

Estudo do limite quântico da termodinâmica empregando emaranhamento fotônico

O presente trabalho em nível de doutorado foi avaliado e aprovado por banca examinadora composta pelos seguintes membros:

Prof. Dr. Daniel Schneider Tasca
Universidade Federal Flumenense

Prof. Dr. Renné Luiz Câmara Medeiros de Araújo
Universidade Federal de Santa Catarina

Prof. Dr. Eduardo Inacio Duzzioni
Universidade Federal de Santa Catarina

Prof. Dr. Luis Guilherme de Carvalho Rego
Universidade Federal de Santa Catarina

Certificamos que esta é a **versão original e final** do trabalho de conclusão que foi julgado adequado para obtenção do título de Doutor em Física.

Documento assinado digitalmente
Paulo Henrique Souto Ribeiro
Data: 25/05/2022 15:22:18-0300
CPF: 730.886.506-10
Verifique as assinaturas em https://v.ufsc.br

Coordenação do Programa de
Pós-Graduação

Documento assinado digitalmente
Paulo Henrique Souto Ribeiro
Data: 25/05/2022 15:22:49-0300
CPF: 730.886.506-10
Verifique as assinaturas em https://v.ufsc.br

Prof. Dr. Paulo Henrique Souto Ribeiro
Orientador

Florianópolis, 2022.

ACKNOWLEDGMENTS

I would first like to thank my advisor Prof. Dr. Paulo Henrique Souto Ribeiro, for all the help and advice over the last seven years of our collaboration.

I would like to thank everyone else that helped me in the process of producing this work such as everyone from the optics lab, especially Guilherme Luiz Zanin for our fruitful cooperation.

I would also like to thank my wife Maria Fernanda Ramos Lento for always having my back and supporting me. In the same way I'd like to thank my parents-in-law.

Finally I want to thank my parents and family for unfailing support and encouragement throughout the many years of study in order to reach this far and writing this thesis. This accomplishment would not have been possible without them. Thank you.

I thank FAPESC for financial support during my PhD.

RESUMO

Quando os sistemas ficam menores, efeitos quânticos , como flutuações, tornam-se relevantes e não podem ser negligenciados. A termodinâmica quântica e a teoria da informação quântica são áreas de pesquisa e têm demonstrado um crescente interesse teórico e experimental. No entanto, o estudo com configurações experimentais usando sistemas tão pequenos é complicado e instável. Neste trabalho, apresentamos e investigamos um esquema ótico experimental que simula sistemas quânticos. Esta configuração ótica usando fótons únicos é fácil de manipular e estável. Utilizamos o grau de liberdade discreto do momento angular orbital (MAO) para simular auto-estados de energia de um sistema quântico. No processo de conversão descendente paramétrica espontânea, um par de fótons únicos é gerado, que são naturalmente emaranhados em seu MAO. Portanto, bombear um cristal não linear com um feixe de laser no modo Gaussiano cria dois fótons gêmeos altamente correlacionados. Esses fótons gêmeos, chamados de sinal e idler, possuem MAO igual de sinais opostos. Medir esse MAO de um dos fótons prepara remotamente o momento do outro fóton. Mostramos como manipular esses estados preparados remotamente para simular estados térmicos. Modulamos a temperatura de tais distribuições térmicas e aplicamos processos como turbulência aos estados térmicos enquanto analisamos a saída. Mostramos como usar este esquema experimental para investigar a termodinâmica quântica, como a relação de flutuação de Jarzynski.

Palavras-chave: Modos de Laguerre-Gauss, Momento angular orbital da luz, Conversão Paramétrica Descendente Espontânea, Termodinâmica Quântica

RESUMO ESTENDIDO

Introdução - O início da Teoria Quântica foi marcado pela descrição da radiação do corpo negro de Max Planck [1]. A explicação de Planck da distribuição espectral da energia irradiada por fontes térmicas era que a energia era trocada em múltiplos da hoje chamada *constante de Planck* $\hbar$ vezes a frequência angular ω, em contraste com a teoria amplamente aceita de que energia era uma variável contínua. Isso levou ao conceito de quantização da luz e, portanto, o *fóton*, o quantum de luz. Isso também foi confirmado pelo efeito fotoelétrico, descoberto por Einstein em 1905, que lhe rendeu o Prêmio Nobel [2]. Enquanto a descrição de partículas e ondas vem da mecânica clássica, a dualidade partícula-onda é um dos fundamentos da mecânica quântica. Isso mostra a conexão fundamental entre a radiação eletromagnética e a mecânica quântica. Por exemplo, luz foi utilizada para mostrar efeitos como interferência de partícula única [3]. Experimentos utilizando luz não foram usados apenas para descobrir novos fenômenos, mas também para provar avanços teóricos na física.
A invenção do laser no início dos anos 60 [4] desencadeou um novo campo de estudos ópticos, chamado de óptica não-linear. Antes as fontes de luz utilizadas para os experimentos eram principalmente a luz térmica, que possui uma baixa densidade de intensidade e um amplo espectro de frequência. Os feixes de laser, por outro lado, tinham um espectro de frequência estreito, um alto grau de coerência e uma alta densidade de energia em uma pequena direção angular bem definida. Isso possibilitou estudar os chamados efeitos não-lineares em meios não-lineares, que só se tornam significativos para campos de luz de alta intensidade. Avanços na Ótica Quântica e Não-linear juntamente com a invenção do LASER como fonte de luz e o estudo de materiais não-lineares permitiram a observação e controle das propriedades quânticas da luz [5]. Um dos efeitos não-lineares mais importantes em ótica quântica é o processo de Conversão Paramétrica Espontânea Descendente (CPDE), que começou a ser investigado uma década após a invenção do laser [6, 7]. Este processo produz um par de fótons únicos com alto grau de correlação e propriedades quânticas. Este processo tornou-se uma das fontes mais utilizadas de *luz quântico* e uma importante ferramenta para experimentos em mecânica quântica. Os dois fótons produzidos no processo de CPDE, chamados *signal* e *idler*, possuem propriedades que não podem ser descritas pela ótica não-linear clássica e exigem uma descrição quântica. Uma dessas propriedades quânticas é o *emaranhamento* entre partículas quânticas como fótons, descrito pela primeira vez por Einstein,

Podolsky e Rosen [8]. Em seu *experimento mental*, eles definiram um sistema quântico (estados EPR) consistindo em dois subsistemas. Esses dois subsistemas interagiram de forma que seu momento e posição permanecem correlacionados mesmo depois de se separaram espacialmente, levando à suposição de não-localidade. Os dois fótons criados no processo de CPDE são, por exemplo, emaranhados no tempo, espaço, momento, energia e polarização [7, 9, 10, 11, 12, 13]. Uma outra propriedade quânticas é o momento angular orbital (MAO) [14, 15]. Foi demonstrado que podemos emaranhar dois ou mais fótons nesse grau de liberdade e que fótons de signal e idler são naturalmente emaranhados em seu MAO [16, 17].

Poynting sugeriu que a luz circularmente polarizada carrega um momento angular [18], o que levou à descoberta do momento angular de spin de $\pm\hbar$ por fóton. Mais tarde, o MAO de $\ell\hbar$ por fóton foi descoberto por Allen *et al.* [19]. Feixes de luz que transportam tal MAO têm frentes de fase entrelaçadas helicoidal ℓ definindo o MAO de cada fóton. A família natural de modos carregando um MAO é a família de modos Laguerre-Gaussianos. Como o MAO é um grau de liberdade discreto e de dimensão infinita, é adequado para aplicações em comunicações clássicas e quânticas, entre outras [20, 21].

Embora os estudos da mecânica quântica tenham visto grandes avanços no último século, a Termodinâmica Quântica [22] é um campo em crescimento que tenta investigar as conexões entre a Termodinâmica e as teorias Clássica e da Informação Quântica. Podemos ver avanços nas investigações teóricas neste campo da física, enquanto as plataformas experimentais e os experimentos ainda são raros. Como mencionamos, já é possível manipular e controlar muitos dos graus de liberdade da luz quântica devido à tecnologia disponível e aos avanços nos últimos anos. Portanto, um esquema experimental totalmente ótico parece uma escolha promissora para a exploração de fenômenos termodinâmicos quânticos [23]. Especificamente, o grau de liberdade MAO foi recentemente usado [24, 25] para demonstrar o protocolo de duas medidas para estudar a versão quântica da relação de flutuação de Jarzynski [26, 27]. Foi então um passo natural fazer uso de correlações quânticas e coerência na luz para estudar o análogo em Termodinâmica Quântica [28, 29, 30].

Neste trabalho, usamos o processo de CPDE para gerar pares de fótons que estão naturalmente emaranhados em seu grau de liberdade de MAO. Mostramos como usar a analogia entre a equação de Schrödinger e a equação paraxial de Helmholtz para simular sistemas quânticos. Em seguida, usamos esse emaranhamento para preparar remotamente um estado térmico de fótons únicos. *Estados térmicos* são emitidos por uma grande variedade de fontes de luz, como luz solar, luz do fogo e

lâmpadas incandescentes. Um estado térmico é caracterizado pelo número de fótons em um modo ótico [31]. O que demonstramos aqui, por outro lado, é a preparação de estados de fótons únicos anunciados apresentando estatísticas térmicas. Tomando as estatísticas da população de fótons de modos óticos de estados térmicos, aplicando-a à probabilidade de população de modos de MAO. Em vez de um único modo ótico com vários fótons, como é usual na Ótica Quântica, lidamos com fótons únicos ocupando vários modos. A preparação remota de tais estados de fótons únicos exibindo estatísticas térmicas pode se tornar uma ferramenta e recurso útil para o estudo experimental da Termodinâmica Quântica. Mostramos a utilidade de tais estados explorando a liberdade e acessibilidade no processo de geração de tais estados e analisamos alguns processos aplicados a esses estados térmicos. Além disso, usamos nosso esquema para produzir remotamente um estado térmico possuindo coerências, um estado térmico *coerente*. Esses estados possuem as mesmas estatísticas de população que um estado de Gibbs, ao mesmo tempo em que apresentam coerências entre os modos ocupados.

Objetivos - O principal objetivo deste trabalho é o estudo experimental da Termodinâmica Quântica. Para este fim, queremos criar uma plataforma experimental para tais investigações, utilizando sistemas fotônicos. Para esses experimentos queremos utilizar fótons gêmeos produzidos na conversão paramétrica descendente espontânea preparados em estados emaranhados. Os estados emaranhados podem ser preparados em vários graus de liberdade dos fótons. Trabalharemos com o emaranhamento no momento angular orbital e na polarização dos fótons. Usando a analogia entre a equação de Schrödinger e a equação paraxial de Helmholtz queremos simular sistemas quânticos. Com isso é possível preparar remotamente estados térmicos no grau de liberdade de MAO. Testaremos as relações de flutuação dissipação de Jarzynski e Crooks incluindo a informação relativa ao emaranhamento. Testaremos também a geração de entropia em processos aplicados a esses estados térmicos.

Metodologia - Todos experimentos desse trabalho foram realizados nos laboratórios da UFSC em Florianópolis. Nesses experimentos um diodo laser é usado para bombear um cristal birrefringente e criar pares de fótons gêmeos no processo de CPDE. Esses fótons são direcionados a um modulador espacial de luz para mudar a ordem de modo Laguerre-Gaussiano. Antes de ser detectado por um contador de fótons únicos, os feixes são acoplados a fibras óticas monomodos que somente acoplam modos Gaussianos de ordem zero, que têm MAO nulo. Usando o SLM para mudar o valor do MAO até chegar em zero, podemos medir o valor do MAO dos feixes

signal e idler, uma vez que a variação de MAO necessária para levar o estado para MAO nulo é igual ao MAO inicial com sinal trocado. Utilizamos o emaranhamento de MAO entro os fótons signal e idler para preparar estados térmicos de um fóton unico remotamente. O modular de luz foi usado para simular processos como turbulência aplicados a esses estados térmicos, que nos permite a verificação da relação de flutuação dissipação de Jarzynski, por exemplo.

Resultados obtidos - Nesta tese simulamos sistemas quânticos utilizando sistemas fotônicos. Apresentamos uma plataforma experimental para a investigação da Termodinâmica Quântica. Mostramos como preparar remotamente um estado térmico utilizando o MAO como grau de liberdade e a analogia entre a equação de Schrödinger e a equação paraxial de Helmholtz. Também foi demonstrando como aplicar processos como turbulência atmosférica a esses estados. Os efeitos desse processo aos estados térmicos como mudança de energia e entropia foram investigado. A relação de flutuação de Jarzynski generalizada foi confirmada.

Palavras-chave: Modos de Laguerre-Gauss, Momento Angular Orbital da Luz, Conversão Paramétrica Descendente Espontânea, Termodinãmica Quântica

ABSTRACT

When systems get smaller, quantum effects, like fluctuations, become relevant and cannot be neglected. Quantum thermodynamics and quantum information theory are active areas of research and have shown an increased theoretical and experimental interest. However the study with experimental setups using such small systems are complicated and unstable. In this work, we present and investigate an experimental optical scheme that emulates quantum systems. This optical setup using single photons is easy to manipulate and stable. We utilize the discrete orbital angular momentum (OAM) degree of freedom to simulate energy eigenstates of a quantum system. In the process of spontaneous parametric down-conversion, a pair of single photons is generated, which are naturally entangled in their OAM. Therefore, pumping a non-linear crystal with a laser beam in a Gaussian mode creates two highly-correlated twin photons. These twin photons, called signal and idler, possess equal OAM of opposite signs. Measuring this momentum of one of the photons remotely prepares the momentum of the other photon. We show how to manipulate these remotely prepared states in order to simulate thermal states. We modulate the temperature of such thermal distributions and apply processes like turbulence to the thermal states while analyzing the output. We show how to use this experimental scheme to investigate quantum thermodynamics, like the Jarzynski fluctuation relation.

Keywords: Laguerre-Gaussian modes, Orbital angular momentum of light, Spontaneous Parametric Down-Conversion, Quantum Thermodynamics

List of Figures

Contents

1. Introduction

The beginning of Quantum Theory was marked by Max Planck's description of black body radiation [1]. His explanation of the spectral distribution of energy radiated by thermal sources was that energy was exchanged in multiples of the nowadays called *Planck's constant* $\hbar$ times the angular frequency ω, in contrast to the widely accepted theory that energy was a continuous variable. This led to the concept of the quantization of light and therefore the *photon*, the quantum of light. This was also confirmed by the photoelectric effect, discovered by Einstein in 1905, which won him the Nobel Prize [2]. While the description of particles and waves comes from classical mechanics, the particle-wave-duality is one of the foundations of quantum mechanics. This shows the fundamental connection between electromagnetic radiation and quantum mechanics as, for example, light was utilized to show such effects as single-particle interference [3]. Experiments utilizing light have not only be used to discover new phenomena but also to prove theoretical advances in physics.
The invention of the laser in the beginning of the 60s [4] sparked a new field of optical studies, called non-linear optics. Before the light sources used for experiments were mainly thermal light, which has a low intensity density and a broad frequency spectrum. Laser light beams, on the other hand, had a narrow frequency spectrum, a high degree of coherence and a high energy density in a small well-defined angular direction. This made it possible to study non-linear effects, which only become significant for high intensity light fields. Advances in quantum and non-linear optics together with the invention of the LASER as a light source and the study of non-linear materials have allowed the observation and control of the quantum properties of light [5]. One of the most important non-linear effects in quantum optics is the process of Spontaneous Parametric Down-Conversion (SPDC), which started to be investigated a decade after the invention of the laser [6, 7]. This process produces a pair of single photons with a high degree of correlation and quantum properties. This process became one of the most widely used sources of *quantum light* and a important tool for experiments on quantum mechanics. The two photons produced in the process of SPDC, called *signal* and *idler*, have properties that cannot be described by classical non-linear optics and demand a quantum description. One of those quantum properties is the *entanglement*

between quantum particles like photons, first described by Einstein, Podolsky and Rosen [8]. In their Gedanken experiment, they defined a quantum system (EPR states) consisting of two subsystems. Those two subsystems interacted in a way that their momentum and position remain correlated even after they become spatially separated, leading to the assumption of non-locality. The two down-converted photons created in the process of SPDC are, for example, entangled in time, space, momentum, energy and polarization [7, 9, 10, 11, 12, 13]. Another one of those quantum properties is the orbital angular momentum (OAM) [14, 15]. It has been shown that we can entangle two or more photons in the OAM degree of freedom and that signal and idler photons are naturally entangled in their OAM [16, 17].

Poynting suggested that circularly polarized light carries an angular momentum [18], which led to the discovery of the spin angular momentum of $\pm\hbar$ per photon. Later the OAM of $\ell\hbar$ per photon was discoverd by Allen *et al.* [19]. Light beams that carry such an OAM have ℓ helical intertwined phase fronts defining the OAM of each photon. The natural family of modes carrying an OAM is the family of Laguerre-Gaussian modes. As the OAM is a discrete and infinite dimension degree of freedom, it is suited for applications in classical and quantum communications, among others [20, 21].

While the studies of quantum mechanics have seen vast advances over the last century, Quantum Thermodynamics [22] is a growing field that tries to investigate the connections between Thermodynamics and Classical and Quantum Information theories. We can see progress in theoretical investigations in this field of physics, while the experimental platforms and experiments are still rare. As we mentioned, it is already possible to manipulate and control many of the degrees of freedom of quantum light due to the available technology and advances in the past years. Therefore, an all-optical experimental scheme seems a promising choice for the exploration of quantum thermodynamic phenomena [23]. Specifically, the OAM degree of freedom was recently used [24, 25] to demonstrate the two-measurement protocol for studying the quantum version of Jarzynski's fluctuation relation [26, 27]. It was then a natural step forward to make use of quantum correlations and coherence in light to study the analogous in Quantum Thermodynamics [28, 29, 30].

In this work, we use the process of spontaneous parametric down-conversion to generate pairs of photons that are naturally entangled in their OAM degree of freedom. We show how to use the analogy between the Schrödinger's equation and the paraxial Helmholtz equation to simulate quantum systems. We then use this entanglement to remotely prepare a single-photon thermal state. *Thermal states* are emitted by a big range of light sources such as sunlight, firelight, and incandescent light bulbs. A thermal

state is characterized by the number of photons in an optical mode [31]. What we demonstrate here, on the other side, is the preparation of heralded single photon states presenting thermal statistics. Taking the statistics of the photon population of optical modes from thermal states, applying it to the population probability of OAM modes. Instead of an optical single mode with several photons, as it is usual in Quantum Optics, we deal with single photons populating several modes. The remote preparation of such single photon states exhibiting thermal statistics might become a useful tool and resource for the experimental study of Quantum Thermodynamics. We show the utility of such states by exploring the freedom and accessibility in the process of generating such states and analyzing a few processes applied to these thermal states. Further, we use our scheme to remotely produce a thermal-like state possessing coherences, a *coherent* thermal state. These states possess the same statistics of populations as a Gibbs state while having also coherences between the occupied modes.

List of Publications

- **T. Häffner**, G. L. Zanin, R. M. Gomes, L. C. Céleri, and P. H. S. Ribeiro, "Remote preparation of single photon vortex thermal states," The European Physical Journal Plus, vol. 135, p. 601, Jul 2020.
- P. H. S. Ribeiro, **T. Häffner**, G. L. Zanin, N. R. da Silva, R. M. de Araújo, W. C. Soares, R. J. de Assis, L. C. Céleri, and A. Forbes, "Experimental study of the generalized jarzynski fluctuation relation using entangled photons," Phys. Rev. A, vol. 101, p. 052113, May 2020
- G. L. Zanin, **T. Häffner**, M. A. A. Talarico, E. I. Duzzioni, P. H. S. Ribeiro, G. T. Landi, and L. C. Céleri, "Experimental Quantum Thermodynamics with Linear Optics," Brazilian Journal of Physics, vol. 49, pp. 783–798, Oct 2019.
- R. M. de Araújo, **T. Häffner**, R. Bernardi, D. S. Tasca, M. P. J. Lavery, M. J. Padgett, A. Kanaan, L. C. Céleri, and P. H. S. Ribeiro, "Experimental study of quantum thermodynamics using optical vortices," Journal of Physics Communications, vol. 2, no. 3, p. 035012, 2018.

2. Simulations using Beams of Light

The heart of this work is the analogy between the Schrödinger equation for quantum systems and the paraxial Helmholtz equation for beams of light. In our experiments we want to use beams of light to simulate quantum systems. The propagation of the beam of light is described by the paraxial Helmholtz equation, while the evolution of the quantum system is described by the Schrödinger equation. A well-known solution to the Schrödinger equation is for example the quantum harmonical oscillator. The paraxial Helmholtz equation and its solutions will be presented in the following.

2.1 Paraxial Helmholtz Equation

In the experiments employed in this work, we use specific modes of light to generate the states of interest. To describe the propagation of electric fields and therefore light we have to start with the Maxwell's equations:

$$\nabla \times \boldsymbol{E} = -\mu_0 \frac{\partial \boldsymbol{H}}{\partial t} \tag{2.1}$$

$$\nabla \times \boldsymbol{H} = \epsilon_0 \frac{\partial \boldsymbol{E}}{\partial t} \tag{2.2}$$

$$\nabla \cdot \boldsymbol{E} = 0 \tag{2.3}$$

$$\nabla \cdot \boldsymbol{H} = 0 \,, \tag{2.4}$$

where μ_0 is the permeability of the vacuum and ϵ_0 is the permittivity of the vacuum, $\boldsymbol{E}$ is the electric field and $\boldsymbol{H}$ is the magnetic field. Considering that time and space differentiation is independent, we take the curl of the equations (2.1) and (2.2) and separate $\boldsymbol{E}$ and $\boldsymbol{H}$, yielding:

$$\nabla \times (\nabla \times \boldsymbol{E}) = -\mu_0 \epsilon_0 \frac{\partial^2 \boldsymbol{E}}{\partial t^2} \tag{2.5}$$

$$\nabla \times (\nabla \times \boldsymbol{H}) = -\mu_0 \epsilon_0 \frac{\partial^2 \boldsymbol{H}}{\partial t^2} \,. \tag{2.6}$$

Substituting for the speed of light $c = 1/(\mu_0 \epsilon_0)$ and using the vector identity for a vector field $\boldsymbol{A}$

$$\nabla \times (\nabla \times \boldsymbol{A}) = \nabla(\nabla \cdot \boldsymbol{A}) - \nabla^2 \boldsymbol{A} \ , \tag{2.7}$$

we derive the equations

$$\nabla^2 \boldsymbol{E} = \frac{1}{c^2} \frac{\partial^2 \boldsymbol{E}}{\partial t^2} \tag{2.8}$$

$$\nabla^2 \boldsymbol{H} = \frac{1}{c^2} \frac{\partial^2 \boldsymbol{H}}{\partial t^2} \ . \tag{2.9}$$

These equations (2.8) and (2.9) are valid for each vector component, for example the Cartesian coordinates components, x, y and z components satisfy the equations of the same form. We can write this in a more general fashion for scalar fields as

$$\Delta u - \frac{1}{c^2} \frac{\partial^2 u}{\partial t^2} = 0 \ \ , \tag{2.10}$$

where Δ is the Laplace operator, $\Delta = \partial^2/\partial x^2 + \partial^2/\partial y^2 + \partial^2/\partial z^2$.
This equation is called the wave equation and any solution $u(\boldsymbol{r}, t)$ with position $\boldsymbol{r} = (x, y, z)$ and time t is called a wave function.

Applying one possible solution, which is the monochromatic wavefunction [32]

$$u(\boldsymbol{r}, t) = a(\boldsymbol{r}) e^{-i\omega t}, \tag{2.11}$$

where $a(\boldsymbol{r})$ is a complex amplitude and the frequency ω, this yields the so-called Helmholtz equation:

$$(\Delta + k^2) a(\boldsymbol{r}) = 0, \tag{2.12}$$

with the the wave number $k = \omega/c$.

Considering, that in this work we use a laser as a source of light, we can apply the paraxial approximation. This approximation is valid when a light beam does not diverge or converge too much and the wavevectors $\vec{k}$ of the light wave are approximately parallel to the direction of propagation [33]. We, then, can rewrite the solution to the wave equation (2.11) by defining an envelope function $C(r)$ that varies slowly compared to the propagation direction z. Using this relation and taking the derivative with respect to z we can derive the following inequalities

$$\frac{\partial^2 C}{\partial z^2} \ll \frac{k}{2\pi}\frac{\partial C}{\partial z}$$
$$\Leftrightarrow \frac{\partial^2 C}{\partial z^2} \ll \frac{k^2 C}{4\pi^2}. \tag{2.13}$$

This shows that the second derivative of the envelope varies slowly with the square of the wave number.
Therefore using the solution $a(\boldsymbol{r}) = C(\boldsymbol{r})e^{-ikz}$ for the Helmholtz equation (2.12) and discard terms with $\frac{\partial^2 C}{\partial z^2}$ compared to $k\frac{\partial C}{\partial z}$ or $k^2 C$, we derive the equation

$$\Delta_T C - 2ik\frac{\partial}{\partial z}C = 0, \tag{2.14}$$

where $\Delta_T = \frac{\partial^2 c}{\partial x^2} + \frac{\partial^2 c}{\partial y^2}$ is the transverse Laplace operator.
Equation (2.14) is called the paraxial Helmholtz equation.

2.2 Solutions to the Paraxial Helmholtz Equation

2.2.1 Gaussian beams

One important solution to the paraxial Helmholtz equation is the family of Gaussian beams [33, 34]. We get to this solution by solving the paraxial equation in Cartesian coordinates, where x and y are the transverse degrees of freedom, determining the beam profile, and z is the direction of propagation.

$$C = \frac{c_0}{q(z)}e^{-ik\left(\frac{x^2+y^2}{2q(z)}\right)}, \tag{2.15}$$

where c_0 is a constant, k is the wave number and $q(z)$ is defined as:

$$\frac{1}{q(z)} = \frac{1}{R(z)} - i\frac{\lambda}{\pi w(z)^2}, \tag{2.16}$$

where λ is the wavelength, $R(z)$ is the wavefront radius of curvature and $w(z)$ is the beam width. $R(z)$ can be written as

$$R(z) = z\left(1 + \left(\frac{\pi w_0^2}{\lambda z}\right)^2\right) = z\left(1 + \left(\frac{z_R}{z}\right)^2\right). \tag{2.17}$$

The beam intensity has its peak on the beam axis and decreases by a factor of $1/e^2$ at the radial distance $\rho = \sqrt{x^2 + y^2} = w(z)$ (see Fig. 2.1) where

$$w(z) = w_0 \left(1 + \left(\frac{\lambda z}{\pi w_0^2}\right)^2\right)^{1/2} = w_0 \left(1 + \left(\frac{z}{z_R}\right)^2\right)^{1/2} . \tag{2.18}$$

$w(z)$ has a minimum, and the origin of z is usually defined so that $w(z = 0) = w_0$, where w_0 is called beam waist. $w(z)$ increases with z and reaches $\sqrt{2}w_0$ at $z = z_R$, called the Rayleigh range (illustrated in Fig 2.1).

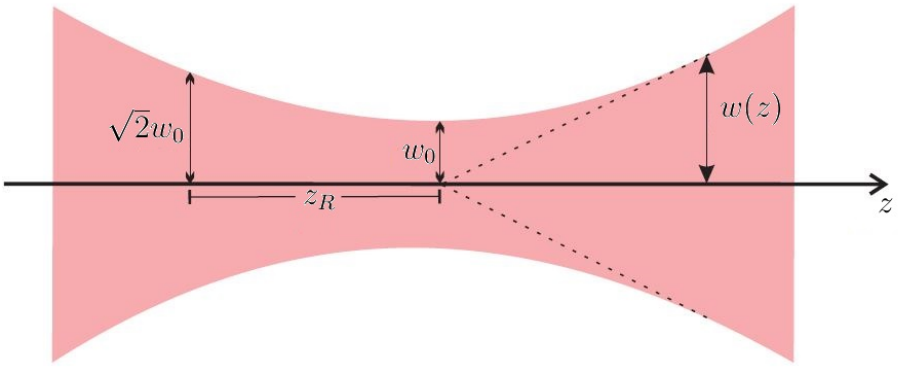

Figure 2.1: Lateral view of a Gaussian beam propagating along z.

Substituting equations (2.16) - (2.18) into equation (2.15), we obtain the expression for the complex amplitude of the Gaussian beams

$$C(\boldsymbol{x}, \boldsymbol{y}, \boldsymbol{z}) = c_0 \frac{w_0}{w(z)} e^{-ik\left(\frac{x^2+y^2}{2R(z)}\right)} e^{-\left(\frac{x^2+y^2}{w^2}\right)} e^{i\Phi(z)} , \tag{2.19}$$

where $\Phi(z)$ is defined as

$$\Phi(z) = \tan^{-1}\left(\frac{z}{z_R}\right) , \tag{2.20}$$

and is called Gouy phase.

2.2.2 Laguerre-Gaussian beams

Another solution to the paraxial equation (2.14) and most relevant for this work is the family of Laguerre-Gaussian beams [19]. This solution is obtained by solving equation (2.14) in cylindrical coordinates. ρ is the radial coordinate and ϕ the azimuth defining the beam profile and z is the direction of propagation. We can write the

complex amplitude in cylindrical coordinates as [35]:

$$LG_{p\ell}(\rho,\phi,z) = c_{p\ell}\frac{w_0}{w(z)}\left(\frac{\sqrt{2}\rho}{w(z)}\right)^{|\ell|} L_p^{|\ell|}\left(\frac{2\rho^2}{w^2(z)}\right)\exp\left(-\frac{\rho^2}{w^2(z)}\right) \exp\left(-i\left(\frac{k\rho^2}{2R(z)} + \left(2p+|\ell|+1\right)\Phi(z)\right)\right)\exp\left(-i\ell\phi\right), \tag{2.21}$$

where $c_{p\ell} = \sqrt{\frac{2p!}{\pi(p+|\ell|)!}}$ and L_p^ℓ are the Laguerre polynomials, defined as

$$L_p^\ell(x) = \frac{x^{-p}e^x}{\ell!}\frac{d^\ell}{dx^\ell}\left(e^{-x}x^{\ell+p}\right). \tag{2.22}$$

Other variables are the same as the ones already defined for the Gaussian beams. The indices p and ℓ are the radial and azimuthal indices respectively. Examples of normalized intensity profiles for the first few orders of LG modes are shown in figure 2.2. The zero-order mode ($\ell = 0, p = 0$) is a Gaussian mode. LG beams with $\ell \neq 0$ have a ring-shaped intensity profile. The index ℓ can take integer values from $-\infty$ to $+\infty$, while the index p only allows non-negative integer values. The intensity profiles for beams with opposite ℓ (for example $\ell = 2$ and $\ell = -2$) have the same intensity profile, they only differ in their phase distribution. Higher orders of p add rings of intensity away from the center of propagation. The azimuthal or rotational index ℓ appears in eq. 2.22 in the Laguerre polynomials, which change the beam size. It also changes the Gouy phase shift and appears in the phase factor $\exp(-i\ell\phi)$. This phase factor advances or retards the beam profile by a phase of $2\pi\ell$ around the axis of propagation (in direction of ϕ). This makes LG beams (except $\ell = 0$) optical vortexes with a topological charge ℓ, which is associated with the orbital angular momentum. Such beams possess a rotational symmetry around their axis of propagation and each photon carries an orbital angular momentum of $i\hbar\ell$ per photon [36].

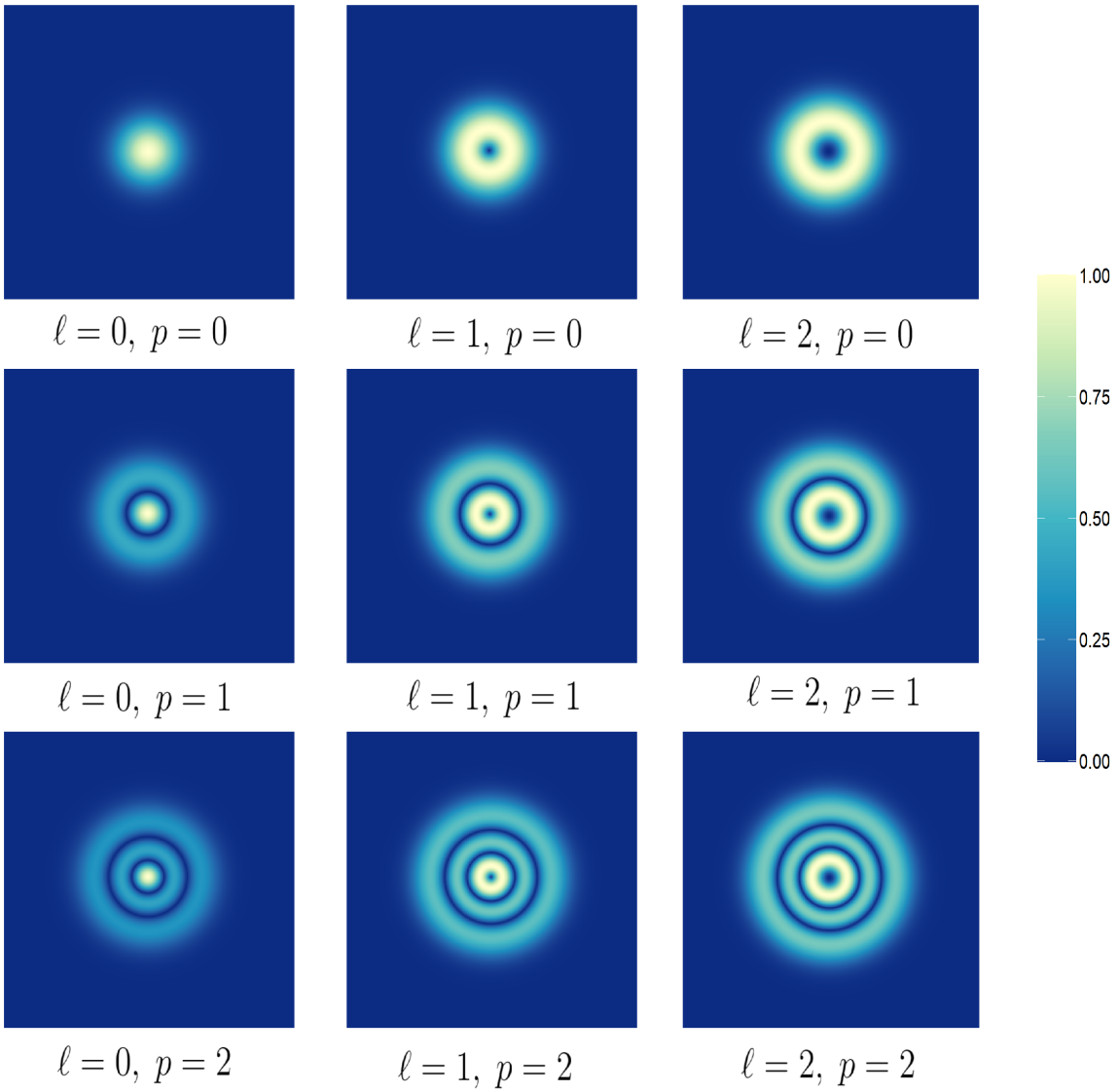

Figure 2.2: Normalized intensity profiles of the first few orders of Laguerre-Gaussian modes [$\ell = (0, 1, 2), p = (0, 1, 2)$]. Intensity profiles for negative indices $\ell < 0$ are the same as the intensity profiles for positive ℓ of the same value ($I(\ell, p) = I(-\ell, p)$.

Each family of optical modes such as LG modes provide a full representation of transverse spatial modes because they are a complete set of orthonormal functions. Each basis can, therefore, be represented in another basis. For example, Hermite-Gaussian modes are another solution to the paraxial equation and superpositions of these modes can represent all LG modes [37]. Another example would be that LG modes are able to fully describe the transverse field of Ince-Gaussian beams [38] and high-order Bessel beams [39], which implies that beams of those familis must also carry an OAM.

2.3 The Orbital Angular Momentum of Light

The special property of the Laguerre-Gaussian modes, which makes them interesting for us for simulation, is the discrete orbital angular momentum that each photon in such a mode carries. This property was discovered by Allen *et al.* in 1992, but the spin angular momentum (SAM) and the orbital angular momentum (OAM) have a long history prior to this.

Light, just like any other electromagnetic radiation has energy and mechanical properties. This was already proposed by Kepler, who suggested that the radiation pressure of light causes the tails of comets. This became evident once Poynting developed the theory of electromagnetic radiation pressure and momentum density in 1905. Einstein and Planck then continued to show the quantization of light and that linear momentum of a photon is $\hbar\mathbf{k}$. Today there are a variety of experiments that use the momentum of light to, for example, trap or cool atoms and molecules [40]. It was again Poynting in 1909 who sparked the research on the momentum of light when he discovered the angular momentum of polarized light, the spin angular momentum, which has the value $\pm\hbar$ for a single photon. This was later measured by showing the torque of light on a suspended half-wave plate in 1936 [41]. The idea of a field of light that has an OAM is not new and was already mentioned in the literature decades ago [42, 43]. But it was almost a century later when Allen *et al.* discovered in 1992 at the Leiden University that beams of light with a helical or twisted wavefront such as LG beams (with $\ell \neq 0$), carry a discrete OAM [19]. To understand the OAM of light we don't even need to consider the concept of photons. We can start with a the description of a electro-magnetic field. We get a direct relation between the linear momentum density

$$\boldsymbol{p} = \varepsilon_0 \boldsymbol{E} \times \boldsymbol{B} \ , \tag{2.23}$$

and the angular momentum density

$$\boldsymbol{j} = \boldsymbol{r} \times \boldsymbol{p} \ , \tag{2.24}$$

where $\boldsymbol{E}$ and $\boldsymbol{B}$ are the electric field and the magnetic field, respectively. Therefore, a angular momentum in the direction of propagation z needs also a component of the electric and magnetic field in the z direction. This means that a theoretically perfect plane waves cannot have an angular momentum. If we follow the analytic analysis of circularly polarized light within the paraxial approximation and integrate the angular momentum and energy density in the $x - y$ plane, we find the ratio of the angular

momentum to energy per unit length of beam [44]

$$\frac{\boldsymbol{J}_z}{\boldsymbol{W}} = \frac{\int\int r\ dr\ d\phi\ (\boldsymbol{r} \times \langle \boldsymbol{E} \times \boldsymbol{B} \rangle)_z}{c \int\int r\ dr\ d\phi \langle \boldsymbol{E} \times \boldsymbol{B} \rangle_z} = \frac{\sigma}{\omega}\,, \tag{2.25}$$

where σ is the spin angular momentum. This leads to the SAM to energy ratio of $\sigma\hbar$ and a SAM of $\pm\hbar$ per photon.
If we now follow the same procedure for a paraxial beam with the phase structure

$$u(r, \phi, z) = u_0(r, z)\mathrm{e}^{\mathrm{i}\ell\phi}\,, \tag{2.26}$$

we will find [45]

$$\frac{\boldsymbol{J}_z}{\boldsymbol{W}} = \frac{\int\int r\ dr\ d\phi\ (\boldsymbol{r} \times \langle \boldsymbol{E} \times \boldsymbol{B} \rangle)_z}{c \int\int r\ dr\ d\phi \langle \boldsymbol{E} \times \boldsymbol{B} \rangle_z} = \frac{\ell}{\omega}\,, \tag{2.27}$$

which gives the angular momentum to energy ratio of $\ell\omega$. Again, assuming the energy of a single photon is $\hbar\omega$, this yields the orbital angular momentum of $\ell\hbar$ per photon, which is independent of the polarization and the SAM [19]. This shows that the easiest definition of a beam of light that carries a OAM is a beam with the phase structure $\phi(r, \phi) = \exp(\mathrm{i}\ell\phi)$.
A natural family of beams of light with such a phase structure are the LG beams introduced in the previous section. While laser beams, usually in Gaussian modes, have spherical wavefronts, the LG beams with $\ell \neq 0$ have the phase factor $\exp(-\mathrm{i}\ell\phi)$, which suggests the existence of a phase vortex at the center of the beam ($\rho = 0$). In Fig. 2.3 is a plot of the phase profiles of the first few orders of LG. The plots shown in Fig. 2.3 are the respective phase profiles of the intensity profiles shown in Fig. 2.2. If we would follow a closed path around the axis of propagation, or around the center in the plots of Fig. 2.2, we would accumulate a phase difference of $2\pi\ell$. We can see that beams with $\ell = 0$ have a zero phase gradient around the center of propagation. For $\ell = 1$ the phase in a transverse plane has a full gradient from 0 to 2π and a beam with $\ell = 2$ has a phase gradient from 0 to 4π, and so on. This phase gradient along a closed circle around the center of the profile determines the OAM of photons or a beam of light in that very LG mode. From the same plots in Fig. 2.3 we can also see that the higher order modes with $p > 0$ don't change this transverse phase gradient. They only add rings with a shifted phase gradient, but if we follow a circular path around the center of the profile we find the same phase difference. This shows that LG modes with $p > 0$ have the same amount of OAM as modes with the same ℓ and $p = 0$.

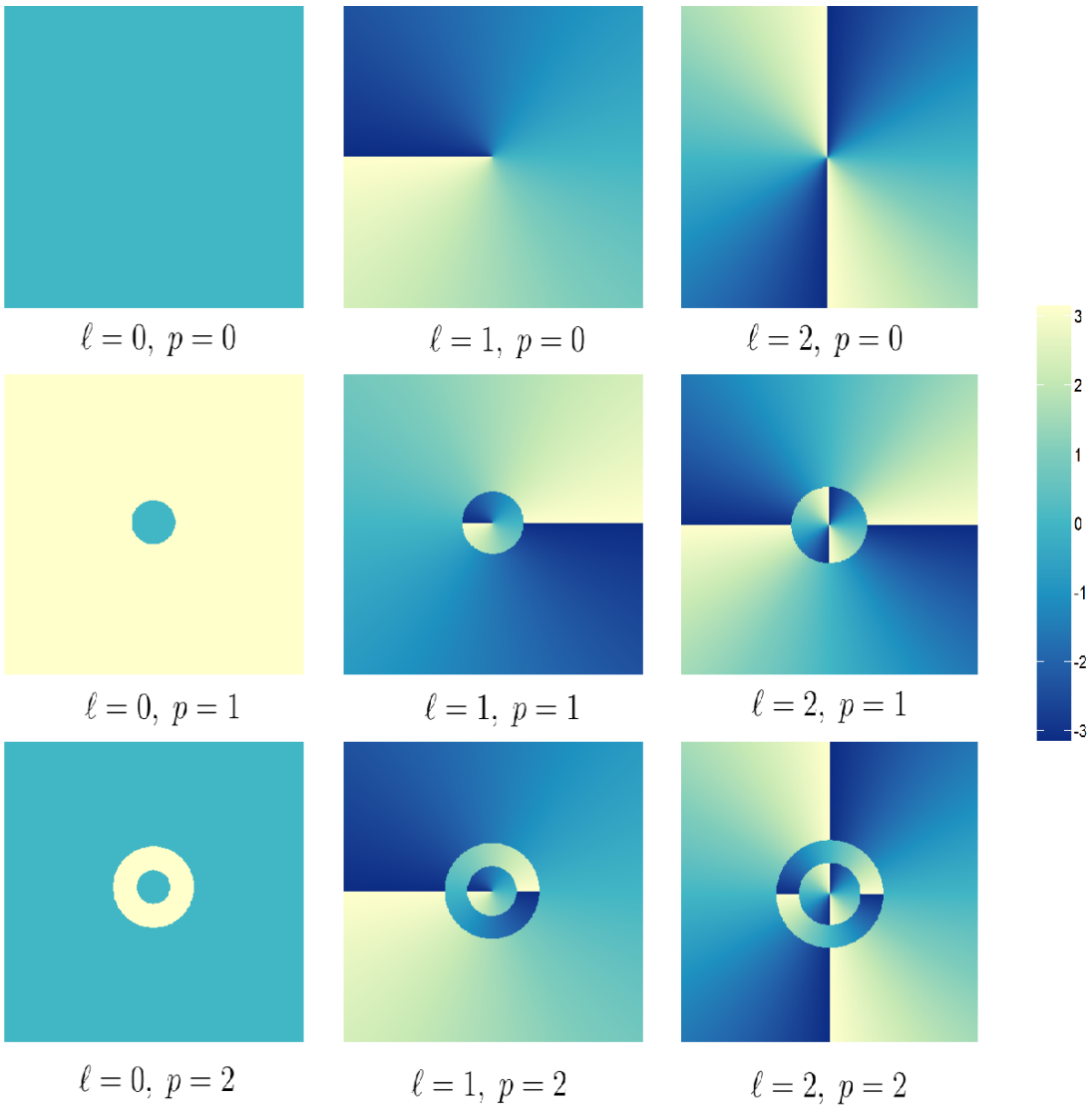

Figure 2.3: Phase profiles in the transverse plane of the first few orders of Laguerre-Gaussian modes [$\ell = (0, 1, 2), p = (0, 1, 2)$]. Each LG mode has a phase gradient from 0 to $\ell \cdot 2\pi$.

The circular phase gradient $\exp(-\mathrm{i}\ell\phi)$ around the axis of propagation of the transverse phase profiles of LG modes give rise to a particular phase structure that results in an intertwined helical wavefront. The wavefront or phase front of a beam of light is a surface of constant phase. In fig. 2.4 is a plot of such planes with equal phase. The plots show that like the circular phase gradient, the amount of intertwined wave fronts is determined by the index ℓ of the respective LG mode. Every LG beam has exactly ℓ intertwined helical phase fronts. The Poynting vector, which is perpendicular to the surface of the phase fronts, has an azimuthal component around the direction of propagation and hence an angular momentum along the beam axis, causing an OAM.

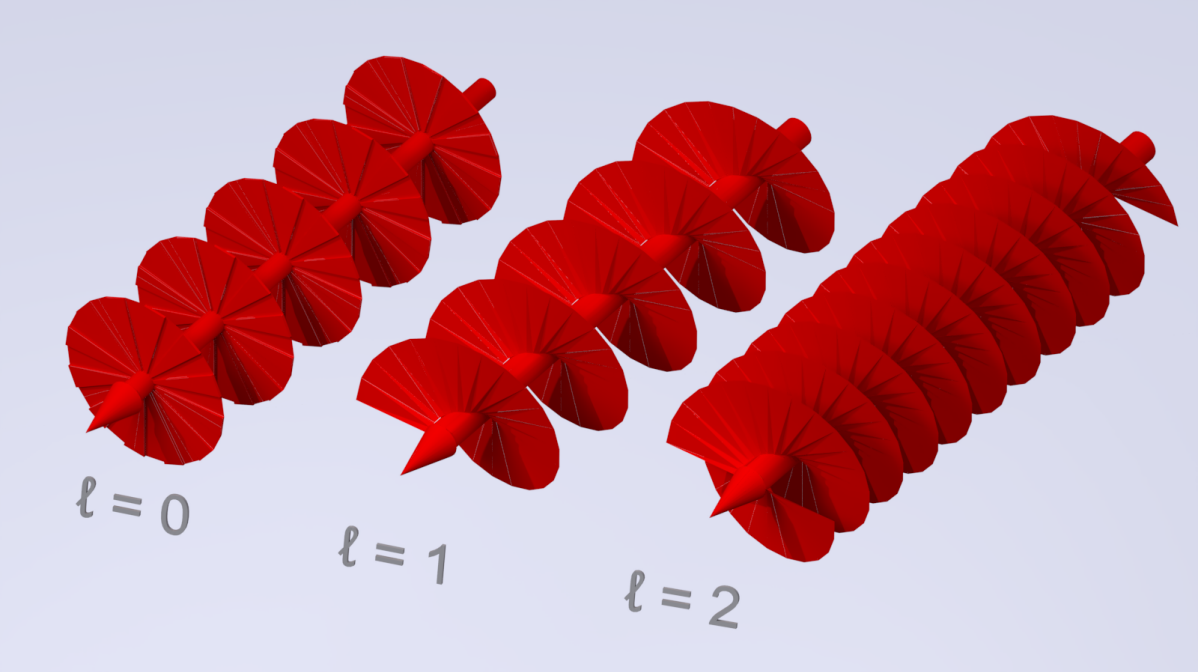

Figure 2.4: Plot of the helical phase fronts for the first orders of LG modes ($\ell = 0$, $\ell = 1$ and $\ell = 2$).

LG beams are not the only example of a family of light modes with such wavefronts. Other examples are Bessel beams [46], Mathieu beams [47] or Ince-Gaussian beams [38]. Beams of these families of optical modes can also carry an OAM. In fact, any vortex beam, a concept developed in the 70s by Nye and Berry [48], that has the phase structure $\exp(-\mathrm{i}\ell\phi)$, possesses OAM, as we have shown here.
The concept of optical OAM is not too new, but what sparked a big growth in this area of research is when Allen *et al.* showed the possibility to rather easily produce light with such a discrete quantized OAM in the laboratory. The light beams we will generate and manipulate in our experiments are described in Chapter 3.2. Those beams only approximate the intensity structure of a LG beam, but generate perfect helical wavefronts and have therefore a discrete OAM per photon. For that reason we will continue referring to them as LG beams in the following. There are several different methods to generate light beams with the necessary azimuthal phase structure to contain OAM. For example, phase plates [49], mode converters that convert Hermite-Gaussian beams into LG beams [35] and forked holograms that generate the OAM in the several orders of diffraction [50]. We will use the method of forked holograms imprinted in a phase modulating display, described in chapter 3.2.
Many advances in the field of OAM of light have been achieved and more and more areas of research are starting to utilize the OAM of light. Optical tweezers use OAM to trap particles and even transfer the OAM to the particle [51]. Ghost imaging was

performed using beams with OAM [52, 53], as well as contrast enhancing microscopy [54, 55] and interferometry [56].

In quantum information processing the polarization of photons was typically used to generate quantum states, superpositions and entanglement. The OAM is another degree of freedom of the photon that is of infinite dimensions and discrete. Therefore the information transmitted with a single-photon can be increased using the OAM degree of freedom [57] and it was even used for multiplexed data transfer [58]. Through the process of spontaneous parametric down-conversion, for example, we can achieve high dimensional entanglement of OAM, (which we will demonstrate in chapter 3.4) making it useful for a variety of quantum protocols. This allows to generate states with high-dimensional entanglement, which are a resource in quantum communication [17, 59]. The high dimensionality is also useful for dense coding and for computation [60].

In this work though, we will apply the OAM degree of freedom of single photons to the simulation of thermal states. We use the entanglement of OAM between two photons to remotely prepare such single-photon states.

The main advantage of the OAM of light for our purpose is the characterization of a light mode through the discrete quantum number ℓ. This index can be measured in the experiment, we can prepare beams with a certain OAM precisely and even create and measure superpositions of light modes determined by their OAM.

As we mentioned before, LG beams are a solution to the paraxial Helmholtz equation in cylindrical polar coordinates (ρ, ϕ, z). From quantum theory is known that a wave function with the azimuthal phase dependence is an eigenstate of the orbital angular momentum operator

$$\hat{L}_z = -i\hbar \frac{\partial}{\partial \phi} \,, \tag{2.28}$$

with the eigenvalue $\ell\hbar$. This *analogy* is not just accidental as we have shown that every photon of a LG mode (or any vortex beam with a $\exp(\mathrm{i}\ell\phi)$ phase structure) carries an OAM of exactly $\ell\hbar$. This analogy lays the foundation for our simulation scheme, which we present in the next chapter.

2.4 Analogy between Schrödinger Equation and paraxial Equation

The fact that photons in LG modes carry OAM and that their wave functions are eigenstates to the OAM operator already lets us guess at a connection between quantum theory and light beams that behave according to the paraxial Helmholtz equation. In 2001 Zeilinger *et al.* used photons from a SPDC source to show that the OAM is indeed discrete and quantized at the single photon level.
Using the properties of photons occupying LG modes, it is possible to draw an analogy to quantum systems described by the Schrödinger equation. Simply writing down the Schrödinger and the paraxial Helmholtz equation next to each other shows the structural similarities between a quantum system and a laser beam.

$$-\left(\frac{\hbar^2}{2m}\nabla^2 + i\hbar\frac{\partial}{\partial t}\right)\psi(x,y,t) = 0 \tag{2.29}$$

$$\left(\nabla^2 - 2ik\frac{\partial}{\partial z}\right)C(x,y,z) = 0\ , \tag{2.30}$$

with $\nabla^2 = \partial_x^2 + \partial_y^2$. Besides the constant factors, these two equations have the exact same structure.
Therefore we draw the analogy between the 2D-Schrödinger equation, which describes a 2D quantum system that evolves with time t, and the paraxial Helmholtz equation, which describes a 2D laser beam that evolves in space in the direction z.
Using this analogy for our simulation scheme we can use a LG beam (which obays the Helmholtz equation) and propagate it in space to simulate a quantum system (which obeys the Schrödinger equation) that propagates in time.
In fact, this comparison is more than an analogy to simulate a quantum system. It is qualitatively correct as photons in such laser modes do posses an angular momentum and an orbital angular momentum [61].
Let's look at a concrete example for the Laguerre-Gaussian modes which we use for our simulation. The LG mode functions are solutions to the paraxial Helmholtz equation

$$\begin{aligned} LG_{p\ell}(\rho,\phi,z) = & c_{p\ell}\frac{w_0}{w(z)}\left(\frac{\sqrt{2}\rho}{w(z)}\right)^{|\ell|} L_p^{|\ell|}\left(\frac{2\rho^2}{w^2(z)}\right)\exp\left(-\frac{\rho^2}{w^2(z)}\right) \\ & \exp\left(-i\left(\frac{k\rho^2}{2R(z)} + \left(2p+|\ell|+1\right)\Phi(z)\right)\right)\exp\left(-i\ell\phi\right), \end{aligned}$$

To determine the quantity of OAM of a photon we can start with the electromagnetic theory and the direction of the Poynting vector, which determines the direction of energy flow. If we follow that description we find that the density of the z component of orbital angular momentum is [62]

$$\ell_z = \varepsilon \frac{\ell}{\omega} \ . \tag{2.31}$$

We know each photon has the energy $\varepsilon = \hbar\omega$ and it follows the known fact that the OAM of each photon is [19]

$$\ell_z = \ell\hbar \ . \tag{2.32}$$

We can compare this to the quantum harmonic oscillator (QHO), which is a solution to the Schrödinger equation. Using the second quantization and the circular raising operators

$$\hat{a}_{\pm}^{\dagger} = \frac{1}{\sqrt{2}} \left(\hat{a}_x^{\dagger} \pm \hat{a}_y^{\dagger} \right) \ , \tag{2.33}$$

we get the number operator $N = n_+ + n_- + 1$ and we can write the QHO eigenstates in polar coordinates as

$$\psi_{p,m}(\rho, \phi) = \sqrt{\frac{p!}{\pi(p+m)!}} \rho^{|m|} \mathrm{e}^{\mathrm{i}m\phi - \rho^2/2} \mathrm{L}_{\mathrm{p}}^{|\mathrm{m}|}(\rho^2) \ , \tag{2.34}$$

where $L_p^{|m|}$ are the generalized Laguerre polynomials. The energy eigenvalues of those states are

$$\varepsilon_{m,p} = n_+ + n_- + 1 = 2p + |m| + 1 \ . \tag{2.35}$$

This is the same exponent in the expression of the Gouy phase for the LG beams. With this comparison it is possible to identify any arbitrary solution $\psi(\xi, \eta, \chi)$ of the Schrödinger equation for the QHO with an arbitrary solution $u(\mathbf{r}, z)$ of the paraxial Helmholtz equation [63]

$$u(\mathbf{r}, z) = \frac{1}{\gamma} \psi(\xi, \eta, \chi) \mathrm{e}^{\frac{\mathrm{ikR}^2}{2\mathrm{q}}} \ , \tag{2.36}$$

with $\xi = x/\gamma, \eta = y/\gamma$ and the parameters γ, q and χ are defined in relation to z through

$$\frac{1}{\gamma^2} - \frac{ik}{q} = \frac{k}{b + iz}$$
$$\tan \chi = \frac{z}{b} .$$

However in our analogy we only want to simulate the energy levels of a HO. If we limit our system to states where $p = 0$ then the energy levels become

$$\varepsilon_m = (|m| + 1)\hbar\omega . \tag{2.37}$$

Renamingg the index $m \to \ell$ so we have the same index as the LG modes the energy becomes

$$\varepsilon_\ell = (|\ell| + 1)\hbar\omega . \tag{2.38}$$

The energy of the QHO in this case only depends on the index ℓ. If we now draw the analogy between energy states of the QHO and OAM states of LG beams of light, we can identify every energy level with a projective measurement of the OAM of a LG mode [24]. This means we can simulate a quantum system with LG beams containing OAM. We can prepare this system, apply processes or transformations, and measure the initial or final energy of the system.
The experimental platform and how to implement this simulation scheme based on this analogy is presented in the next chapter.

3. Experiment

3.1 Experimental setup

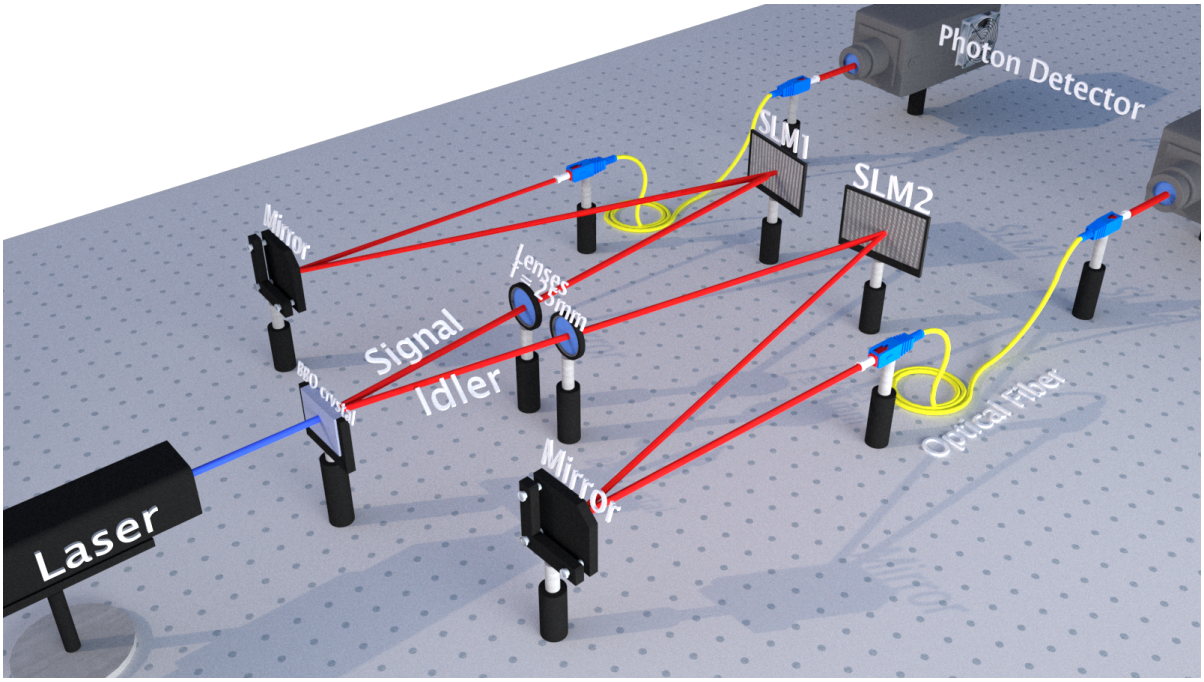

Figure 3.1: Experimental setup: A BBO-crystal is pumped with a diode laser. The generated signal and idler beams are diffracted by SLMs and coupled to single-mode optical fibers. At the output of the fiber, they are detected by single-photon counting modules and coincidences are recorded.

In this chapter we will present an experiment where we use LG beams and their OAM to simulate quantum systems through the analogy shown in the previous section. A sketch of the experimental setup is shown in figure 3.1. A 405 nm diode-laser is used to pump a non-linear Beta-Barium-Borate (BBO) birefringent crystal. The so-called pump beam coming from the laser is considered to be approximately Gaussian, monochromatic and has a linear polarization with orientation in the direction of the extraordinary axis of the BBO crystal. In the crystal, the process of spontaneous parametric down-conversion (SPDC) takes place. This process annihilates one pump photon and generates two photons, the signal and idler photons (or only signal and

idler), according to the type-I phase matching conditions (see Chapter 3.4). In the beam paths of the signal and idler beams, we placed two collimating lenses of focal length $f = 250\ mm$ after the crystal at the focal distance $250\ mm$. This leaves the signal and idler beams to propagate collimated, without diverging or converging. The signal and idler beams are then directed onto Spatial Light Modulators (SLM). This liquid crystal display can modulate the phase front of the two beams independently. Subsequently, signal and idler are coupled to single-mode optical fibers. Such fibers only couple photons in modes with zero OAM ($\ell = 0$). The photons that were coupled to the fibers are then detected by a single-photon-counting-module. In the experiment we used the single-photon avalanche diode SPCM-AQR-12 (and SPCM-AQR-14), which have a efficiency of around 50% at 830 nm and a dark count rate of 250 (50) counts/per second. The single photon timing resolution is 350 ps at full width at half maximum and the dead time is around 50 ns. These detectors send an electric pulse upon detection of a single photon. In front of the detectors are narrow-band interference filters centered at 810 nm with a 10 nm bandwidth. The electric pulses from the two photon detectors are then sent to a field-programmable gate array that was programmed in LabVIEW as a coincidence counting module. This modules counts the electric pulses caused by the signal and idler photons and counts them simultaneously while comparing the times of arrival. We consider a coincidence event when a signal and an idler photon were detected withing a $5\ ns$ window. Due to the spatial and spectral filtering we can guarantee with high probability that the recorded coincidence events were caused by pulses generated from two twin-photons created at the same instance in the non-linear crystal from one pump photon. Only photons from such coincidence events are then post-selected. Therefore with the same high probability the post-selected detected photons exhibit energy and OAM conservation properties, which entangle the two-photon state.

With this experimental setup only photons with zero OAM will couple to the single-mode fiber and will subsequently be detected by the photon detectors and only entangled twin photons generated in the process of SPDC in the non-linear BBO crystal are post-selected and considered. In the next sections, we show how we can use this setup to prepare single photon states with a specific amount of OAM, how we can change the OAM of a single photon and how we can measure the OAM of a single photon. Further we give a quick introduction into the process of SPDC and the OAM spectrum of photons generated by this process and the OAM entanglement between the signal and idler photons.

3.2 OAM generation

For the simulation of quantum systems we need states with different energy levels. In our analogy those energy levels of the quantum system are represented by the OAM carried by a single photon. We therefore need to be able to generate arbitrary amounts of OAM for a beam of light as well as at the single-photon level. The key to this is a device called Spatial Light Modulator (SLM). This device, together with the technique of holograms can change the amount of OAM of an incoming beam of light or photon by an arbitrary amount, limited only by the spatial resolution of the SLM display.

3.2.1 Spatial Light Modulator

A SLM is a device capable of spatially modulating a beam of light. For example, projectors are used to produce images by modulating the intensity of a light beam. In our experiment however, we are just interested in modulating the *phase* and therefore the *wavefront* of our laser beam or rather of the signal and idler beams. The two SLMs used are PLUTO-2 phase-only Spatial Light Modulators produced by HOLOEYE. In some experiments we directed signal and idler beams to a single shared SLM screen that was divided into two separate controllable areas. A photograph of the device that was used in all of the experiments presented here is shown in figure 3.2. The SLM has a reflective liquid crystal on silicon micro-display with a resolution of 1920x1080 pixels. The distance between the center of each pixel is 8 μm. Upon reflection, every pixel can be controlled separately to vary the phase of the incoming light beam approximately from 0 to 2π. The modulation of each pixel is controlled by applying an 8-bit grayscale from 0 to 255, giving the possibility of 256 different phase modulation strengths. The modulation strength is wavelength dependent, but with a good calibration the full range of the 256 values can be fitted to the range between 0 and 2π. To control the SLM screen and therefore the applied phase-front modulation, we connect the device to a computer and use it like an ordinary computer screen. We can then chose a grayscale image to be projected onto the screen. To generate the image that will exhibit the desired phase-front modulation, we wrote a program in LabVIEW which calculates an image and sends the image to the SLM screen. The calculations of these images or masks depends on a variety of parameters like the amount of OAM, the angle in which the modulated beam propagates, the wavelength of the incoming light, the center of the light beam, and several more.

Figure 3.2: Photograph of a PLUTO-2 spatial light modulator manufactered by HOLOEYE.

When the SLM is turned off, or a blank image is projected onto the display it acts almost like a mirror. There are minor diffraction effects due to the limited size of the pixels. Even thouh the SLM is a phase-only modulator, by chosen a suited mask we can modulate the intensity of an incoming beam through constructive and destructive interference. For our purpose we use the phase modulation to generate and modulate light beams containing orbital angular momentum by using the technique of holograms.

3.2.2 Holograms

In general, holography is a technique to first record a wavefront in order to reconstruct it later. For example, we can reconstruct the wavefront of a light beam that was reflected by an object. To reconstruct such a reflected wavefront we divide this process into two steps. In the first step, a light beam (for example a plane wave or Gaussian beam) is divided into two beams. One beam is directed at an object of interest and the second beam, the reference beam, is propagated freely. The two beams are then recombined in the same plane, causing them to interfere. This interference pattern can be recorded by a photographic film, for example, which is then called the *hologram*. All the information necessary to reconstruct the light field reflected by the object is available in the interference pattern, the recorded hologram. In the second step, we can then illuminate the hologram with the same light beam used before, the reference beam. This will generate a light beam identical to the reflected light created by the object in the first step. With this technique, we can, therefore, use specific interference masks to generate light beams with different intensity and phase

distributions with great versatility. We note, that with this technique we need only a phase modulation of the reference beam and no intensity modulation, even though the modulated beam has a different intensity distribution compared to the initial reference beam. This is the reason we chose this method to generate light beams containing OAM, as we just need a phase-only SLM, which we can control with great flexibility and change the projected holograms almost instantly.

For our purpose, the object of interest we try to reconstruct are Laguerre-Gaussian beams containing OAM. The reference beam corresponds to the signal and idler beams, incident on the SLM. As the process of SPDC preserves the structure of the incident beam, signal and idler beam maintain the same modal structure as the beam of the pump laser. The laser emits an approximately Gaussian beam and we, therefore, take our reference beam to be Gaussian. In a simplified approach this Gaussian beam can be assumed as a plane wave. As an example, we would like to generate a Laguerre-Gaussian beam with $\ell = 3$. The first step is then to record the interference pattern of the wavefront of this very Laguerre-Gaussian beam ($\ell = 3, p = 0$) and a plane wave propagating in a relative angle to each other. The resulting interference pattern of such a superposition can be seen in figure 3.3.

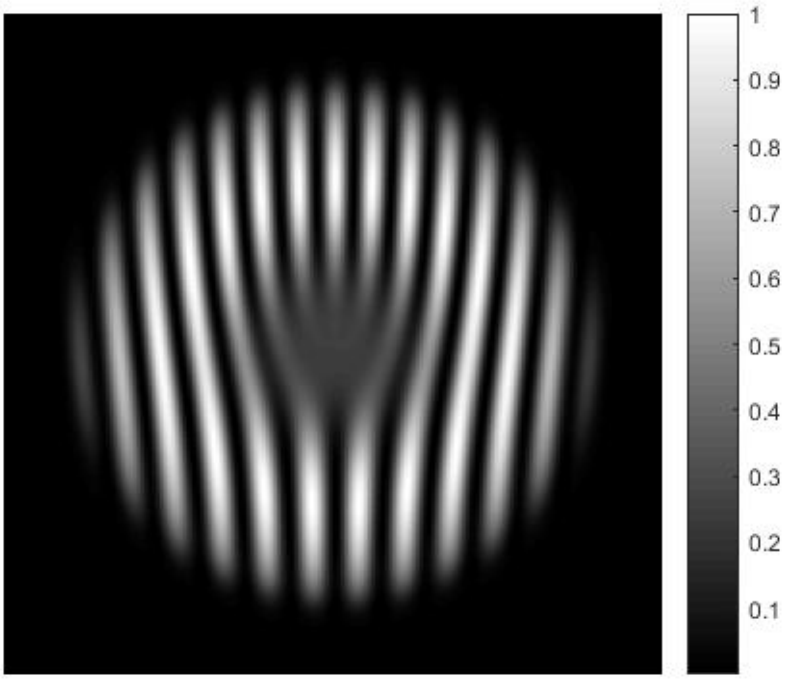

Figure 3.3: Interference pattern of a Laguerre-Gaussian beam ($\ell = 3$, $p = 0$) and a plane wave.

Now in the second step we want to reconstruct the initial beam. Therefore we direct a plane wave onto the recorded phase mask. This recorded hologram from Fig. 3.3 behaves like a diffraction grating. The zero-order maximum coincides with the reference beam and the first diffraction maximum is the desired Laguerre-Gaussian beam which possesses the desired OAM of $\ell = 3$.

To generate beams of light which possess a specific value of OAM ℓ, amplitude and phase distribution we filter the first-order maximum spatially by only considering the angle of propagation of the first-order maximum. Instead of actually recording hologram masks for every LG beam we can calculate the phase mask that will generate a beam of light with the desired properties in the first order of diffraction [64]. The hologram can be realized like a binary grating. For example, for a phase difference between 0 and π we set the transmission to zero (black) and for a phase difference between π and 2π we set the transmission to be unity (white). Like this, only a portion of the initial intensity will be coupled into the first order maximum of diffraction. To improve the energy that is coupled to the first order, we can replace the binary diffraction grating with a blazed diffraction grating [65]. This blazing improves the intensity in the first order maximum drastically.

As we are mainly interested in the amount of OAM contained in the resulting beam, we just need to reproduce the helical phase distribution of the Laguerre-Gaussian beams, as this phase generates the twisted phase front responsible for the OAM. It is therefore sufficient to only consider the phase distribution to calculate the desired hologram diffraction patterns [14]. This will generate beams with a slightly different intensity profile than LG beams but with the correct phase pattern, generating the OAM. An example of such a calculated hologram is shown in figure 3.4.

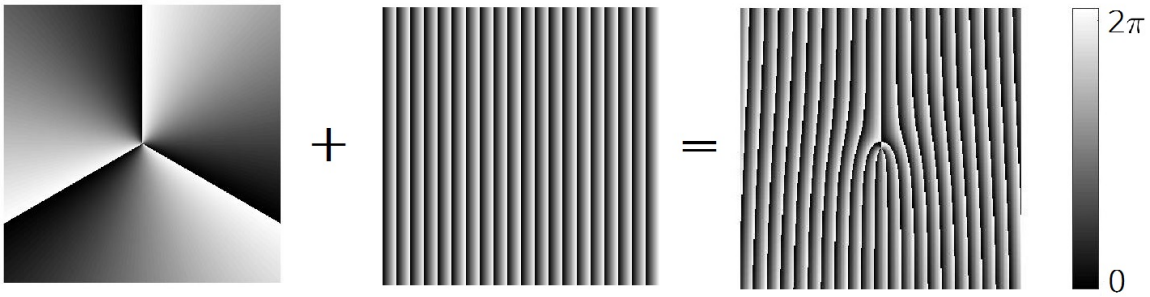

Figure 3.4: Example of the calculation of a hologram mask to change the OAM of light beams by $3i\hbar$. Shown is the superposition of the phase distribution of a LG beam ($\ell = 3$) and a blazed diffraction grating.

We take the phase distribution of the Laguerre-Gaussian beam with the

amount of OAM we want to generate and add it to a blazed interference grating. The sum is then expressed as modulo 2π. These step in calculating the masks are integrated into the LabVIEW program creating the images that will be projected onto the SLM screen. After the parameters have been passed, the program calculates the hologram masks and transforms it into an 8-bit grayscale image. This image is then projected onto the SLM screens where the modulation of the signal and idler beams takes place. An illustration of this OAM generation process is shown in fig. 3.5. A Gaussian beam $[LG(\ell = 0, p = 0)]$ is directed at a forked hologram mask with a forked blazed grating. The diffracted beam in first-order has then an OAM of $\ell = +1$.

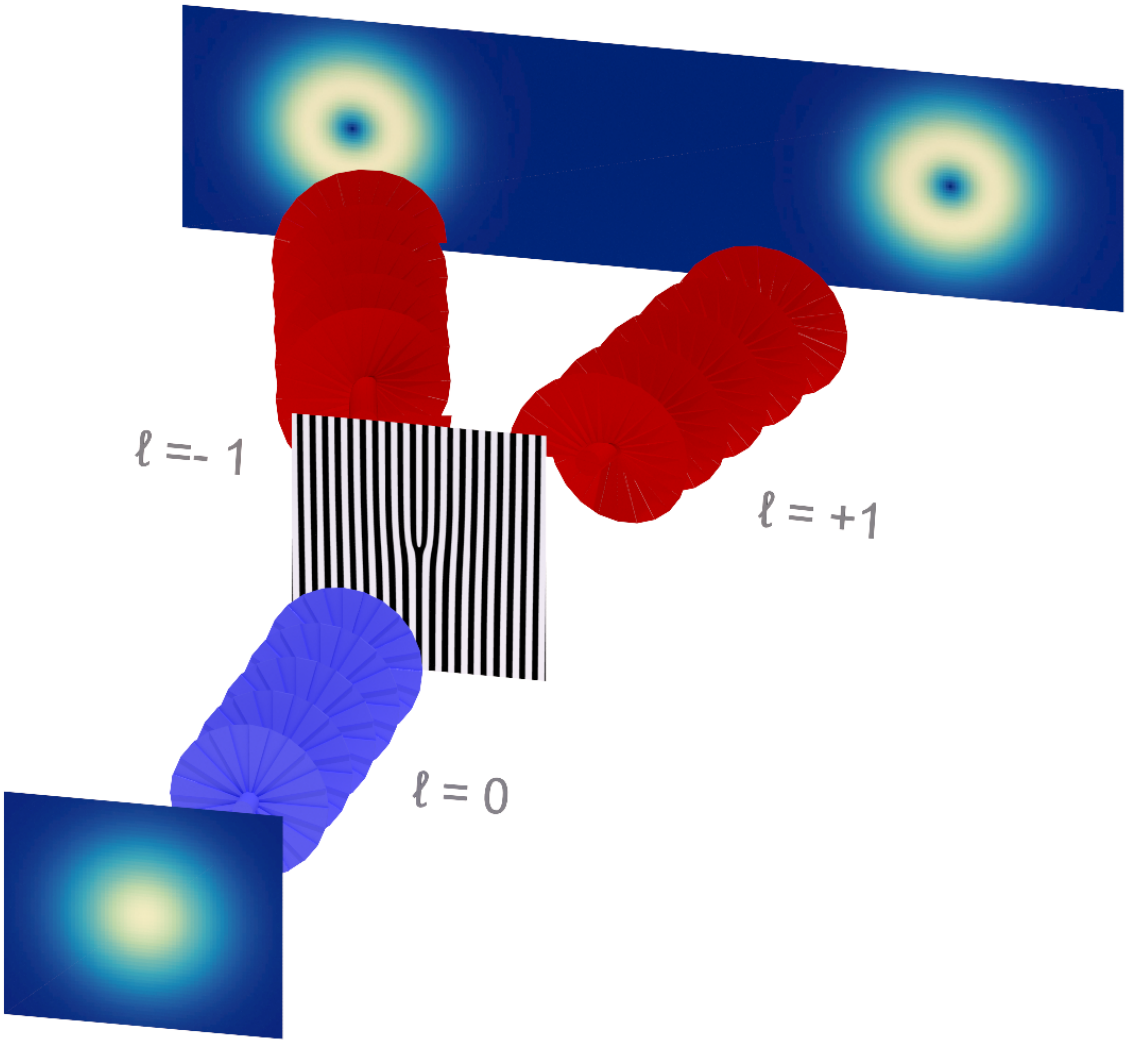

Figure 3.5: Production of a beam of light containing an OAM of $\ell = +1$. A plane wave (Gaussian beam) hits a forked hologram mask. The first-order diffracted beams obtain the desired helical phase fronts to generate OAM.

The same masks used to generate a beam containing OAM from an initial plane wave (Gaussian beam) can be utilized to lower or raise the OAM of an incident beam. For example, a hologram mask that would transform an incoming plane wave with zero OAM into a beam containing OAM of $\ell\hbar$, would change the OAM of any incoming beam with OAM $5\hbar$ to $(5+\ell)\hbar$. This fact is used to prepare, change and measure the OAM of a beam of light or single photons.

3.3 OAM detection

3.3.1 Mode Sorter

There are several different techniques and approaches to measure the OAM of a light beam or a photon. For example in an earlier work [24] we have used a device called *mode sorter* [66]. This device unfolds the circular phase profile of a Laguerre-Gaussian beam into a linear phase distribution with an optical element that performs a spiral transformation. This linear phase ramp can then be used with a convex lens to direct different orders of Laguerre-Gaussian beams onto different spatial positions in the detection plane. The detection plane is then recorded with a CCD camera and each position is calibrated and identified with a certain amount of OAM. In the experiment mentioned, we used a HeNe-Laser at a visible wavelength of $633\ nm$. In the experiments presented here, we want to measure the OAM of the signal and idler beams at a infrared wavelength of $810\ nm$, though. Because the mode sorter needs a very sensitive alignment and calibration, we could not use this device with invisible light and single photon intensities. For the numerical simulations of the experiments presented here, on the other hand, we used this technique of spiral transformations to analyze the OAM spectrum of our beams of light. The mode sorter we have used in the previous experiment has the disadvantage that adjacent LG modes overlap in the detection plane. Therefore we need to calibrate every mode with a localized intensity distribution, instead of only a single position. The mode sorter we programmed for numerical simulation is the slightly improved spiral transformations described in ref. [67], which completely separate adjacent modes spatially.

3.3.2 Single-mode Fiber Detection

The OAM measurement scheme that was used in the experimental setup shown in Fig. 3.1 consists of an SLM, a single-mode fiber and a photon detector. The optical single-mode fiber couples only modes with zero OAM ($\ell = 0$). We can use the

SLM to change the OAM of an incident light beam with arbitrary OAM by an arbitrary amount ℓ, as described in the previous section. Let's define a hologram mask $\mathcal{L}_m$ that is projected onto the SLM will perform the change in OAM from $\ell \to \ell + m$. Then photons incident on the SLM screen with an OAM of $\ell = k$ will be transformed into modes with an OAM of $\ell = k + m$. If we now apply the mask $\mathcal{L}_{-k}$, then photons with an initial OAM of $\ell = k$ will end up with $\ell = 0$. Every photon with a different initial OAM will have $\ell \neq 0$. Therefore the only photons that will couple to the single-mode fiber are photons that had initially an OAM of $\ell = k$ before they hit the SLM. The output of the fibers are subsequently detected by the single photon avalanche detectors. This means the choice of the OAM-lowering or -raising operation performed by the hologram mask projected on the SLM determines the amount of OAM of the detected photons before they entered the detection apparatus.
In order to measure the OAM spectrum of the signal or idler beam we can scan the SLM with different hologram masks $\mathcal{L}_m$, for example $m = [-10, 10], m \in \mathbb{Z}$. Counting the coincidence events for the photons that coupled to the fiber for each value of m, we can measure the OAM distribution of the incident light beam from $\ell = -10$ to $\ell = +10$. An example of a measured OAM distribution is shown in Fig. 4.3.
With the described measurement scheme we can measure single OAM values of incoming photons or beams of light by choosing a single mask $\mathcal{L}_m$ projected onto the SLM screen. It is also possible to generate a superposition of several masks (with $\mod 2\pi$) and project it onto the SLM. Instead of applying the two masks $\mathcal{L}_{-3}$ and $\mathcal{L}_{-4}$ separately to detect incoming photons with OAM of either $\ell = 3$ or $\ell = 4$, we could apply the superposition of the two masks $\mathcal{L}_{-3} + \mathcal{L}_{-4}$. This would couple both, photons with $\ell = 3$ and photons with $\ell = 4$, as well as photons in OAM superposition states of $\ell = 3$ and $\ell = 4$. This lowers the detection efficiency as photons with $\ell = 3$ have a chance to be modulated to have $\ell = -1$.

3.4 Spontaneous Parametric Down-Conversion

3.4.1 Theory and Entanglement

In the experiments presented here we want to simulate quantum systems by employing the OAM basis of single photons. So far, we have shown how to create or change the OAM of a beam of light or a photon and how to measure it. To generate single photon states we use the non-linear process of spontaneous parametric down-conversion. The process of SPDC is the most widespread used technique for creating

entangled photon pairs nowadays. Experiments that employ entangled photons [68] or need a heralded single-photon source [69] commonly achieve this through the process of SPDC in a non-linear crystal. SPDC is a second-degree non-linear optical process in which a photon incident on a non-linear crystal spontaneously separates into two photons of lower frequencies [70]. Those two down-converted photons often referred to as *twin photons* exhibit correlations in a variety of degrees of freedom. Since the 1970s the correlations between the fields generated by SPDC are observed [7]. Correlations have been observed for the spectral [71] and temporal [72] degrees of freedom, and the spatial degrees of freedom. The latter include the transverse spatial profile [73, 74], transverse position and the momentum [75, 76]. The orbital angular momentum as one of those degrees of freedom is entangled as well, and their investigation is fairly recent [77]. As we want to prepare states in the basis of OAM states, we will use the process of SPDC as our photon source.

Down-converted photons are ”born” at the same instance of time in the non-linear crystal, which causes time correlation between the two down-converted photons. This time entanglement is essential in order to filter out the *twin photons* by post-selecting them after detection.

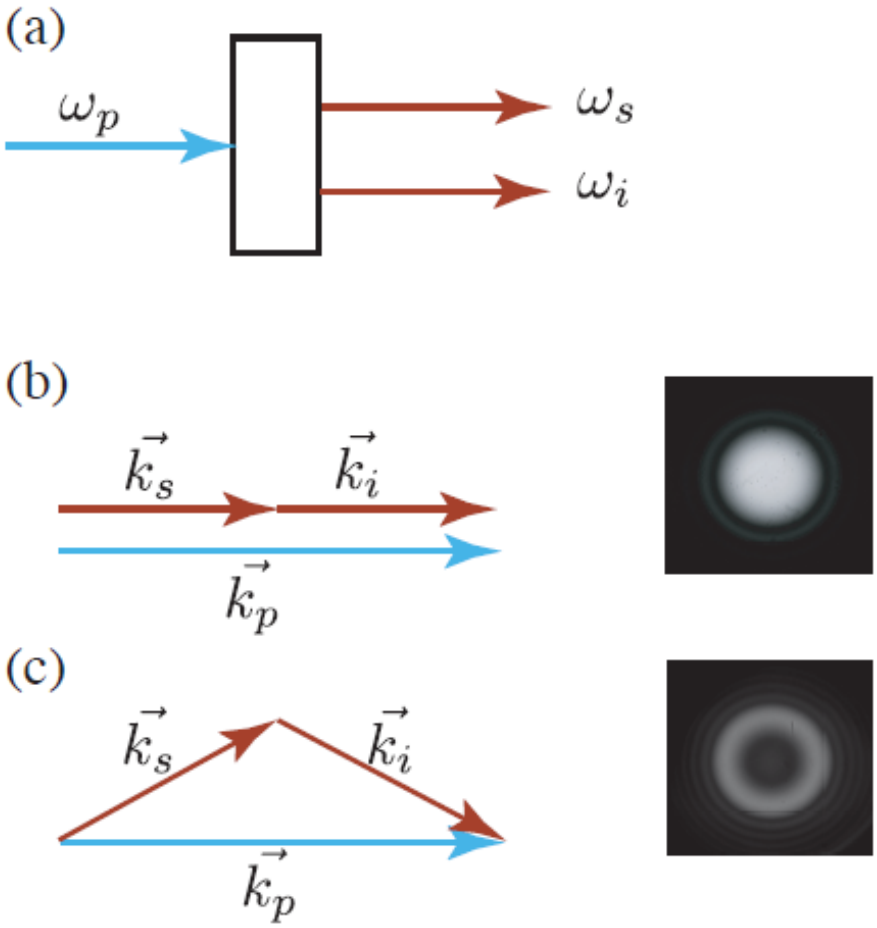

Figure 3.6: (a) In the process of SPDC, a pump photon with frequency ω_p decays spontaneously into two photons of the lower frequencies ω_s and ω_i. (b) In the collinear setup, the two down-converted twin photons are emitted into the same direction parallel to the pump beam direction, resulting in a bright spot. (b) In the noncollinear setup, the twin photons are emitted with opposite transverse momentum, resulting in a bright ring, propagating in the shape of a cone.

When the pump photon decays into the two twin photons, called *signal* and *idler* (figure 3.6 (a)), they follow laws of energy conservation. As this is a parametric process, their angular frequencies follow the equation

$$\omega_p = \omega_s + \omega_i \ . \tag{3.1}$$

The emission is the greatest when pump ($\vec{k_p}$), signal ($\vec{k_s}$) and idler ($\vec{k_i}$) photons follow as well the conservation of linear momentum.

$$\vec{k_p} = \vec{k_s} + \vec{k_i} \ . \tag{3.2}$$

Those two conservation laws are referred to as the phase-matching conditions. The process of SPDC is the most efficient when those conditions are fulfilled. The condition in Eq. (3.2) can be met in two different ways. The SPDC can be collinear, meaning that signal and idler photons are created with their $\boldsymbol{k}$-vector in the same direction, parallel to the pump beam (figure 3.6 (b)). A second possibility is the SPDC being non-collinear, emitting signal and idler photons in different directions with opposite transverse momentum while still fulfilling the phase-matching conditions (figure 3.6(c)). In our experiment, we employ the type-I non-collinear SPDC, meaning that signal and idler beam have the same linear polarization, orthogonal to the pump polarization.

The process of SPDC is related to the tensor of second-order for the dielectric susceptibility which appears in the expansion of the electric polarization:

$$\boldsymbol{P}(\boldsymbol{E}) = \varepsilon_0 \left(\chi^{(1)} \boldsymbol{E} + \chi^{(2)} \boldsymbol{E}^2 + \chi^{(3)} \boldsymbol{E}^3 + ... \right) \ . \tag{3.3}$$

Focusing on the non-linear interaction, we apply a perturbation to the electromagnetic field Hamiltonian in a dielectric medium [10], yielding

$$\mathcal{H}(t) = \mathcal{H}_0(t) + \mathcal{H}_I(t) \ . \tag{3.4}$$

The perturbation $\mathcal{H}_I(t)$ is then the nonlinear interaction Hamiltonian. After quantizing the electrical field we can calculate the state $|\psi(t)\rangle$ of the system for any time t by applying the time evolution operator

$$\mathbf{U}(t) = \exp\left(\frac{1}{i\hbar} \int_0^t d\tau \mathbf{H}_I(\tau) \right) \ . \tag{3.5}$$

to the photon state at time $t = 0$ when the interaction in the crystal takes place:

$$|\psi(t)\rangle = \mathbf{U}(t)|\psi(0)\rangle \ . \tag{3.6}$$

This leads to a rather big and unpractical expression. In order to simplify the equation, we make some approximations such as the pump beam has a moderate frequency spread and contains only extraordinary polarization; the crystal is large in x and y directions compared to the pump size; we put the detectors with a small aperture far away from the crystal so that each detector only selects one spatial mode; narrow bandwidth filters are placed in front of the detectors limiting the possible frequency combinations between pump, signal and idler beams. This monochromatic approximation eliminates the time dependence of the state. The last

two approximations are specific to the experimental apparatus. This leads to the much simpler expression for equation (3.6) [10, 75]

$$|\psi\rangle_{SPDC} = C_1|vac\rangle + C_2|\psi\rangle \ . \tag{3.7}$$

The first state $|vac\rangle$ is the vacuum state. We are only interested in the second two-photon state $|\psi\rangle$. We can then write the two-photon state at the output right after the non-linear crystal as [78]

$$|\psi\rangle = \int\int d\boldsymbol{k}_s \ d\boldsymbol{k}_i \ \Phi(\boldsymbol{k}_s, \boldsymbol{k}_i)\hat{a}_s^\dagger(\boldsymbol{k}_s)\hat{a}_i^\dagger(\boldsymbol{k}_i)|vac\rangle \ . \tag{3.8}$$

$\hat{a}_s^\dagger(\boldsymbol{k}_s)$ and $\hat{a}_i^\dagger(\boldsymbol{k}_i)$ are the single photon creation operators for the signal and idler modes with their respective wave vectors $\boldsymbol{k}_s, \boldsymbol{k}_i$. $\Phi(\boldsymbol{k}_s, \boldsymbol{k}_i)$ is the mode function of the pump and includes the phase matching conditions. We can express this function as

$$\Phi(\boldsymbol{k}_s, \boldsymbol{k}_i) = \int d^3k_p \ \tilde{E}_p(\boldsymbol{k}_p) \ \varepsilon(\boldsymbol{k}_p - \boldsymbol{k}_s - \boldsymbol{k}_i) \ \delta(\omega_p - \omega_s - \omega_i) \ , \tag{3.9}$$

where the ε is due to the phase matching conditions and the δ term enforces the energy conservation $\omega_p = \omega_s + \omega_i$, and $\tilde{E}$ is the beam profile of the pump. We can write the phase matching function, for a crystal of finite thickness L, and length much larger than the pump beam size, and if the angle between signal and idler beams is small enough that the z component of the momentum vector $(\sqrt{k^2 - q^2})$ can be approximated by $k - q^2/2k$ as

$$\Phi(\boldsymbol{k}_s, \boldsymbol{k}_i) = \tilde{E}(q_s + q_i)\frac{1}{\pi}\sqrt{\frac{2L}{k_p}}\mathrm{sinc}\left(\frac{\mathrm{L}|\mathrm{q_s} - \mathrm{q_i}|^2}{4\mathrm{k_p}}\right)\mathrm{e}^{-\mathrm{i}\frac{\mathrm{L}|\mathrm{q_s}-\mathrm{q_i}|^2}{4\mathrm{k_p}}} \ . \tag{3.10}$$

L is the length of the crystal in the z direction and k_p is the magnitude of the pump's wave vector $\boldsymbol{k}_p$. A full derivation of these results can be found in ref. [12]. We see that signal and idler photons are entangled in various degrees of freedom, determined by the various factors shown in the equations above. The main entangled degrees of freedom are time, energy and momentum. The time entanglement will be used for post-selecting twin-photons in coincidence measurements and the entanglement of energy lets us filter the down-converted photons for specific frequencies. The linear momentum conservation of the photons lets us filter the direction of propagation, but the more interesting momentum entanglement for our purpose is the entanglement of the orbital angular momentum. We will explicitly show how to exploit the OAM

entanglement for the remote state preparation of thermal states.

3.4.2 Coincidence Amplitudes

In our experiment we measure the coincidences between photon detection events of signal and idler photons. Two twin photons (signal and idler photons) that are generated from one pump photon in the process of SPDC are entangled in time. Post-selecting a signal and an idler photon through coincidence counting guarantees that these two photons indeed were generated in the same SPDC process and preserve energy and momentum compared to the pump photon that gave rise to the twin photons. As we are later on interested in the OAM spectrum of the signal and idler photons we want to measure those photons in LG modes. A photon in a pure LG mode can be expressed as

$$|\ell, p\rangle = \int dr\ LG_p^\ell\ (r,\phi)\hat{a}^\dagger(r)|vac\rangle\ , \tag{3.11}$$

where $LG_p^\ell(r,\phi)$ are the Laguerre-Gaussian transverse profiles of the corresponding LG modes

$$LG_p^\ell(r,\phi) = \sqrt{\frac{2p!}{\pi(p+|\ell|)!}}\ \frac{1}{\omega}\left(\frac{\sqrt{2}r}{\omega}\right)^{|\ell|} \mathrm{e}^{-\frac{\mathrm{r}^2}{\omega^2}} \mathrm{L}_\mathrm{p}^{|\ell|}\left(\frac{2\mathrm{r}^2}{\omega^2}\right) \mathrm{e}^{\mathrm{i}\ell\phi}\ . \tag{3.12}$$

We can then make use of $\mathcal{I} = \sum_{\ell,p} |\ell,p\rangle\langle\ell,p|$ to write the two photon state from Eq. (3.8) as the following:

$$|\Psi\rangle = \sum_{\ell_1,p_1}\sum_{\ell_2,p_2} C_{p_1,p_2}^{\ell_1,\ell_2}|\ell_1,p_1\rangle|\ell_2,p_2\rangle\ . \tag{3.13}$$

The coincidence probability of finding a signal photon in the LG mode characterized by the indices ℓ_s and p_s and an idler photon in the LG mode characterized by the indices ℓ_i and p_s is then

$$P_{p_s,p_i}^{\ell_s,\ell_i} = \left|C_{p_s,p_i}^{\ell_s,\ell_i}\right|^2\ . \tag{3.14}$$

The coincidence amplitudes $C_{p_s,p_i}^{\ell_s,\ell_i}$ can be determined by the overlap integral

$$\begin{aligned} C_{p_s,p_i}^{\ell_s,\ell_i} &= \langle\psi_i,\psi_s|\psi_{SPDC}\rangle \\ &= \int\int d^3k_s d^3k_i\ \Phi(\boldsymbol{k}_s,\boldsymbol{k}_i)\left(LG_{p_s}^{\ell_s}\right)^*\left(LG_{p_i}^{\ell_i}\right)^*\ . \end{aligned} \tag{3.15}$$

The phase matching function $\Phi(k_s, k_i)$ can be simplified by applying the thin-crystal approximation, where the crystal length is short compared to the Rayleigh length. Equivalently one can assume a colinear setup ($\boldsymbol{q}_s = \boldsymbol{q}_i = 0$). The sinc term in Eq. (3.10) then reduces to unity [78]. If we write the pump photon in the basis of LG modes as well, like the signal and idler photons, the coincidence amplitudes can be calculated from

$$C^{\ell_s,\ell_i}_{p_s,p_i} \propto \int_0^{2\pi} d\phi \int_0^{\infty} r\ dr\ LG^{\ell_p}_{p_p} \left(LG^{\ell_s}_{p_s}\right)^* \left(LG^{\ell_i}_{p_i}\right)^* . \tag{3.16}$$

By simply evaluating the azimuthal part of the integral in (3.16).

$$\int_0^{2\pi} d\phi\ \mathrm{e}^{i(\ell_p-\ell_s-\ell_i)\phi} = 2\pi\delta_{\ell_p,\ell_s+\ell_i} , \tag{3.17}$$

we see easily the OAM conservation in the down-conversion process, due to the phase matching conditions [16, 79]:

$$\ell_p = \ell_s + \ell_i . \tag{3.18}$$

Fig. 3.6 shows how the energy and linear momentum is preserved in the SPDC process. Fig. 3.7 is an illustration of how the OAM is as well conserved in the SPDC process. In the example, a non-linear crystal is pumped with a beam of light containing OAM of $\ell_p = +2$. The two down-converted beams signal and idler can then have OAM of $\ell_s + \ell_i = \ell_p = +2$. This obeys the momentum conservation expressed in Eq. (3.18). Other combinations like $\ell_s = 2$ and $\ell_i = 0$ are possible, but less likely. These probabilities are determined by the overlap interal in Eq. (3.16).

In our experiments we mainly consider the special case where the pump beam is in a Gaussian mode and has zero OAM ($\ell_p = 0$). The OAM of signal and idler are then related through $\ell_s = -\ell_i$ and the two indices can be substituted by $\ell = \ell_s = -\ell_i$. Also we are only interested in the OAM and limit ourselves the subspace where $p_p = p_s = p_i = 0$. The expression for the down-converted two-photon state simplifies to

$$|\psi\rangle = \sum_{\ell=-\infty}^{\infty} C_{|\ell|}|+\ell,-\ell\rangle_{si} , \tag{3.19}$$

with the coincidence amplitudes $C_{|\ell|} = C^{\ell_s=+\ell,\ell_i=-\ell}$. This means if we find a signal photon in the OAM state $|\ell\rangle$, the idler twin-photon is in the state $|-\ell\rangle$ and has the same ℓ with opposite sign. The probability of finding a signal photon with $\ell_s = \ell$ and an idler

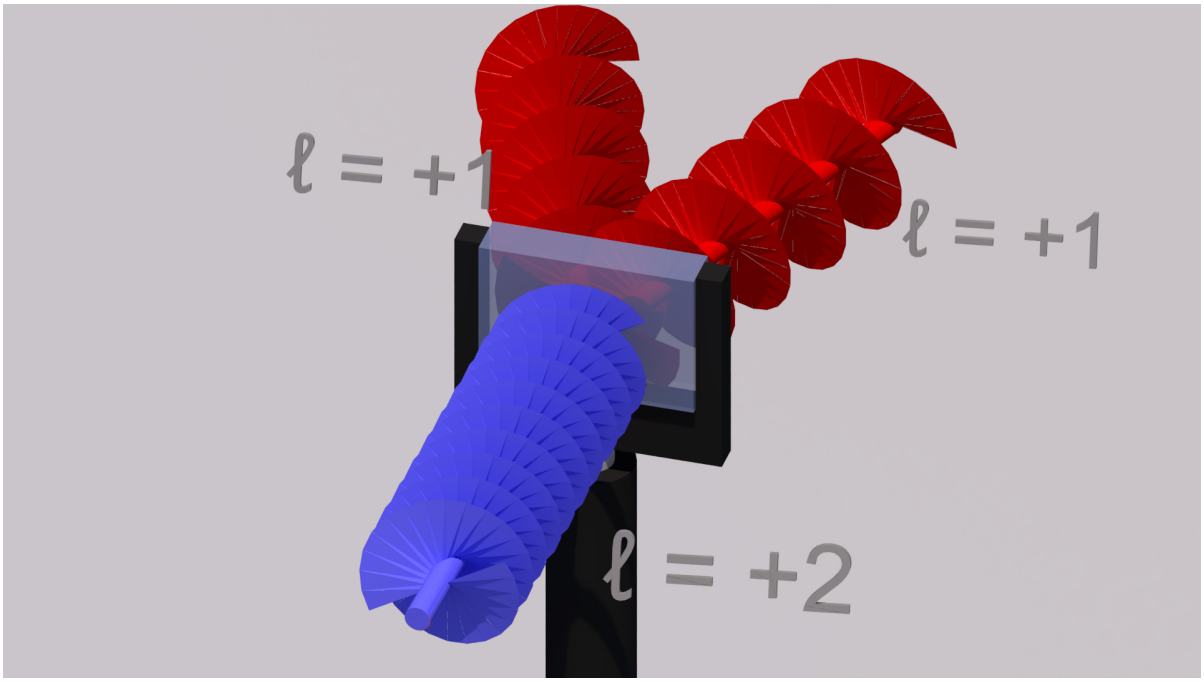

Figure 3.7: A beam of light with OAM $\ell_p = +2$ pumps a non-linear crystal. The OAM is conserved in the SPDC process. A possible combination for the OAM of the downconverted signal and idler beams is $\ell_s = +1$ and $\ell_i = +1$.

photon with $\ell_i = -\ell$ is [80]

$$P^{\ell,-\ell} = |C_{|\ell}|^2 \,. \tag{3.20}$$

3.4.3 OAM Spectrum of the SPDC process

In the process of SPDC, signal and idler photons are generated in all possible LG modes and therefore with all possible values of OAM. The only restriction on the possible OAM amounts of the two signal and idler twin photons is the momentum conservation $\ell_p = \ell_s + \ell_i$. The probability to find a signal or idler photon in the mode with OAM $\ell\hbar$ is determined by the coefficient $C_{|\ell|}$. This coefficient can be calculated through the mode overlap integral inside the non-linear crystal where the mode mixing happens.

This overlap integral then determines the OAM spectrum of the down-converted signal and idler photons. In the next chapter we want to show how to manipulate these coefficients $C_{|\ell|}$ and therefore the OAM spectrum to prepare thermal state.

We will now explicitly calculate the three-mode spatial overlap of Laguerre-Gaussian modes in the crystal during the process of SPDC, giving rise to the mentioned coefficients [81].

OAM mixing in SPDC

We calculate the overlap integral $\mathcal{O}^{\ell_p,\ell_s,\ell_i}_{p_p,p_s,p_i}$ for a pump beam with the indices ℓ_p, p_p, signal beam with ℓ_s, p_s and idler beam with ℓ_i, p_i. The overlap integral already defined in Eq. (3.16) reads

$$\mathcal{O}^{\ell_p,\ell_s,\ell_i}_{p_p,p_s,p_i} = \int LG^{\ell_p}_{p_p}(LG^{\ell_s}_{p_s})^*(LG^{\ell_i}_{p_i})^* dr^2 \ , \tag{3.21}$$

where LG^{ℓ}_{p} are the Laguerre-Gaussian mode functions defined in Eq. (2.21). We then have

$$\begin{aligned}\mathcal{O}^{\ell_p,\ell_s,\ell_i}_{p_p,p_s,p_i} =& \frac{c_{p_p,\ell_p} c_{p_s,\ell_s} c_{p_i,\ell_i}}{\omega_p\omega_s\omega_i} \int_0^\infty r\ dr \frac{(\sqrt{2}r)^{|\ell_p|+|\ell_s|+|\ell_i|}}{\omega_p^{|\ell_p|}\omega_s^{|\ell_s|}\omega_i^{|\ell_i|}} \\ &\times L^{|\ell_p|}_{p_p}\left(\frac{2r^2}{\omega_p^2}\right) L^{|\ell_s|}_{p_s}\left(\frac{2r^2}{\omega_s^2}\right) L^{|\ell_i|}_{p_i}\left(\frac{2r^2}{\omega_i^2}\right) \\ &\times \mathrm{e}^{-\left(\frac{\mathrm{r}^2}{\omega_\mathrm{p}^2}+\frac{\mathrm{r}^2}{\omega_\mathrm{s}^2}+\frac{\mathrm{r}^2}{\omega_\mathrm{i}^2}\right)} \int_0^{2\pi} \mathrm{d}\phi\ \mathrm{e}^{\mathrm{i}(\ell_\mathrm{p}-\ell_\mathrm{s}-\ell_\mathrm{i})\phi} \ .\end{aligned} \tag{3.22}$$

The azimuthal integral gives us the known orbital angular momentum conservation $\int_0^{2\pi} d\phi\ \mathrm{e}^{\mathrm{i}(\ell_\mathrm{p}-\ell_\mathrm{s}-\ell_\mathrm{i})\phi} = 2\pi\ \delta_{\ell_\mathrm{p},\ell_\mathrm{s}+\ell_\mathrm{i}}$. As we are only interested in the OAM of the signal and idler photons, which is determined by the indices ℓ, we can limit ourselves to the case where $p_p = p_s = p_i = 0$, as well as the case of the pump being a Gaussian beam with zero OAM ($\ell_p = 0$). This guarantees the signal and idler beams to have the same OAM with opposing signs ($\ell_s = -\ell_i$), so we can substitute for the variable $\ell = \ell_s = -\ell_i$. We can now normalize the overlap integral by the fundamental overlap

$$\Omega^{\ell_p,\ell_s,\ell_i}_{p_p,p_s,p_i} = \frac{\mathcal{O}^{\ell_p,\ell_s,\ell_i}_{p_p,p_s,p_i}}{\mathcal{O}^{0,0,0}_{0,0,0}} \ , \tag{3.23}$$

where

$$\mathcal{O}^{0,0,0}_{0,0,0} = \sqrt{\frac{8}{\pi}} \frac{\left(\frac{1}{\omega_p^2}+\frac{1}{\omega_s^2}+\frac{1}{\omega_i^2}\right)^{-1}}{\omega_p\omega_s\omega_i} \ . \tag{3.24}$$

Explicitly calculating the transverse integral yields the result

$$\Omega(\ell) = \Omega^{0,\ell,-\ell}_{0,0,0} = \sqrt{2}^{2|\ell|} \frac{\left(\frac{1}{\omega_p^2}+\frac{1}{\omega_s^2}+\frac{1}{\omega_i^2}\right)^{-|\ell|}}{\omega_p\ \omega_s^{|\ell|}\omega_i^{|\ell|}} \ . \tag{3.25}$$

A detailed derivation is shown in Appendix A.
As an example, we can look at the OAM distribution for the relation of the beam widths $\frac{1}{\omega_p^2} = \frac{1}{\omega_s^2} + \frac{1}{\omega_i^2} = \frac{2}{\omega^2}$, which is suggested by the phase matching and wave-front matching conditions. For this relation we get the OAM spectrum of the SPDC process as

$$\Omega(\ell) = \left(\frac{1}{2}\right)^{|\ell|} \frac{1}{\omega_p} \,. \tag{3.26}$$

From this example we can easily see that the overlap decreases exponentially for increasing values of ℓ.
This overlap determines the spectrum of the signal and idler modes, which in our case for the family of Laguerre-Gaussian modes determines the OAM of the two down-converted beams. This result yields the probability of generating two down-converted photons with OAM of ℓ_s and $-\ell_i$ from a Gaussian pump laser with $\ell_p = 0$, which becomes smaller with increasing values of $|\ell_s| = |\ell_i|$. From Eq. (3.25) we see that the slope of the exponential decay, under the approximations and assumptions we have made, only depends on the widths of the mode widths. Therefore we can manipulate this spectrum by changing the mode beam widths of the pump, signal and idler beams. In the next chapter we will show how we can use the exponential decay of the OAM spectrum of the signal and idler photons to simulate a thermal state, which also has a distribution with an exponential decay. To show how to remotely prepare single photon thermal states we performed a series of experiments where we manipulate the family of LG modes in different ways to prepare different thermal distributions.
We limit ourselves to a pump beam with no OAM ($\ell_p = 0$) because it results in exactly the overlap integral from Eq. (3.25) which gives the signal and idler photons their exponential OAM distribution. If we pump the crystal with a beam containing OAM this distribution will be different and not exponential in relation to $|\ell|$. Also the distribution will differ if we include non-zero values for the radial indices p.

4. State Preparation and Manipulation

4.1 Remote State Preparation

In our simulation scheme we want to simulate the energy levels of a quantum system through the OAM of single photons. We achieve this by using the analogy between the Schrödinger equation and the Paraxial Helmholtz equation. When we prepare OAM states of photons we can simulate the analog energy states of the system of interest.

In a previous experiment [24] we prepared a beam of light from a cw HeNe-laser in different LG modes and therefore with different amounts of OAM per photon. When we measure the OAM spectrum of those beams we can determine the state of our simulated system that is associated with this very distribution. After we prepared an OAM distribution and confirmed it through a measurement, we can let certain processes act on the system. After such a process was applied to the system we then measure the final OAM distribution and determine the transmissions between the initially prepared system and the final measured state.

In the experiments presented in this work on the other hand, we use the process of SPDC as a single-photon source instead of a laser beam to generate OAM states and simulate the system of interest. This allows us to take this simulation scheme to the quantum single-photon level. With our experimental setup, we are able to generate entangled twin photons and measure their OAM as explained in the previous chapter. The entanglement of the OAM degree of freedom between signal and idler photons allows us to remotely prepare a state in the OAM basis of one of those photons.

Again, we are only interested in the OAM degree of freedom which is determined by the index ℓ and limit ourselves to modes with $p_p = p_s = p_i = 0$, as well as the pump laser to be in a Gaussian mode (LG mode with $\ell = 0$) so that we can make use of the OAM conservation $\ell_p = \ell_s + \ell_i$, leading to $\ell_s = -\ell_i$. We recall the two-photon state in

Eq. 3.19 directly after the crystal where the process of SPDC took place

$$\begin{aligned}|\psi\rangle &= \sum_{\ell=-\infty}^{\infty} C_{|\ell|}|+\ell,-\ell\rangle_{si} \\ &= \sum_{\ell=-\infty}^{\infty} C_{|\ell|}|+\ell\rangle_s \otimes |-\ell\rangle_i \ ,\end{aligned}$$

The signal photon has the OAM ℓ and the idler photon has the OAM $-\ell$, with probability $|C_{|\ell|}|^2$. This means if we know the OAM of either signal or idler photon, the OAM of the twin photon is automatically determined through their entanglement in this degree of freedom. We can make use of this fact to prepare the OAM of an idler photon remotely by only looking at the correlated signal photon. With our OAM measurement apparatus explained in Sec. 3.3 we can select the amount of OAM that photons possess that will couple to the single-mode fiber. This results in a selection of the OAM of all the photons that can be detected by the single-photon detector. Measuring the OAM of a single signal photon is equivalent to preparing the OAM of the detected photon.
In the experiment we can measure the OAM of the signal photons, but allow correlated idler photons with all possible values of OAM. We can do this by removing the OAM measurement apparatus from the idler beam path, consisting of the single-mode fiber and the SLM. We can remove the fiber and the SLM or remove only the fiber and use the SLM display as a mirror. We then post select all coincidence events of all simultaneously detected signal and idler photons. Because in our experimental scheme the measurement of a photon with OAM ℓ is equivalent to preparing the photon with an OAM of ℓ we can simply apply the single photon bra state $\langle\ell|$ to the two-photon state. Then upon detection of a signal photon with OAM equal to $\ell_s = \ell$, the two-photon state becomes

$$\begin{aligned}\langle\ell|_s|\psi\rangle &= \langle\ell|_s \sum_{\ell=-\infty}^{\infty} C_{|\ell|}|+\ell,-\ell\rangle_{si} \\ &= \langle\ell|_s|\ell\rangle_s \, C_{|\ell|}|-\ell\rangle_i \\ &= C_{|\ell|}|-\ell\rangle_i \ .\end{aligned} \tag{4.1}$$

We end up with a single-photon state for the idler photon with an OAM equal to $\ell_i = -\ell$, determined by the measured OAM of the signal photon. The sum disappeared because the coincidence amplitude equals zero for all $\ell_i \neq -\ell_s$ due to the conservation of OAM. This shows that by measuring and therefore preparing the OAM of the signal photon we determined the OAM of the idler photon. We *remotely* prepared the single-photon

OAM state by only acting on the signal photon.

4.2 Thermal States

With the idea of performing thermodynamic processes in mind, states of special interest to us are *thermal states*. Thermal states are states emitted by thermal sources. Such thermal sources are quite common in nature, like the sun or black bodies, but they are difficult to prepare in the laboratory, even more difficult in the quantum limit, in a way that is useful and manipulable. In Quantum Optics, a thermal state is produced by any body in thermal equilibrium at a temperature T. Such heated bodies emit electromagnetic radiation, called thermal radiation or chaotic radiation. A light bulb would be such a thermal source. Apart from the emissivity, thermal radiation from a real source is equal to the black body radiation. A black body radiates a continuous spectrum of frequencies over a wide range. The spectrum and the radiated energy depend on the temperature of the surface of the body and their relation can be described by Planck's law of black body radiation [82, 83]

$$B_\nu(T) = \frac{2h\nu}{c^3} \frac{1}{\mathrm{e}^{\frac{\mathrm{h}\nu}{\mathrm{k_B T}}} - 1} \ , \tag{4.2}$$

where $B_\nu(T)$ is the spectral radiance, h is the Planck constant, c is the speed of light, k_B is the Boltzmann constant, ν is the frequency of radiation and T is the absolute temperature of the body. The overall power of radiation is found to increase with the fourth power of the absolute temperature and is expressed by the *Stefan-Boltzmann law*. The radiation emitted by a black body is spread into several electromagnetic modes. These modes can be described in terms of plane waves and they are characterized by a wave vector $\vec{k}$ and a frequency ν. These modes are called *thermal states* and in the optical regime, we call them *optical modes*. The energy of the photons occupying these modes is determined by their frequency. Therefore, the radiated energy of a single mode, of a single frequency is quantized, as only a finite amount of photons occupy each mode. The average number of photons occupying each single optical mode coming from a thermal source was found to be [83]:

$$\langle n_\nu \rangle = \frac{1}{\mathrm{e}^{\frac{\mathrm{h}\nu}{\mathrm{k_B T}}} - 1} \ . \tag{4.3}$$

This relation is known as the Bose-Einstein distribution law for photons. All the properties of thermal radiation depend on the absolute temperature of the radiating

body and are heavily subjected to fluctuations. Therefore a thermal state is defined just by its statistics. A thermal state is not a pure state but a completely mixed state as it is a statistical mixture. We can express a thermal state with a density matrix as:

$$\rho = \sum_n p(\varepsilon_n)|n\rangle\langle n| \ , \tag{4.4}$$

where $p(\varepsilon_n)$ is the probability to detect exactly n photons in the optical mode with frequency ν. By using the average photon number this probability distribution can be expressed as [84]:

$$\begin{aligned} p(\varepsilon_n) &= \frac{\langle n\rangle^n}{(1+\langle n\rangle)^{n+1}} \\ &= \mathrm{e}^{\left(\frac{-\varepsilon_\mathrm{n}}{\mathrm{k_B T}}\right)^\mathrm{n}} \left(1 - \mathrm{e}^{\frac{-\varepsilon_\mathrm{n}}{\mathrm{k_B T}}}\right) \\ &= \frac{\mathrm{e}^{\frac{-\varepsilon_\mathrm{n}}{\mathrm{k_B T}}}}{\sum\limits_n \mathrm{e}^{\left(\frac{-\varepsilon_\mathrm{n}}{\mathrm{k_B T}}\right)}} \\ &= \frac{e^{-\beta\varepsilon_n}}{Z}, \end{aligned} \tag{4.5}$$

where Z is called the partition function and we used $\beta = 1/k_B T$.
Any state that can be written as a density matrix with only diagonal elements and weights according to equation (4.5) is called a thermal state. In this work, we want to substitute and identify the numberstates $|n\rangle$ with the OAM states $|\ell\rangle$. We can do this with the analogy between the paraxial equation and the Schrödinger equation and identifying the energies as $\varepsilon_n = \varepsilon_\ell = (|\ell| + 1)\hbar\omega$. The OAM thermal state then writes:

$$\begin{aligned} \rho &= \sum_{\ell=-\infty}^{+\infty} p(\ell)|\ell\rangle\langle\ell| \\ &= \sum_{\ell=0}^{\infty} \frac{\mathrm{e}^{-\beta(|\ell|+1)\hbar\omega}}{Z}|\ell\rangle\langle\ell| \ , \end{aligned} \tag{4.6}$$

where $|\ell\rangle$ are the LG modes and $(|\ell|+1)\hbar\omega$ their respective energies. In order to prepare photonic thermal OAM states in the lab we then have to prepare the probabilities of each OAM mode as $p(\ell) = \frac{\mathrm{e}^{-\beta(|\ell|+1)\hbar\omega}}{Z}$. Two different methods are presented in the next section.

4.3 Remote preparation of thermal states

With our analogy we can simulate energy levels with OAM single photon states. To create thermal states we have to identify each state with its respective probability $p(\ell)$ determined by Eq. (4.5). Because thermal states are an incoherent superposition of energy states we can simply prepare an OAM state for each energy level of the thermal state separately and then multiplying it with the adequate probability. This is what has been done in a previous experiment [24]. In that work, each OAM state was prepared separately, a process was applied and a final measurement was performed to see which transitions to other OAM states have occurred. Here, we want to remotely prepare a single-photon thermal state with the correct thermal detection probabilities for each OAM mode like in Eq. 4.6. This means the actual OAM state is unknown before detection. We can achieve this with two different methods; through the weighted measurement and therefore remote preparation of multiple OAM modes simultaneously, or by manipulating the amplitudes C^{ℓ_s,ℓ_i} of the SPDC process, that determine the OAM spectrum of the signal and idler photons.

4.3.1 Superposition of Hologram Masks

In the chapters 3.2 and 3.3 we showed how to use hologram masks to generate and measure the orbital angular momentum of a beam of light or a single photon. In chapter 4.1 we showed how the measurement of the OAM of the signal (idler) beam, remotely prepares the OAM of the the idler (signal) beam. Instead of measuring the signal OAM (for example $\ell_s = 3$) with a single forked hologram mask like the one shown in Fig. 3.4, lets imprint a superposition of several hologram masks in the SLM of our OAM detection scheme. Lets say we generate the masks for $\ell_s = 3$ and $\ell_s = 2$, add the grayscale images (with mod 255) and imprint the resulting image on the SLM screen. If both masks are added with equal weights then we would be able to equally measure signal OAM of $-3\hbar\omega$ and $-2\hbar\omega$ per photon. The state of the idler beam up to a normalization constant is then remotely prepared as

$$\langle \ell|_s|\psi\rangle = \left(\langle \ell=-3|_s + \langle \ell=-2|\right) \sum_{\ell=-\infty}^{\infty} C_{|\ell|}|+\ell,-\ell\rangle_{si} \tag{4.7}$$

$$= \langle \ell=-3|_s|\ell=-3\rangle_s \, C_{|\ell=3|}|\ell=3\rangle_i + \langle \ell=-2|_s|\ell=-2\rangle_s \, C_{|\ell=2|}|\ell=2\rangle_i \tag{4.8}$$

$$= C_{|\ell=3|}|\ell=3\rangle_i + C_{|\ell=2|}|\ell=2\rangle_i \; . \tag{4.9}$$

By measuring the OAM of the signal beam for two values simultaneously, we prepared the idler beam in a superposition of $\ell = 3$ and $\ell = 2$, with weights determined by the process of SPDC or rather the mode overlap integral. In order to theoretically prepare a thermal state with this technique, we need to create a superposition with an infinite number of masks and their respective thermal weights. Each mask is an image where each pixel has a grayscale value between 0 and 255. If we multiply each mask by a factor between 0 and 1 before we add the masks together, we can determine the weight it will have in the superposition. Each mask for a specific ℓ can therefore be multiplied with the coefficient $p(\ell)/C_{|\ell|}$, where $p(\ell)$ are the thermal weights defined in equation 4.5 and $C_{|\ell|}$ are the coefficients determined by the process of SPDC. The resulting single photon state in the idler beam is then

$$|\psi\rangle_i = \sum_{\ell} p(\ell)|\ell\rangle \ . \tag{4.10}$$

So in this remote preparation scheme, we use one SLM in the path of the signal photons to apply the superposition of forked hologram masks, which remotely prepares the single photon state of the idler photons. We can then use the second SLM in the path of the idler photons to measure the remotely prepared OAM distribution. As we are limited by the resolution of the SLM display, we cannot create a superposition of infinite masks. But because both coefficients $p(\ell)$ and $C_{|\ell|}$ go towards 0 for large values of ℓ, we can truncate our thermal states at a reasonable value. A measurement of the OAM spectrum of the idler beam for a thermal state prepared with this technique is shown in Fig. 4.1. With this technique we generate a state as a superposition of several OAM values, which, when measured, have the correct thermal probabilities. Therefore the states generated like this are sufficient to simulate energy levels with correct probabilities. However this is a coherent superposition and therefore results in a pure state. A *real* thermal state is a mixed state and an incoherent superposition.

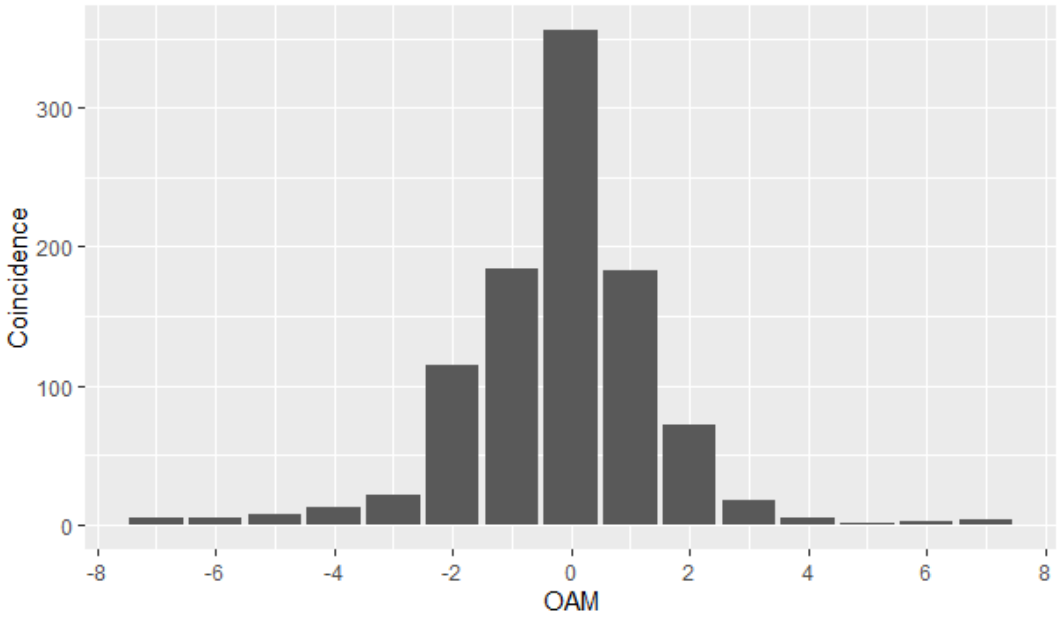

Figure 4.1: Measured OAM distribution of the idler beam, while a superposition of forked holograms was projected onto a SLM in the path of the signal photons.

4.3.2 Manipulating the OAM Spectrum of down-converted photons

In Eq. (3.25) we determined the probabilities for the different LG modes of the down-converted signal and idler photons. The OAM distribution only depends on the beam widths of the pump, signal and idler beams. In fact, there are more factors in the actual experiment that can influence this distribution, like signal and idler angles, the coupling to the fibers, and the alignment of the optical elements as well as the center of the hologram masks displayed on the SLMs in relation to the beam profiles.

As a first test and to characterize the OAM distribution, we measured the OAM for both, signal and idler, at the same time. Recording the coincidence events for every possible combination of OAM values for signal and idler, we can generate a heat map of the correlations between signal and idler OAM. Such a measurement is displayed in figure 4.2. For each measurement point, the coincidences have been recorded over the time period of 30 s. This first measurement confirms the correlations predicted by the description of the two-photon state derived in equation (3.19). If we detect a signal photon with OAM of ℓ, we find the idler photon to posses OAM of $-\ell$ with high probability. This results in the diagonal correlation in figure 4.2. In chapter 3.4 we stated that that the probability of finding a photon in the state $|\ell\rangle$ decreases with increasing $|\ell|$, following an exponential decay law and the highest probability to find signal and

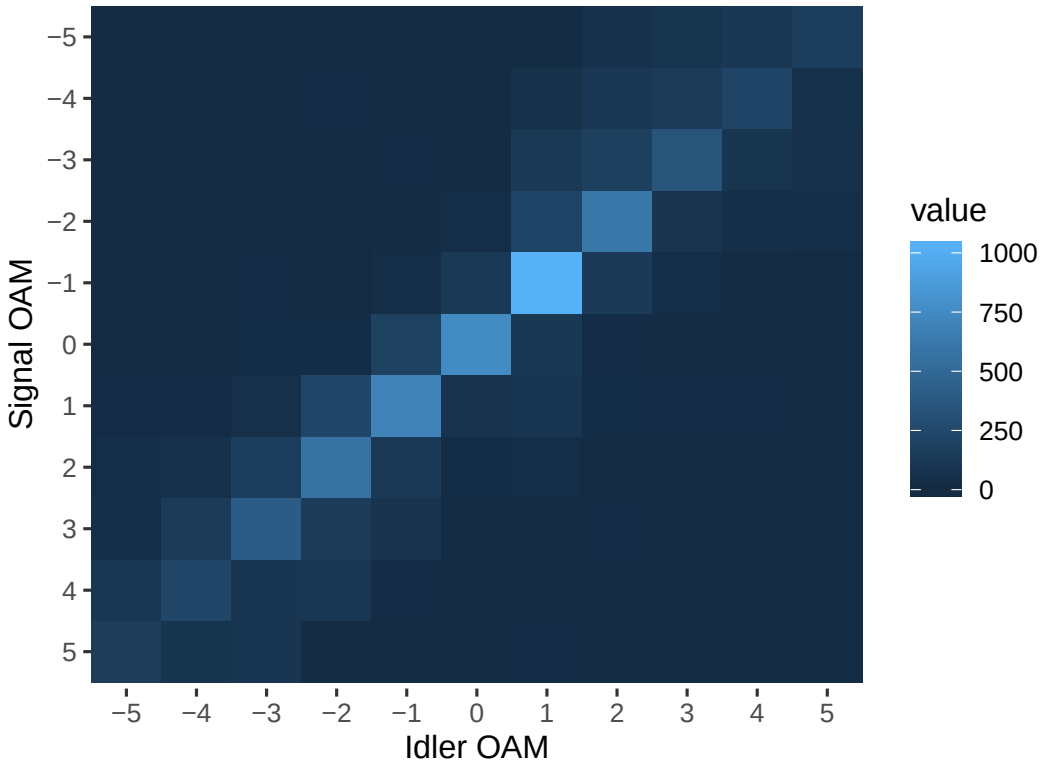

Figure 4.2: Measured OAM each combination of signal and idler OAM values. The measured OAM values range from $\ell = -5$ to $\ell = +5$ for both, signal and idler.

ider with $\ell = 0$, given that the pump as $\ell_p = 0$. This can, as well, be seen in figure 4.2. Coincidence counts for values of $\ell = \pm 5$ are only $\approx 10\%$ of those for $\ell = 0$, while the correlation persists.

Our goal is to identify this exponential decay defined by the coefficients $C_{|\ell|}$ with the exponential decay of the probabilities in a thermal state. We can write Eq. (3.19), the two-photon state as a *nonlocal thermal* state

$$|\psi\rangle_{si} = \sum_{\ell=-\infty}^{\infty} \sqrt{\frac{\mathrm{e}^{-\beta\epsilon_\ell}}{Z}} |+\ell, -\ell\rangle_{si} \ , \tag{4.11}$$

where $\beta = (k_B T)^{-1}$, the energy $\epsilon_\ell = (|\ell|+1)\hbar\omega$ and Z is the partition function. $(|\ell|+1)\hbar\omega$ gives the energy for the special case of the radial index $p = 0$. This lets us identify $\beta(|\ell| + 1)\hbar\omega$ as the ratio between the quantum of OAM (in units of energy) and the thermal energy β^{-1} [24]. Therefore equation (4.11) is an entangled state with thermal weights for entangled photons with $\ell_s = -\ell_i$, that have been generated by the process of SPDC in a nonlinear crystal.

Considering this state, we can measure the OAM of the signal photons, but remove the

OAM measurement apparatus from the idler beam. This means we are tracing over the OAM degree of freedom for the idler beam, allowing all photons with arbitrary OAM to be detected and considered for coincidence events. Therefore for the signal beam, we obtain a *remotely prepared local thermal state*, which we can write as a density matrix for the mixed state

$$\rho_s^{th} = \mathsf{Tr}_i \left(|\psi\rangle_{si} \langle\psi|_{si} \right) \tag{4.12}$$

$$= \sum_{\ell_i} \sum_{\ell=0}^{\infty} \frac{\mathsf{e}^{-\beta(|\ell|+1)\hbar\omega}}{Z} \langle \ell|_i| + \ell, -\ell\rangle_{si} \langle +\ell, -\ell|_{si} |\ell\rangle_i \tag{4.13}$$

$$= \sum_{\ell=0}^{\infty} \frac{\mathsf{e}^{-\beta(|\ell|+1)\hbar\omega}}{Z} |\ell\rangle\langle\ell|_s \ . \tag{4.14}$$

The result of a measurement of this thermal distribution is displayed in figure 4.3. The coincidences have been normalized by the partition function Z, which is the sum of all recorded coincidence for all possible values of OAM. The error bars are the standard deviation, which is the square root of the coincidence count rate for each separate mode (ℓ) respectively. The coincidences for each OAM mode were measured separately over the time period of 60 s. To this normalized measurement data we fitted

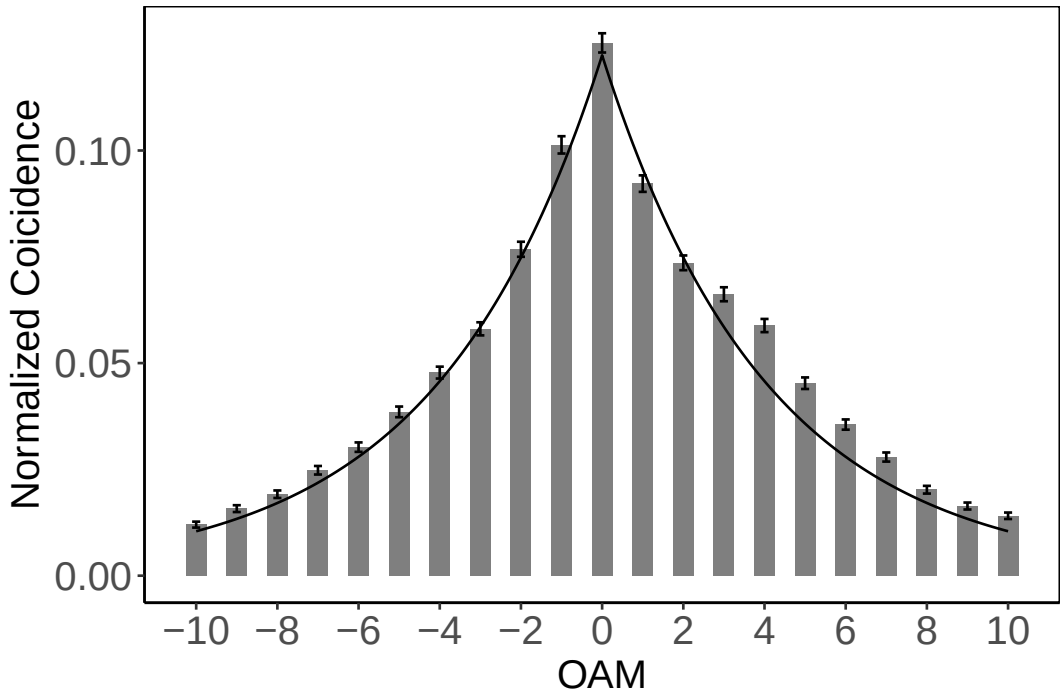

Figure 4.3: Measured OAM distribution for heralded idler photons gated by signal photons with traced OAM.

a thermal distribution like

$$p(\ell) = \frac{\mathrm{e}^{-\beta(|\ell|+1)\hbar\omega}}{Z}. \tag{4.15}$$

From this fit to our experimental data, we can directly obtain the effective temperature of the single photon thermal state, as well as the inverse thermal energy normalzied with respect to $\hbar\omega$. This temperature should not be confused with a thermodynamic temperature. The temperature inferred here concerns the parameter of the Gibbs state, which is used in the description of thermal states of quantum systems. The partition function Z defined as the sum over all possible OAM states takes a specific form as the energy levels of our thermal state have degeneracy 2, except for the $\ell = 0$. This degeneracy leads to [24]

$$Z = \left(\mathrm{e}^{\beta\hbar\omega}\tanh\frac{\beta\hbar\omega}{2}\right)^{-1}. \tag{4.16}$$

The distribution in figure 4.3 was found to have $\beta\hbar\omega \approx 0.25$. This result shows that the one photon state in the OAM basis generated by SPDC is compatible with a thermal distribution. The measured distribution exhibits an exponential decay for increasing values of $|\ell|$ and has approximately symmetric positive and negative parts. There are no coherences between those OAM states representing the energy levels of the thermal state as the single photon coherence time is shorter than the measurement of consecutive photons. This is desired as we note that a thermal state is a mixed state, a perfect statistical mixture.

4.4 Thermal State Manipulation

One idea going forward is to use these thermal states in future experiments to gain insides into processes and phenomena that include systems that have such thermal distributions of energy levels. For such purposes we are interested in not only preparing specific thermal states remotely but also prepare them in a controlled manner, making them useful for a bigger range of applications.

4.4.1 Pump beam size

In order to manipulate the single photon OAM distribution, we want to modify the amplitudes $C_{|\ell|}$ defined in equation (3.16). These amplitudes are dependent on the angular spectrum of the signal and idler beams (eq. (3.10)). The spectra are defined

by the length of the crystal (L), the normalized pump beam width ($\bar{w}_p = w_p/\sqrt{\lambda_p L}$) and the width of the LG basis [80]. We use a Gaussian monochromatic laser as our pump ($\lambda_p = const.$ and $\ell_p = 0$) and the same nonlinear crystal for all experiments ($L = const.$). This leaves as the only free variable parameters the size of the pump beam and the size of the LG mode basis of the signal and idler beams.

For this reason, we inserted a telescope in the pump beam before the crystal and left the signal and idler beam widths fixed by the size of the optical fibers they couple into. This telescope consists of two lenses with focal lengths $f_1 = 15$ mm and $f_2 = 5$ mm. This reduces the width of the pump beam by a factor of 3 compared to the measurement presented in the previous section. After the telescope was inserted, the same measurement as in the previous section was repeated. The result is shown in Fig 4.4. The black circles are the same measurement data presented in figure 2.1 for comparison.

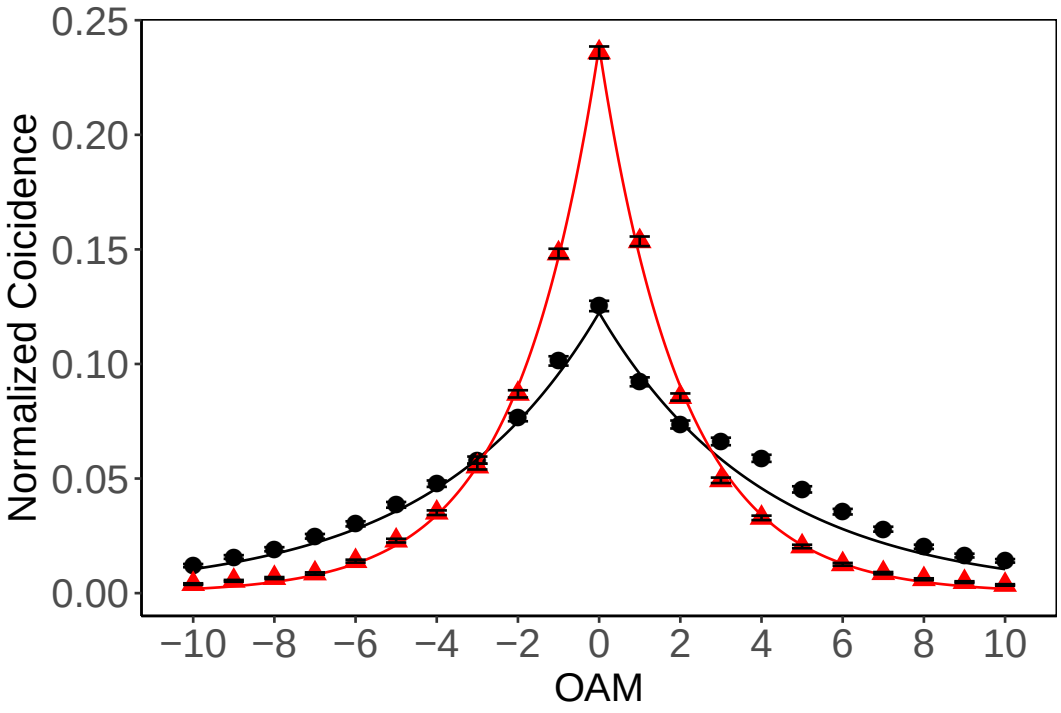

Figure 4.4: OAM distribution for heralded idler photons without (black circles) and with reduced pump beam diameter (red triangles). Thermal functions were fitted to the experimental data (solid lines).

The solid lines are the fitted thermal distributions to the experimental data. Again we find the recorded single photon OAM state to be in very good agreement with a thermal distribution. The temperature of the distribution that was calculated from the fitted function changed from $\beta\hbar\omega \approx 0.25$ to $\beta\hbar\omega \approx 0.49$. This result is similar to

the theoretically simulated results in reference [80]. Therefore we can confirm that reducing the pump beam width results in a decreasing temperature (β is the inverse temperature) associated with the single photon OAM distribution. Decreasing the beam diameter cools down the photonic mode structure.

Another magnitude related to thermal states is the average dimensionless energy defined as

$$\frac{\langle E \rangle}{\hbar\omega} = \frac{1}{\hbar\omega} \sum_{\ell} p(\ell)\varepsilon(\ell) \ , \tag{4.17}$$

where $\varepsilon(\ell) = (|\ell| + 1)\hbar\omega$ are the energies for each ℓ and $p(\ell)$ are the measured probabilities for each ℓ. The average energies for the two different pump widths are $\langle E_1 \rangle/\hbar\omega \approx 4.34$ and $\langle E_2 \rangle/\hbar\omega \approx 3.00$. Cooling down the system, therefore, results in a reduced average energy.

4.4.2 Aperture size

Another possibility of changing the spiral bandwidth of the down-converted photon states is to vary the maximum size of LG modes that can be detected. We have stated before that the size of the LG basis is fixed by the diameter of the optical fiber. This is true for the signal beam where we perform the OAM measurements. For the idler beam we removed the OAM measurement apparatus and specifically the optical fiber connecting the idler beam to the detector. Instead we direct idler photons directly onto the single photon detector which results in the trace over all possible OAM states. This allows all idler photons with any value of OAM to be detected at any time. An iris is placed at the opening of the single photon detector. This iris can be closed or opened to decrease or increase the aperture diameter. We detect all idler photons with a fully opened detector, which doesn't discriminate between different OAM modes. As we are preparing the thermal single photon state remotely, we can vary the aperture size of the idler photon detector. Decreasing the diameter of the aperture changes the size of the LG modes that are able to be recorded by the photon detector. Changing the width of the idler LG modes then in return changes the spiral bandwidth of the idler beam or their OAM distribution. Because the signal and idler OAM spectra are entangled due to the phase matching properties, we can vary the diameter of the idler detector aperture to modify the OAM distribution of the measured signal photons. This works through the same mechanism as the *remote* preparation of the signal or idler OAM. With an opened detector we performed the trace over all OAM modes. Now we perform the

partial trace, reducing the detection probability of higher order modes with greater $|\ell|$. This can be understood in two different ways. The coefficients $C_{|\ell|}$ determined by the overlap integral in Eq. (3.25) for coincidence counts predict lower probabilities for higher order modes when the beam widths are reduced. This was true for the reduced pump beam width as we have seen in the previous section, and we expect a similar trend here. On the other hand, closing an iris and therefore limiting the aperture size of the detector doesn't result in a true *decrease* of all possible modes. Instead this results in a cut-off of higher order modes. Higher order LG modes of the same family have a bigger width due to the exponential of $|\ell|$ in the expression of the complex amplitude of LG modes in Eq. (2.21). This can also be seen in the plot of the intensity profiles of the first few order in Fig. 2.2. Anyhow, this should have the same effect as reducing the LG mode width, resulting in a greater inverse temperature β for the resulting thermal state. We varied the detector aperture size from completely opened to $1.5\ \mathrm{mm}$, to $1.0\ \mathrm{mm}$ and $0.58\ \mathrm{mm}$. For each aperture diameter size, we perform the same OAM distribution measurement for the signal photons as before. The results of those measurements are shown in Fig. 4.5.

The coincidence counts have been normalized with the partition function. The solid lines are the thermal distributions that have been fitted to the experimental data.

All measured distributions still follow a thermal distribution, even with the smaller aperture diameter. We see that the temperature of the distributions decreases with smaller aperture sizes. In the limit of a closed detector aperture, the system's temperature tends towards zero. A thermal state of temperature zero would be a pure state with the only contribution being $\ell = 0$. This makes sense, because LG modes with $\ell \neq 0$ have zero intensity in the center of the beam. If it were possible to close the aperture to point size, the only contribution would be from the mode $\ell = 0$, therefore resulting in the thermal state with infinite inverse temperature.

We note that the distributions are becoming increasingly asymmetrical for smaller aperture sizes as well as diverging from the ideal thermal distribution, therefore being out of equilibrium. This is due to the experimental alignment. The spatial profile of the LG modes as well as the aperture are of circular shape. Due to experimental imperfections, the shape of the LG modes could become elliptical and the circular aperture doesn't exclude modes with positive and negative ℓ to the same extent. Another reason is that the forked hologram projected onto the SLM is not perfectly in the center of the down-converted signal beam. Leading to asymmetrical measurement results for modes with positive and negative ℓ.

The divergence from the ideal thermal distribution can be quantified to provide a figure

of merit of the quality of the prepared OAM distributions. The deviation compared to the ideal equilibrium thermal state can be numerically expressed by the Kullback-Leibler (KL) divergence. It is defined as

$$D_{KL}\left(p_f(\ell)||p_m(\ell)\right) = \sum_{\ell} p_m(\ell) \log\left(\frac{p_m(\ell)}{p_f(\ell)}\right) , \tag{4.18}$$

where $p_f(\ell)$ and $p_m(\ell)$ are probability distributions. We can now calculate the KL divergence for our measured probabilities and the probabilities taken from the fitted thermal distribution. The results of the performed calculations on the measured data are summarized in table 4.1.

As we decrease the aperture size we see an increase in the inverse temperature β,

Table 4.1: Calculations performed on measured data.

Aperture size	inverse temperature (β)	average energy ($\langle E \rangle$)	KL divergence
opened	0.35	3.40	0.014
1.5 mm	0.59	2.51	0.015
1.0 mm	0.77	2.33	0.036
0.58 mm	0.84	2.23	0.054

meaning a cooling down of the system. At the same time, this results in a decreasing average energy. For the completely opened detector, we calculated the KL divergence to be 0.014 which is approximately a thermal state. For the almost complete closed detector aperture with a 0.58 mm diameter, we calculated the KL divergence as 0.054. This shows the increased deviation from the ideal equilibrium thermal state for smaller aperture diameters, while the output is still not far from a thermal state concerning the populations.

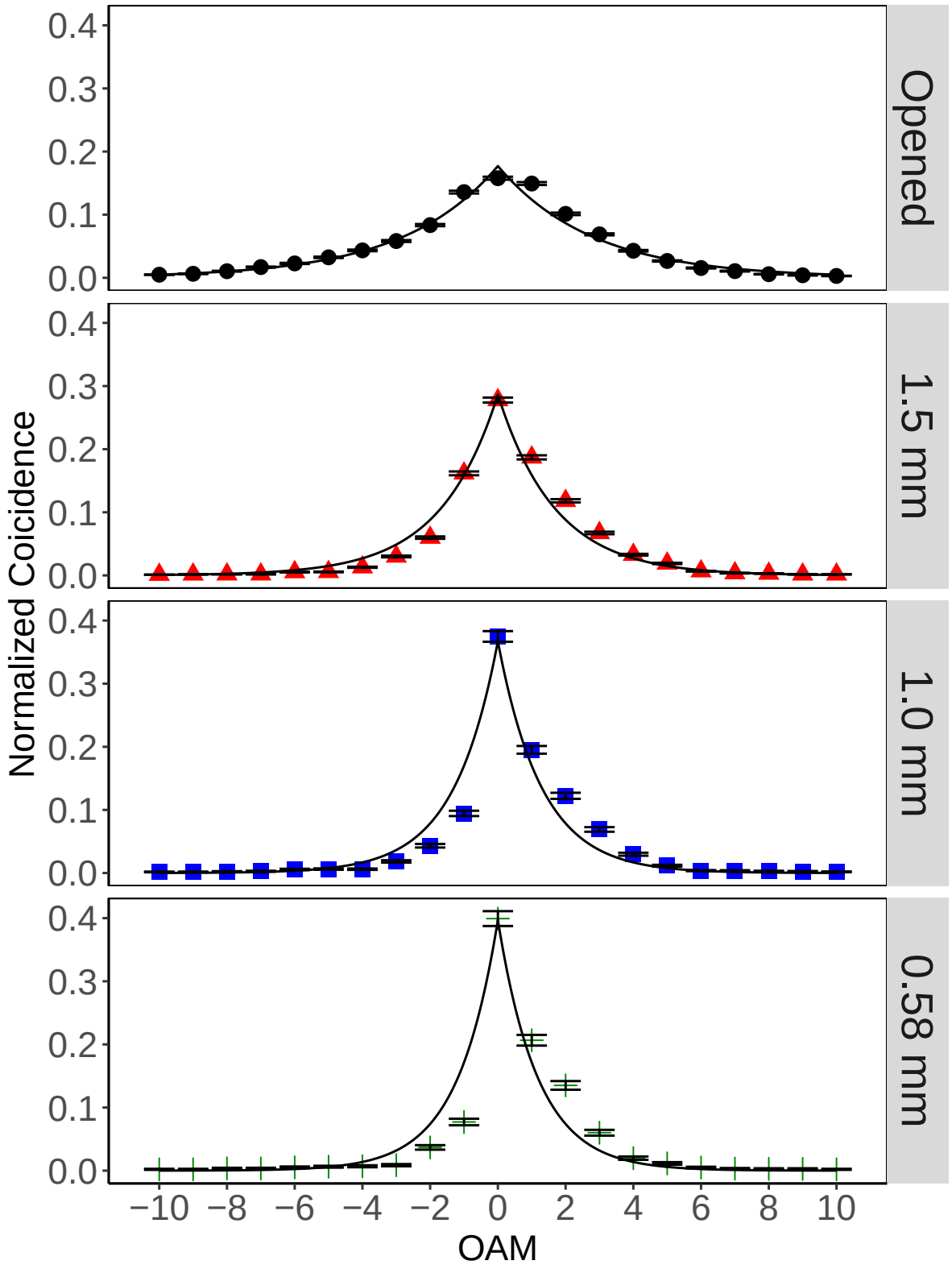

Figure 4.5: OAM distributions for different aperture sizes before the photon detector; opened detector (discs), 1.5 mm (triangles), 1.0 mm (squares), 0.58 mm (crosses). Thermal distributions were fitted to the experimental data (solid lines).

4.4.3 Fresnel lens

In the previous section we changed the LG mode width of the down-converted signal and idler beams by limiting the aperture size of the photon detector. As mentioned this actually only limits the detection of higher order modes, even though resulting in the desired effect on our prepared thermal states. Another way of changing the size of the LG mode family is through lenses. If we want to insert a lens in the beam path of the signal or idler photons without changing our alignment we can do this by implementing a Fresnel lens on one of the SLMs. The idea of a Fresnel lens is as if you'd collapsed a conventional lens into a flat surface while maintaining the curvature of the original lens. An illustration is shown in Fig. 4.6 a). Such a lens can be directly implemented on a SLM screen by a phase only modulation. If we create such a mask and as usual create a grayscale image with values from 0 to 255 we get an image as the one in Fig. 4.6 b). The mod 255 function creates the characteristic rings, that are different from the circular areas in the physical lenses.

We then repeat the same measurement as in the last section. Measuring the OAM

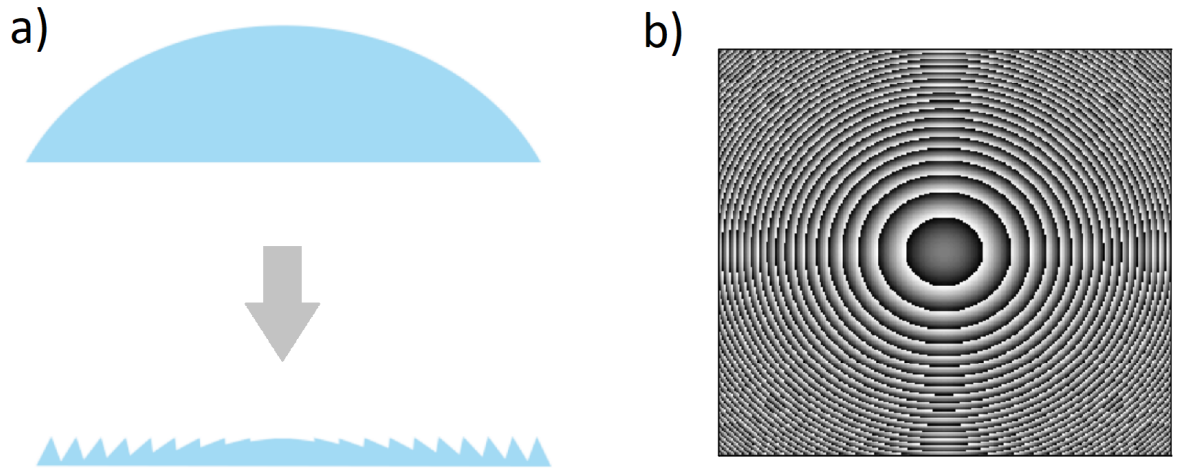

Figure 4.6: a) Illustration of the main idea of a Fresnel lens. A optical lens is collapsed into a flat structure while maintaining as much of the surface slope of the original lens as possible. b) Computer generated phase mask to implement a Fresnel lens on a SLM.

of the signal photons with an optical fiber and a SLM, while focusing the idler beam with a Fresnel lens. The results for such measurements are shown in Fig. 4.7. We recorded the OAM distributions of the signal photons for detected coincidence events. The first measurement was without a lens for reference, then we used a lens with focal length $f = 1.5$ m and a lens with $f = 1.0$ m. A stronger focus decreases the size of the beam width. From the measurements we can see that a stronger focus leads to a increased inverse temperature β for the fitted thermal distribution. The fitted

values for the thermal distributions were $\beta_1 = 0.27$, $\beta_2 = 0.39$ and $\beta_3 = 0.49$, for no lens, $f = 1.5$ m and $f = 1.0$ m, respectively. The effect of the lens also reduces the energy of the thermal states from $\langle E_1 \rangle = 4.21\hbar\omega$, to $\langle E_2 \rangle = 3.52\hbar\omega$ and $\langle E_3 \rangle = 3.22\hbar\omega$. This behaviour is expected by evaluating the overlap integral of the SPDC process for coincidence events, and is in agreement with the measurements presented in the previous sections.

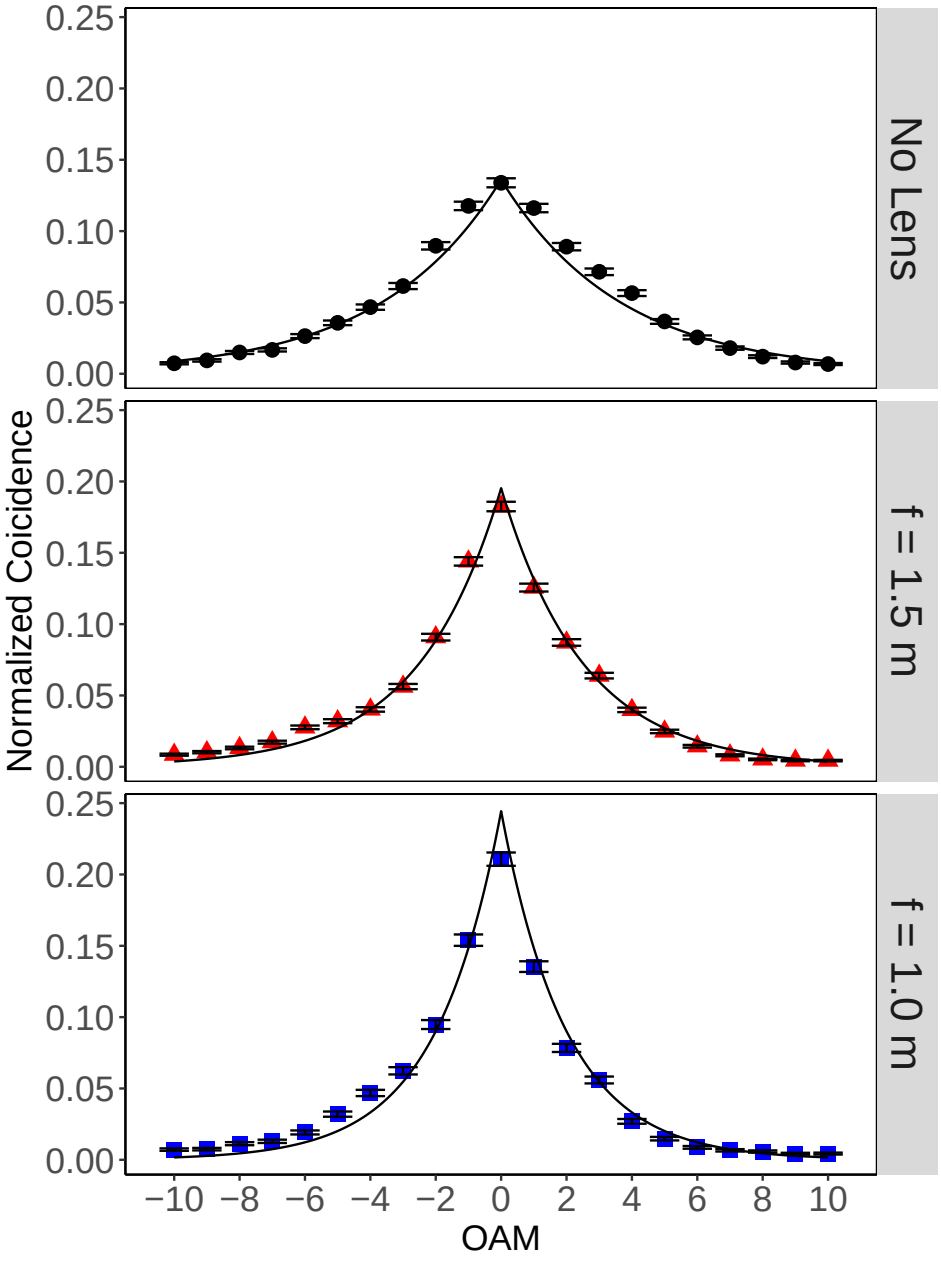

Figure 4.7: Measured signal photon OAM distributions for different focal lengths of a Fresnel lens in the beam path of the idler photons; without a lens (black discs), focal length $f = 1.5$ m (red triangles), focal length $f = 1.0$ m (blue squares). Thermal distributions were fitted to the experimental data (solid lines).

4.4.4 OAM multiplication through spiral transformations

The underlying idea for the *mode sorter* device, which we used in earlier experiments to measure the OAM of a beam of light are spiral transformations [66]. An improved version, that solved the problem of mode overlap is still used for numeric simulations of our experiments [67]. The same technique of spiral transformations can be used to multiply the OAM of a beam of light [85].

The OAM of a light beam is determined by the helicity of the phasefront of the beam. Therefore a spiral transformation that would *twist* or *loosen* the circular phase gradient, will result in an increased or decreased OAM. We can therefore call this spiral transformation a multiplication or division of OAM. An illustration showing the schematics of such transformations is shown in Fig. 4.8, which was taken from the original paper by Wen *et al.* [85]. The figure shows the example of a transformation between $\ell = 3$ and $\ell = 2$.

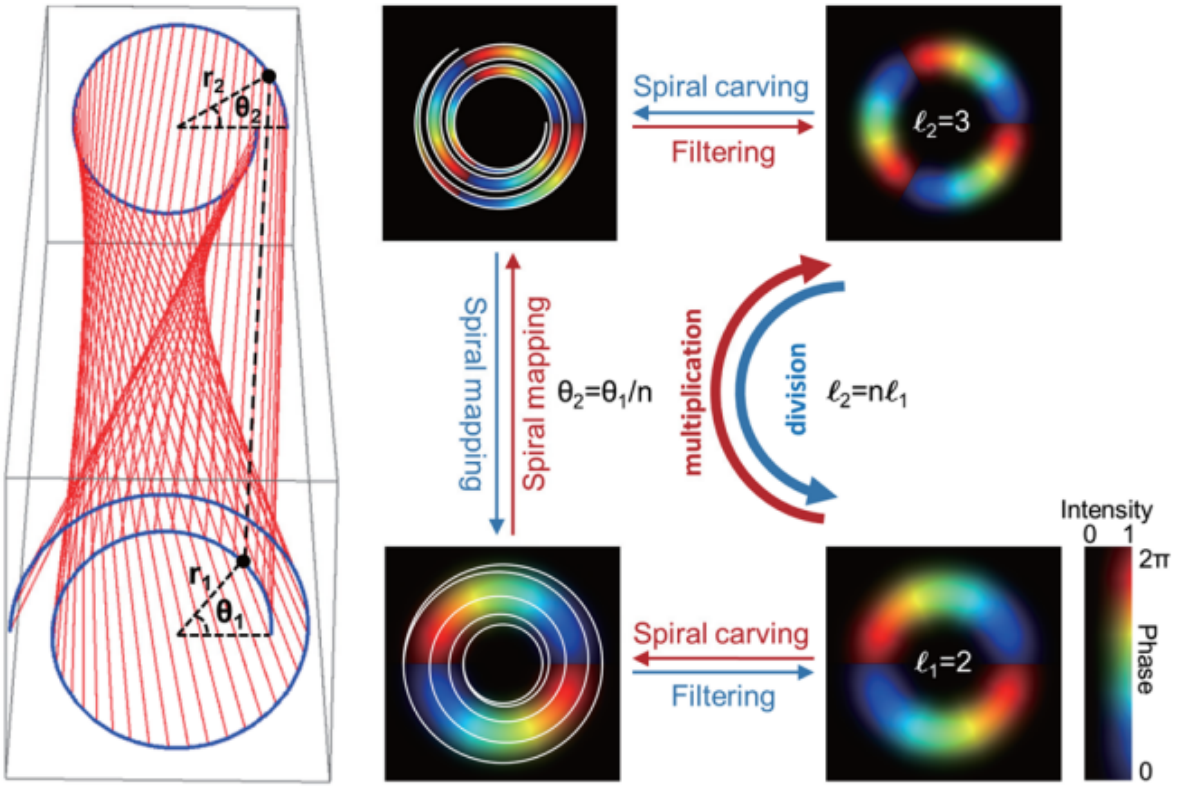

Figure 4.8: Illustration of the spiral transformation that results in an OAM multiplication or division. Shown is the example of a spiral mapping between the modes $\ell = 3$ and $\ell = 2$. Image taken from Ref. [85].

Even though the OAM is discrete, we can multiply or divide OAM by any rational factor. If the resulting OAM is not an integer, the transformed beam will end up in a superposition state of different values ℓ. For example, a LG beam with $|\ell = 3\rangle$ that is transformed with the factor $n = \frac{1}{2}$, will be in the superposition $\frac{1}{\sqrt{2}}|\ell = 1\rangle + \frac{1}{\sqrt{2}}|\ell = 2\rangle$. These transformations can be achieved through a phase mask displayed on a SLM. We can then apply this transformation to our thermal OAM states. In Fig. 4.9 is the result of a numeric simulation for such a spiral OAM multiplication applied to a thermal state.

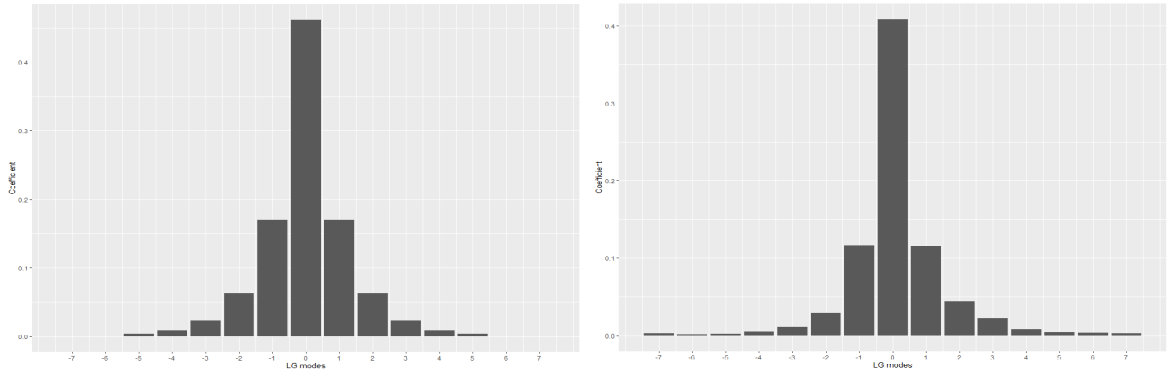

Figure 4.9: A thermal state with $\beta = 1$ was produced as an input state (on the left). It then passed through the spiral transformation performing the OAM multiplication with the factor $n = 0.8$. The final OAM distribution is shown on the right.

A thermal state with inverse temperature $\beta = 1$ was prepared and then an OAM multiplication with the factor $n = 0.8$ was applied. We can see the inverse temperature increased as the higher order contributions decreased. To show the overall impact of this kind of transformation on different input thermal states we performed the simulation for different input states and different multiplication factors. The results are shown in Fig. 4.10.

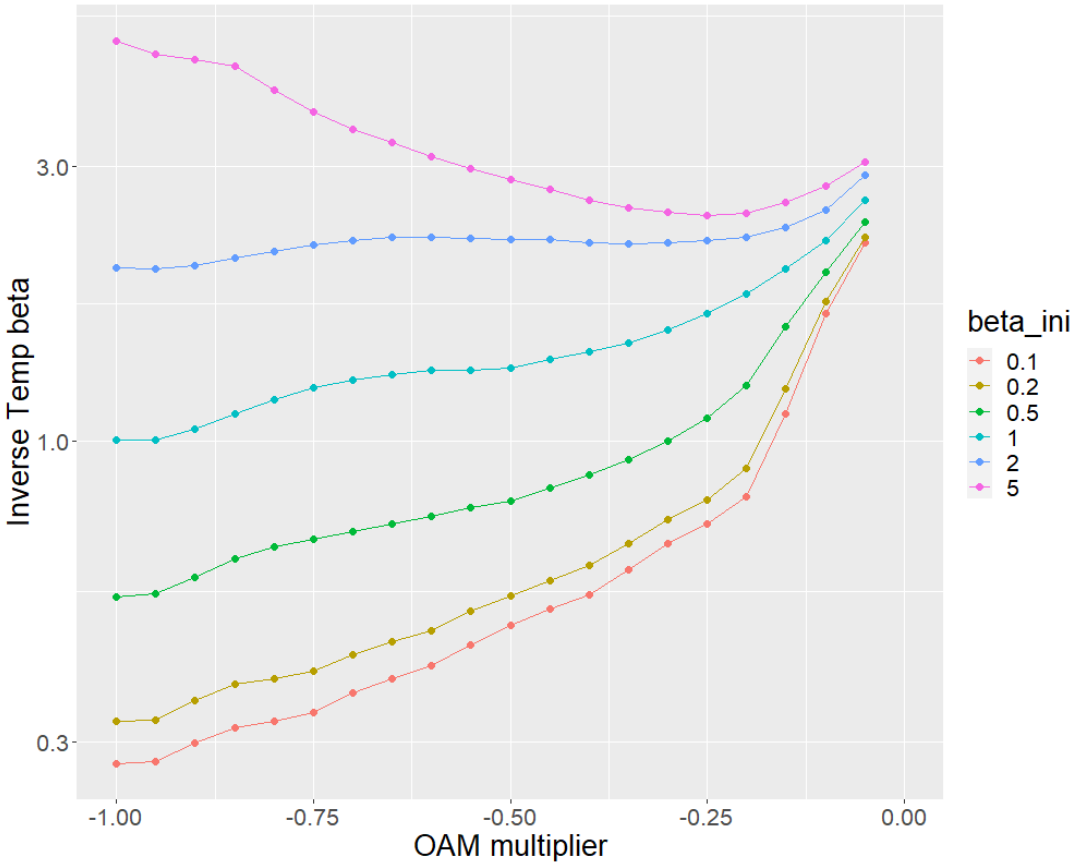

Figure 4.10: Plot of the OAM multiplication for different input thermal states. Different input temperatures are in different colors and connected by lines. the inverse temperature β has been plotted over the multiplication factor n.

We can see for different input inverse temperatures β that for small enough OAM multiplication factors, the resulting distributions tend towards large β. For those distributions with large β the almost only contribution is the mode with $\ell = 0$.

4.5 Turbulence

We have seen how we can use the OAM multiplication as a process to change the temperature of our simulated thermal states. Another process that changes the temperature of a thermal state is turbulence. As we are working with an optical setup, the investigation of atmospheric turbulence to beams of light seems like a natural choice. The process of turbulence can couple input modes to different output modes in a random fashion. This random coupling between modes can be seen as a sort of fluctuation, which is of great interest to thermodynamics, especially quantum thermodynamics, where fluctuations become crucial. This makes the turbulence interesting to us for two different reasons; first as a process to manipulate and prepare the temperature of a thermal state, which we will show in this section, and second as a thermodynamic process acting on a thermodynamic system presented in the next chapter. In our experimental platform we can mimic the process of a system being disturbed by turbulence with a pseudo-random phase-mask projected onto a SLM.

4.5.1 Statistics of Atmospheric Turbulence

In atmospheric turbulence, small turbulent areas are mixing the air, resulting in slightly different temperatures, which leads to different pressures in those areas and therefore different refractive indices. A beam of light passing through such areas then gets distorted by such fluctuations of the refractive indices. This random process can be described by the refractive index structure function [86]

$$D_n(\boldsymbol{r}_1, \boldsymbol{r}_2) = C_n^2 \left\|\boldsymbol{r}_1 - \boldsymbol{r}_2\right\|^{2/3} \ , \tag{4.19}$$

where C_n is the constant refractive index structure parameter characterizing the strength of the fluctuation. Equation (4.19) describes the spatial variation in the difference of refractive index as a function of separation. This means the function $D_n(\boldsymbol{r}_1, \boldsymbol{r}_2)$ calculates the difference of the refractive index between the two positions in space $\boldsymbol{r}_1$ and $\boldsymbol{r}_2$. Such refractive index fluctuations then induce energy dissipation and phase fluctuations. It was Kolmogorov who characterized such atmospheric turbulent processes by what is now called *Kolmogorov statistics* [87]. In turbulent processes, energy is transferred from big scales to smaller scales leading to non-linear dynamics of the system. This energy transfer is called an energy cascade. Kolmogorov described this energy cascade and dissipation where low wavenumbers transfer energy to higher

wavenumbers, which lead to the universal expression for the energy spectrum:

$$E(k) = C\varepsilon^{2/3}k^{-5/3} \,, \tag{4.20}$$

where C again is the constant structure parameter, ε is the dissipation rate and k the wavenumber. This assumption of energy cascade then yields the expression for the phase power spectrum

$$\begin{aligned} \Phi(k) =& 0.0097k^2C_n^2k^{-11/3} && (4.21)\\ =& 0.023r_0^{-5/3}k^{-11/3} \,. && (4.22) \end{aligned}$$

The second line is the expression rewritten by Fried [88] in terms of the Fried parameter r_0 which can be written as [89]

$$r_0 = 0.185\left(\frac{\lambda^2}{C_n^2 z}\right)^{3/5} \,, \tag{4.23}$$

where λ is the wavelength and z the distance of propagation. Using this phase power spectrum we find an expression for the phase structure function like we did for the refractive index:

$$\begin{aligned} D_\Phi =& 2\int_0^\infty \Phi(k)(1-\cos(2\pi kr))dk && (4.24)\\ =& 6.88\left(\frac{\delta r}{r_0}\right)^{5/3} \,, && (4.25) \end{aligned}$$

where $\delta r = \|\boldsymbol{r}_1 - \boldsymbol{r}_2\|$ is the distance between two points in space. This equation determines the variation of the phases between two spatial positions $\vec{r_1}$ and $\vec{r_2}$. This means that beam of light (with a two-dimensional transverse profile and one dimension of propagation), that passes through a atmospheric turbulence, receives relative phase differences described by the Kolmogorov statistics in Eq. (4.25). If we then compare the phase distribution of the beam before and after the beam passed through the turbulence, we can look at this three-dimensional atmospheric turbulence as a mapping between two two-dimensional phase distributions. We can therefore use this statistical description of three-dimensional atmospheric turbulence to simulate such turbulence through a single two-dimensional phase mask [90].

To do so, we pseudo-randomly generate a grayscale image, where the values of every two points of distance δr are determined by equation (4.25) for a fixed value for the Fried parameter r_0, determining the scintillation strength. A result of such a

turbulence mask is shown in Fig. 4.11. This mask is pseudo-random, because the code that was written to generate such a mask uses a pseudorandom number generator. Therefore setting a seed before executing the algorithm would always result in the same turbulence mask, which would always result in the same mode coupling. This

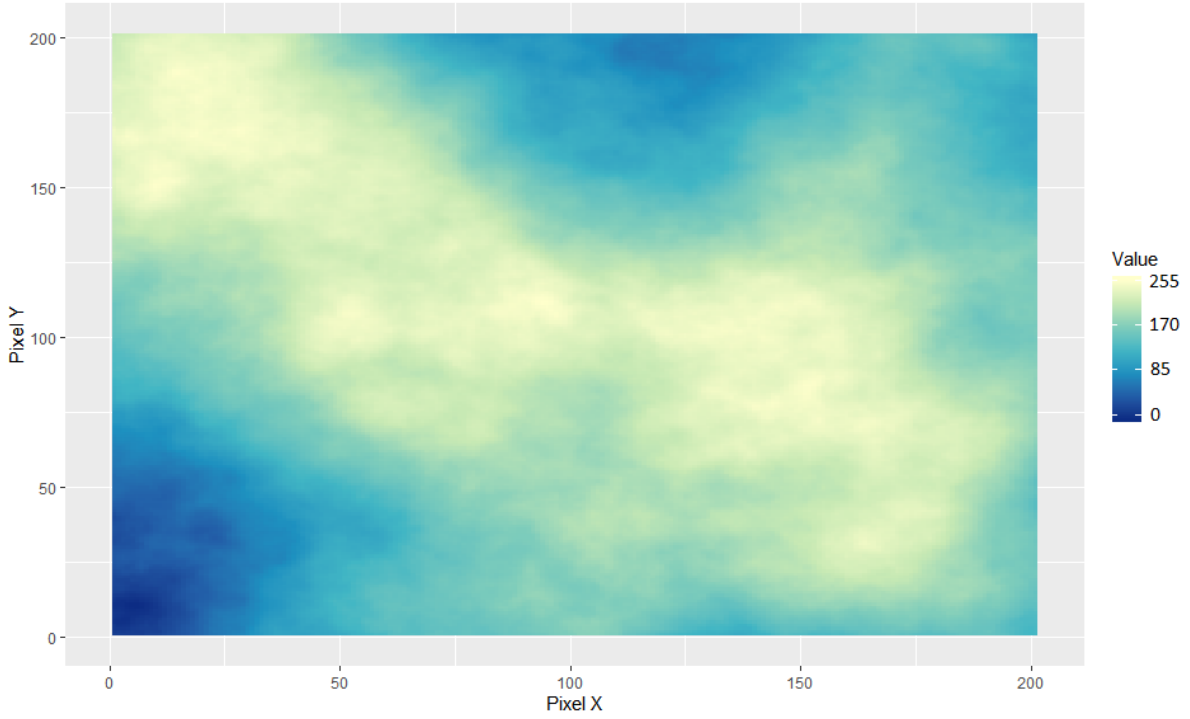

Figure 4.11: Pseudo-random generated two-dimensional phase mask, simulating the effects of an atmospheric turbulence. To display such masks on the SLM every pixel has a 8-bit grayscale range for possible values between 0 and 255.

turbulence mask can now be projected on the SLM. The SLM then modulates the phase of the beam of light hitting the SLM display differently in every pixel according to the phase mask. The SLM with the turbulence phase mask is then placed in the path of the down-converted idler photons. This flat 2-D phase mask simulates the idler photons passing through a weak atmospheric turbulence.

4.5.2 Effect of Turbulence

First we prepare an OAM thermal state in the same way as explained in section 4.3 through the process of SPDC and measuring the OAM spectrum of the signal photons. The time-entangled idler photons are used only for triggering the coincidence measurement. We repeat the same measurement by preparing the same thermal state but simulate the signal photons passing through a weak atmospheric turbulence by

applying a Kolmogorov phase mask to the SLM in the path of the signal photons. Again, we measure the OAM distribution of the signal photons, using the idler photons for coincidence counts. The results are shown in Fig. 4.12.

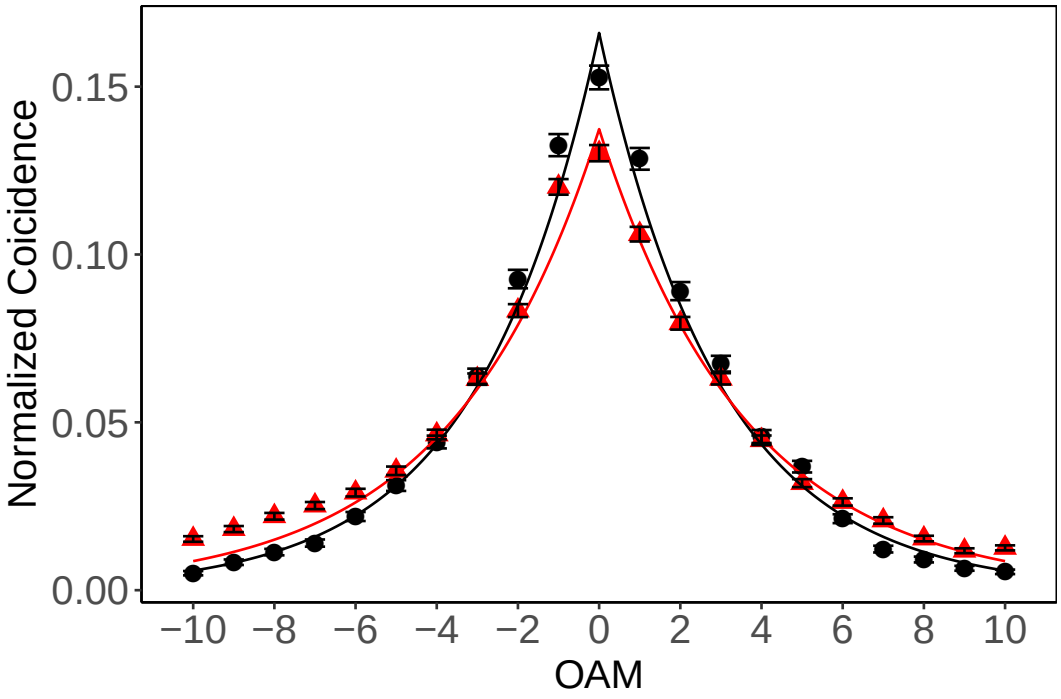

Figure 4.12: Measured OAM distribution for heralded signal photons without (black circles) and with (red triangles) a weak atmospheric turbulence. A thermal distribution was fitted to the experimental data.

The solid lines are the thermal distributions that have been fitted to the experimental data. For the initial thermal state (black circles) we found an inverse temperature of $\beta \approx 0.34$, the average energy $\langle E \rangle = 3.56\ \hbar\omega$ and the KL divergence $D_{KL}(i) \approx 0.015$. After the turbulence has been applied, we found the inverse temperature of the output state to be $\beta \approx 0.28$, the average energy $\langle E \rangle = 4.13\ \hbar\omega$ and the KL divergence $D_{KL}(i) \approx 0.027$.

Looking at the KL divergence we can see the input state is approximately a thermal state. Even though the output state is slightly out of equilibrium, it is not far from a thermal state. The process of turbulence increased the temperature and the average energy of the distribution.

This can be understood by looking at the case of a thermal state at zero temperature as the input state. Zero temperature, or infinite β, means the thermal state is equal to a Gaussian mode with only $\ell = 0$, our initial state is therefore in a single mode with zero OAM. Subjecting this state $|\ell = 0\rangle$ to a turbulence will then ”spread” into higher order

contributions ($\ell \neq 0$) resulting in a heating up of the thermal state.
To compare the effects of different turbulence strengths on different initial thermal states, we performed a series of measurements similar to the one described before. We prepared thermal states with initially different inverse temperatures β and subjected them to increasingly stronger turbulences (smaller Fried paramter). After we measured the resulting OAM distribution like in the measurement presented before, we calculated the inverse temperature β by fitting the thermal distribution. The inverse temperature was plotted over the Fried parameter for different initial thermal states. The result is shown in Fig. 4.13.

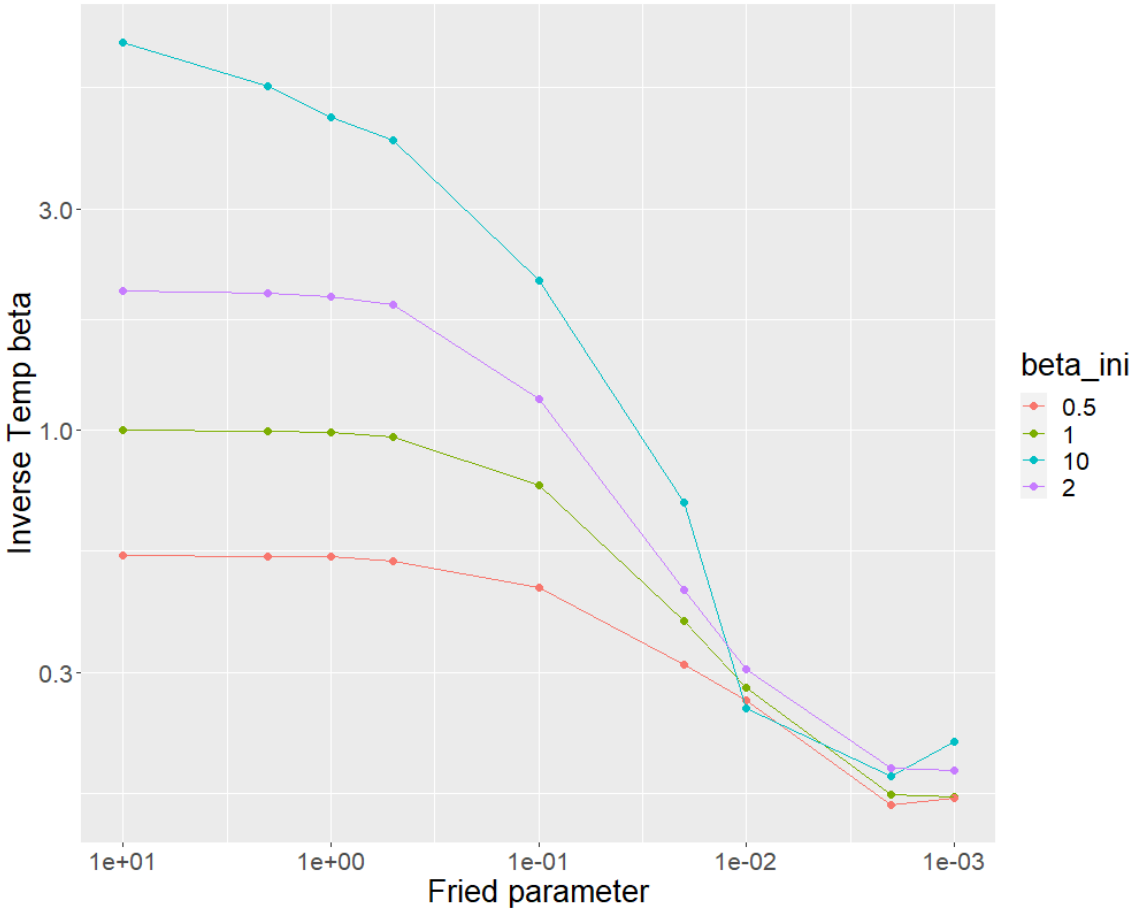

Figure 4.13: Thermal states were initially prepared with different inverse temperatures β. An atmospheric turbulence with different scintillation strengths was applied to the thermal states (a smaller Fried parameter results in a stronger turbulence). The same initial states are of the same color and connected by lines for easier visability.

We can see again, that a stronger turbulence results in a heating up of the thermal states, or a smaller inverse temperature β. For very large turbulence strengths the thermal states all tend towards infinite temperature. This is the case when all modes, or energy levels in our analogy, are equally probable occupied.

4.6 Non-Classical Thermal States

4.6.1 Coherent thermal state

A thermal state is a mixed state with no coherences between the separate contributions. In our analogy, the single photon OAM thermal state is an incoherent superposition of all OAM modes $|\ell\rangle$. We achieved this by measuring each mode separately and integrate over time, therefore adding them incoherently. In Sec. 4.3.1 we showed how to prepare a thermal distribution by projecting a superposition of masks on the SLM such as

$$\mathcal{L} \rightarrow \sum_m c_m \left(\mathcal{L}_{+m} + \mathcal{L}_{-m}\right) \ . \tag{4.26}$$

where the coefficients $c_m = (\mathrm{e}^{-\beta\epsilon_m})/Z$ follow a thermal distribution. This will prepare a state in the form of

$$|\psi\rangle = \sum_{\ell=-\infty}^{\infty} \frac{\mathrm{e}^{-\beta\epsilon_\ell}}{Z}|\ell\rangle \ , \tag{4.27}$$

with $\epsilon_\ell = (|\ell|+1)\hbar\omega$. Like this all OAM modes are generated in a coherent superposition. A OAM measurement of such a coherent thermal state is shown in Fig. 4.14 (black distribution). When we measure the OAM spectrum of the signal or idler beams, we count single photons, which we always detect in a single OAM mode $|\ell\rangle$. Therefore the populations still exhibit the exponential decay described by a thermal distribution, because the different modes don't interfere. The coherences between OAM modes are not measured by detecting only the populations of different OAM modes through single photon detection. However the coherence between the different OAM modes become noticeable when we perform a process on the superposition state, enabling coupling between the modes and introducing interference effects.

4.6.2 Effect of Turbulence on coherent thermal states

To show such effects we remotely prepare the signal photons in a coherent thermal state by applying a superposition of phase masks (see section 3.2) to the SLM in the path of the idler mode. Idler photons are then detected with a bucket photon detector, tracing over the OAM degree of freedom. We use the other SLM in the path of the signal photons for the OAM measurement scheme. We can add a turbulence phase masks to this SLM in order to simulate the single photon coherent thermal state

propagating through a weak atmospheric turbulence.

Fig. 4.14 shows the OAM measurements for a coherent thermal state that propagated through an atmospheric turbulence. The black distribution was recorded without turbulence for reference. The red and blue distributions were recorded with different turbulence masks but the same turbulence strength. As the process of turbulence is of statistical nature, every time we generate a turbulence mask it will look different even though it follows the same statistics. We note that the measured distributions are far out of equilibrium as the turbulence seems to have a much stronger effect on the coherent thermal state compared to the thermal state in the previous section. The two distributions are very different even though they were subjected to a turbulence with the same scintillation strength. This is due to the interference effects caused by the coherences between the modes. It was previously shown that the entangled OAM states keep their coherences even through turbulence [91]. Therefore, different turbulence masks introduce different phase modulations which cause different interference effects, resulting in distinct OAM distributions.

We repeated this measurement for several different turbulence phase masks for the same scintillation strength (like the red and blue distributions in Fig. 4.14). We then sum over those recorded distributions. In Fig. 4.15 is the distribution without turbulence and the distribution after averaging over 10 recorded measurements. The distribution after averaging over several measurements tends to return to a thermal distribution, exhibiting the exponential decay. By measuring just the populations of the OAM modes we do record the effects of interference on the population but we discard the information of coherences between the OAM modes. Summing over the recorded populations is then equal to an incoherent superposition. Without coherences, we return to the thermal state which is a completely mixed state without coherences.

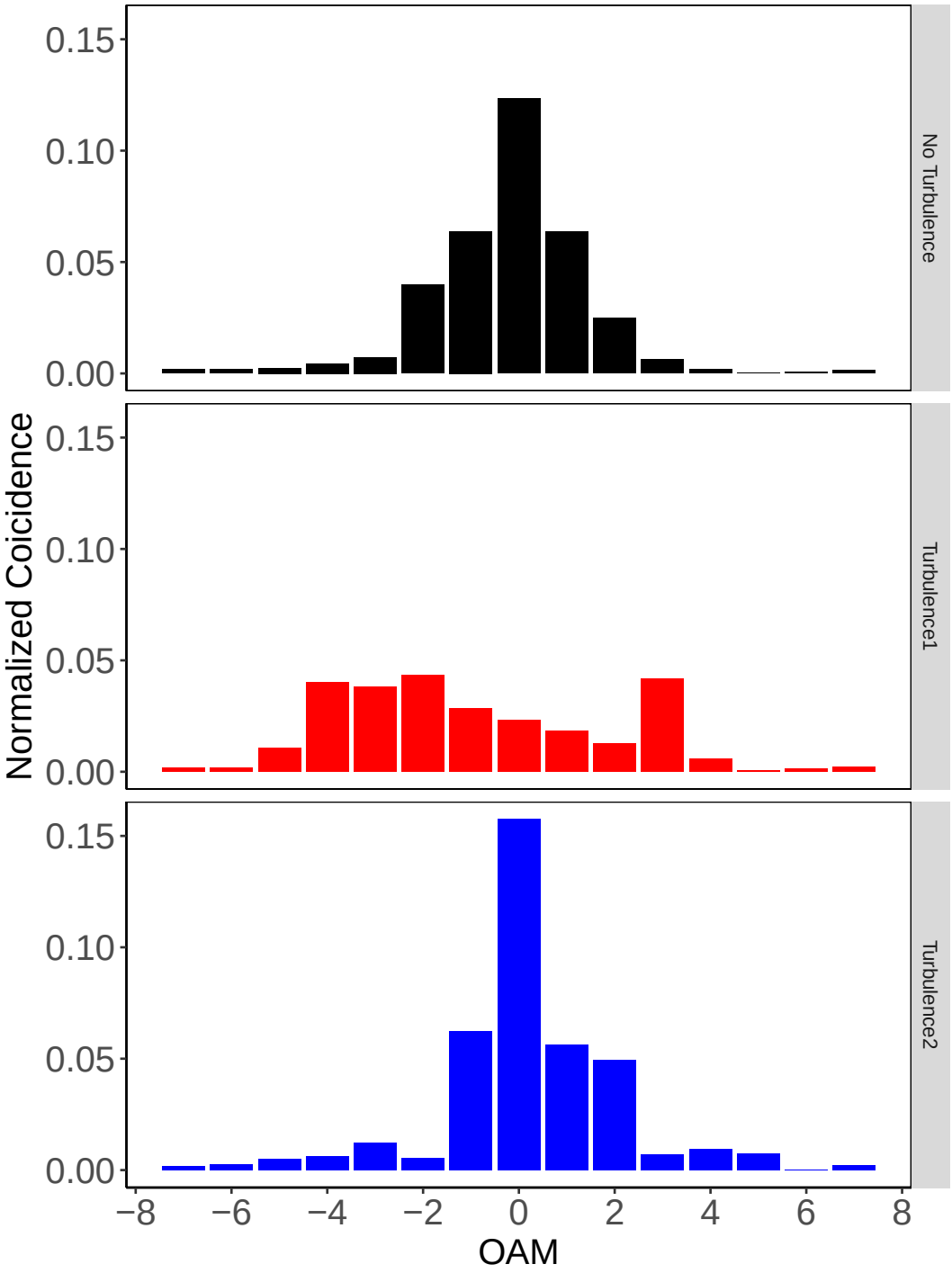

Figure 4.14: Measured OAM distribution for heralded idler photons without (black circles) and with (red triangles) a weak atmospheric turbulence. A thermal distribution was fitted to the experimental data.

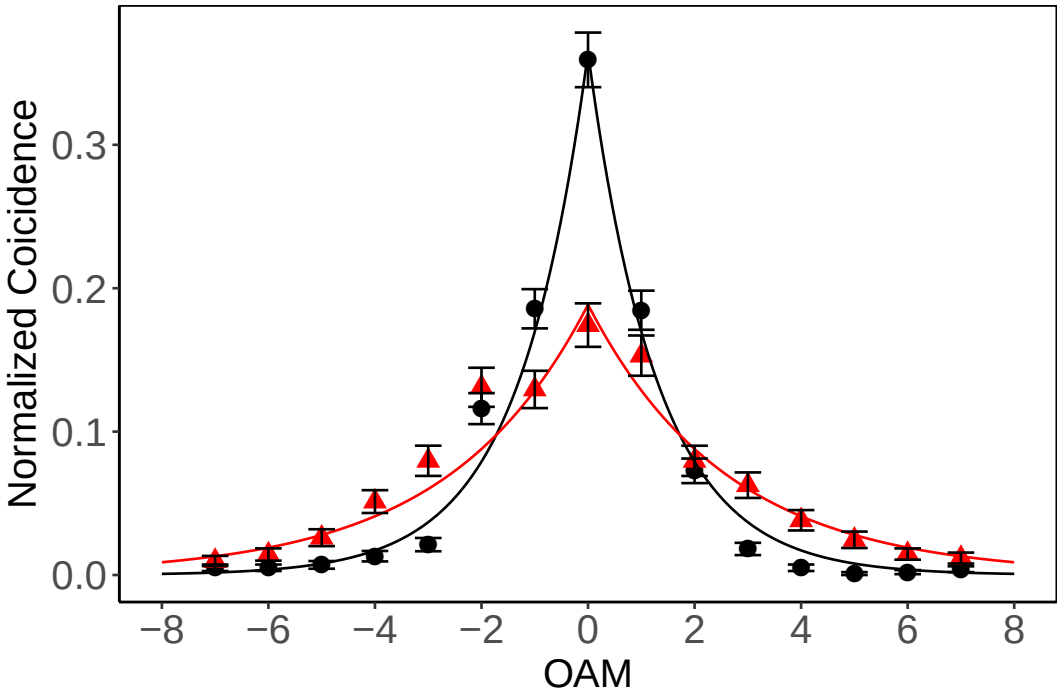

Figure 4.15: OAM distribution for the heralded signal photon of the unperturbed coherent thermal state (black discs). OAM distribution after averaging over several measurements with different turbulence masks of the same scintillation strength (red triangles).

4.6.3 Pump beam with OAM

As we have shown in a previous chapter, pumping a non-linear crystal with a Gaussian laser beam generates a thermal distribution in the OAM degree of freedom of the signal and idler beams. In this measurement we show the change of the down-converted OAM spectrum when the pump beam has an OAM ($\ell \neq 0$).
We placed a vortex phaseplate in front of the BBO crystal and passed the Gaussian laser beam through it. The phaseplate used was the $m = 2$ Zero-Order Vortex Half-Wave Retarder from ThorLabs. These plates are also called q-plates. The phaseplates generate radially and azimuthally polarized light from linearly polarized light source. Our linearly polarized Gaussian laser beam receives a helical phase of exp$(\pm 2im\phi)$, which generating an OAM equal to $\ell = \pm 2$. This vortexplate does not generate a LG mode, but a superposition of such modes. The phase and intensity profiles generated from a Gaussian beam are shown in Fig. 4.16.

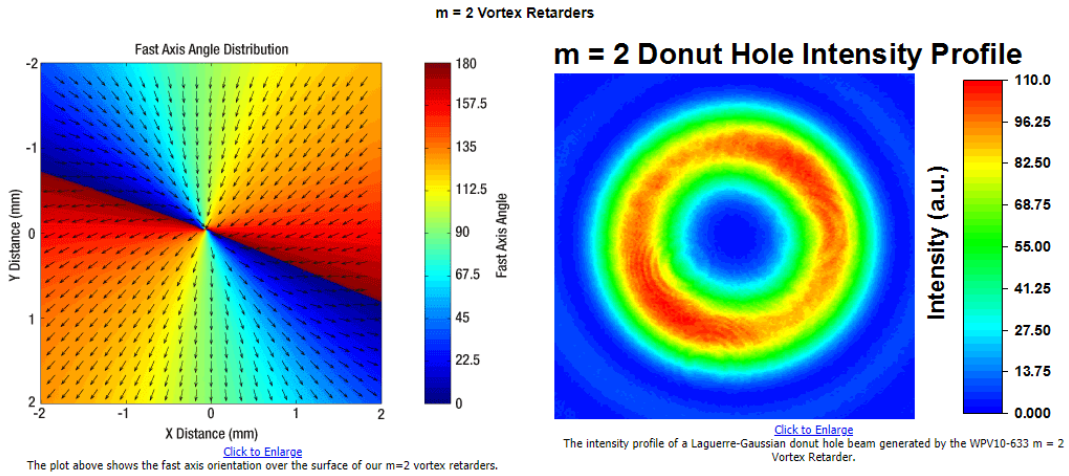

Figure 4.16: On the left is a plot of the fast axis orientation over the surface of the $m = 2$ vortex retarder. On the right side is the intensity distribution of a Gaussian beam, that passed through a Zero-Order Vortex Half-Wave plate: $m = 2$.

We then recorded the OAM spectrum of the signal photons. The resulting distribution is plotted in Fig. 4.17.

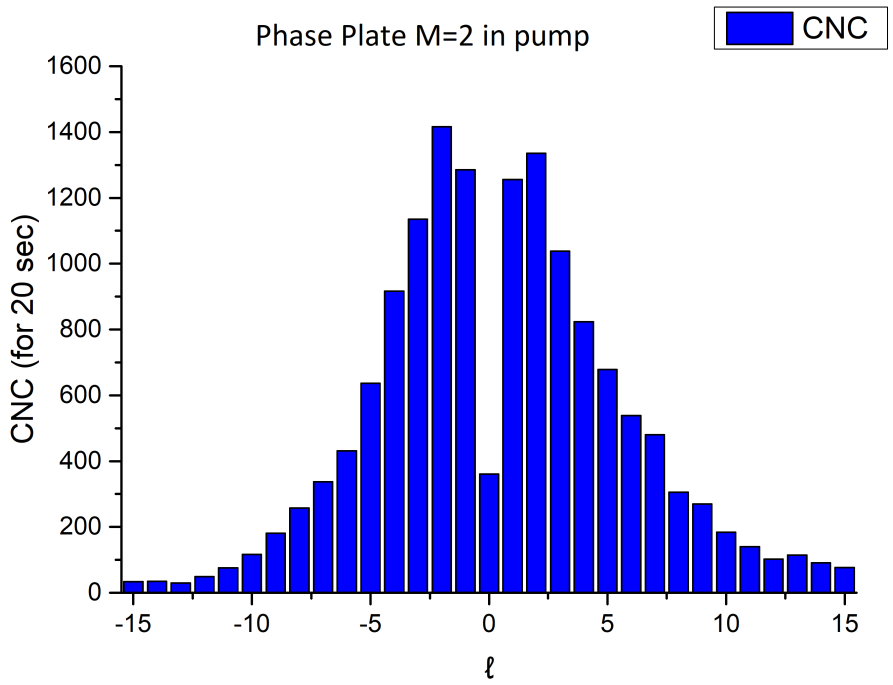

Figure 4.17: Measured OAM distribution of the signal photons after the SPDC process. The pump beam passed through a vortex retarder and possesses an OAM of $\ell = 2$.

As expected, the probability to find signal (or idler) photons in the mode $\ell = 0$ is smaller than for $\ell = \pm 1$. This OAM states is clearly not in a thermal state.
The purpose of this measurement is to show that it is possible to shape the OAM distribution of the down-converted signal and idler photons by changing the OAM of the pump beam. But the distribution doesn't show the exponential decay for $|\ell|$ and it is therefore not useful for our purpose of identifying it with a thermal state. To generate an OAM distribution in the signal and idler beams that still exhibits the exponential decay, and therefore can be interpreted as a thermal state, needs a more sophisticated superposition of OAM modes as a pump beam.

4.6.4 Superpositions of Thermal States

We have shown that a pump with zero OAM $\ell = 0$ generates a exponential OAM distribution for signal and idler beams, which we can use for the simulation of thermal states. We have also shown that different pump beam widths change the slope of that exponential decay and therefore the temperature of the simulated decay. In the next measurement we prepared the pump beam in a superposition of two Gaussian beams with zero OAM, with different beam widths. For that purpose we inserted a

Mach-Zehnder interferometer in the path of the pump beam laser before the non-linear crystal. The experimental setup is shown in Fig. 4.18. The pump laser is the same as before, a diode laser at $405\ \mathrm{nm}$. The linearly polarized pump beam is then coupled to the entrance of the interferometer, where it is separated into two parts with a half-waveplate (HWP) and a polarizing beam-splitter. In the upper arm of the interferometer we inserted a telescope. The telescope consists of two lenses with focal lengths $f_1 = 50\ \mathrm{mm}$ and $f_2 = 100\ \mathrm{mm}$. This doubles the beam width of the laser passing through the telescope compared to the laser in the other arm of the interferometer, where we have free propagation without a telescope. We then recombine the two beams with different beam waists at the exit of the interferometer. By rotating the HWP at the entrance of the interferometer we can change the proportions of the superposition of the two different modes. The recomined beam at the exit of the interferometer is then redirected onto the BBO crystal where the process of SPDC takes place. The subsequent setup is identical as in Fig. 3.1.
We then measure the OAM distribution of the idler beam in the same fashion as before.

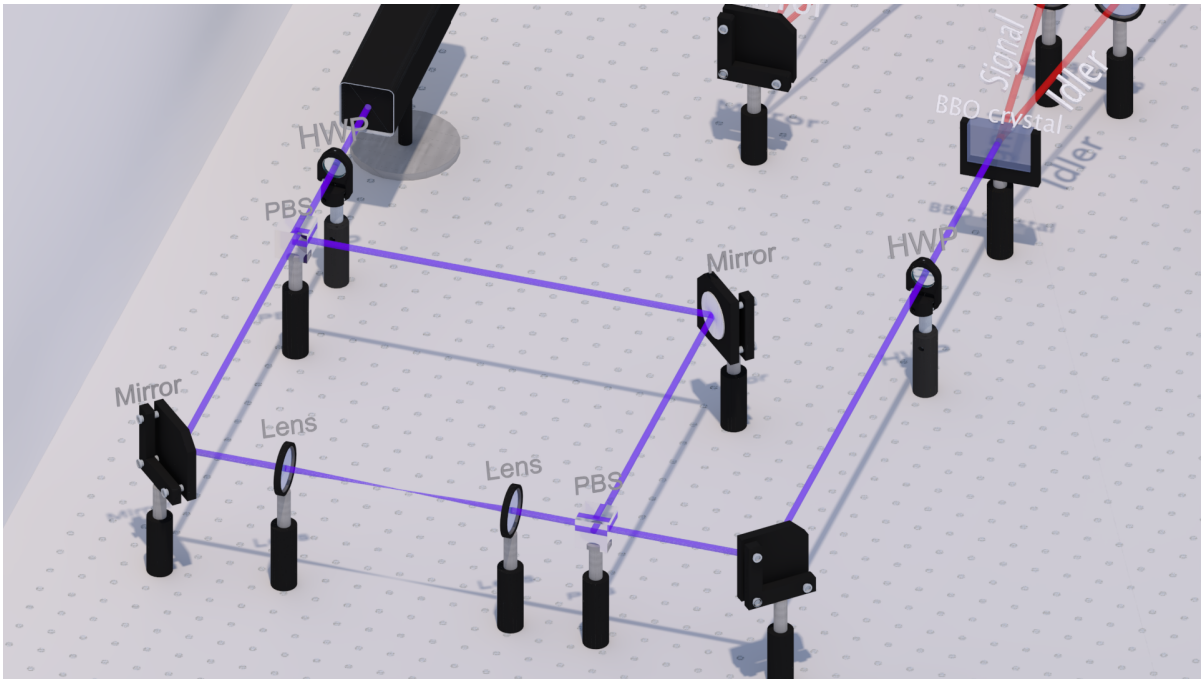

Figure 4.18: Experimental setup for the generation of superposition thermal states. After passing through a half-wave plate (HWP) the pump laser beam gets separated by a polarizing beam splitter (PBS) at the entrance of a balanced Mach-Zehnder interferometer. One of the beams passes through a telescope to increase the beam width before they are recombined in a second PBS. The two combined Gaussian beams pass through a second HWP to adjust their linear polarization to then pump the non-linear BBO crystal.

In a first measurement we blocked one arm of the interferometer to see the

OAM distributions that the two Gaussian beams generate separately. The result of the measurements is plotted in Fig. 4.19.

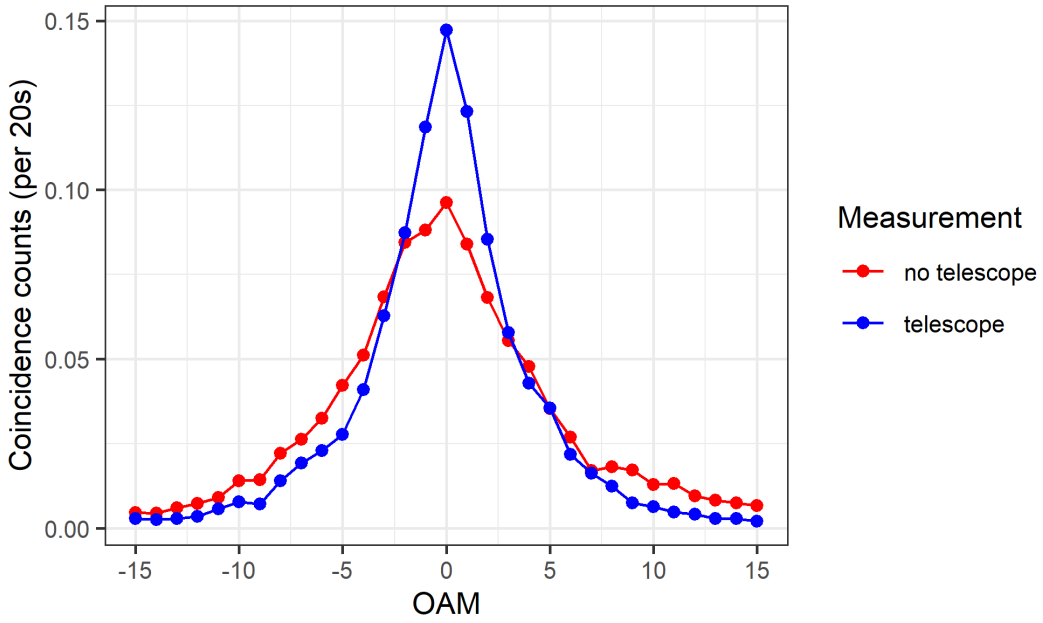

Figure 4.19: The pump beam was split in a Mach-Zehnder interferometer to generate two Gaussian beams with different beam waists. In each measurement one arm of the interferometer was blocked. Red dots are the laser beam as pump, blue dots are the laser after passing through a telescope.

We can see that the two pump beams with different beam waists produce two different thermal distributions with a distinct exponential slope, therefore with different inverse temperatures β. This was predicted by the overlap integral and was already demonstrated in a previous section of this chapter.
We then pump the non-linear crystal with the superposition of the two Gaussian beams. The results can be seen in fig. 4.20.

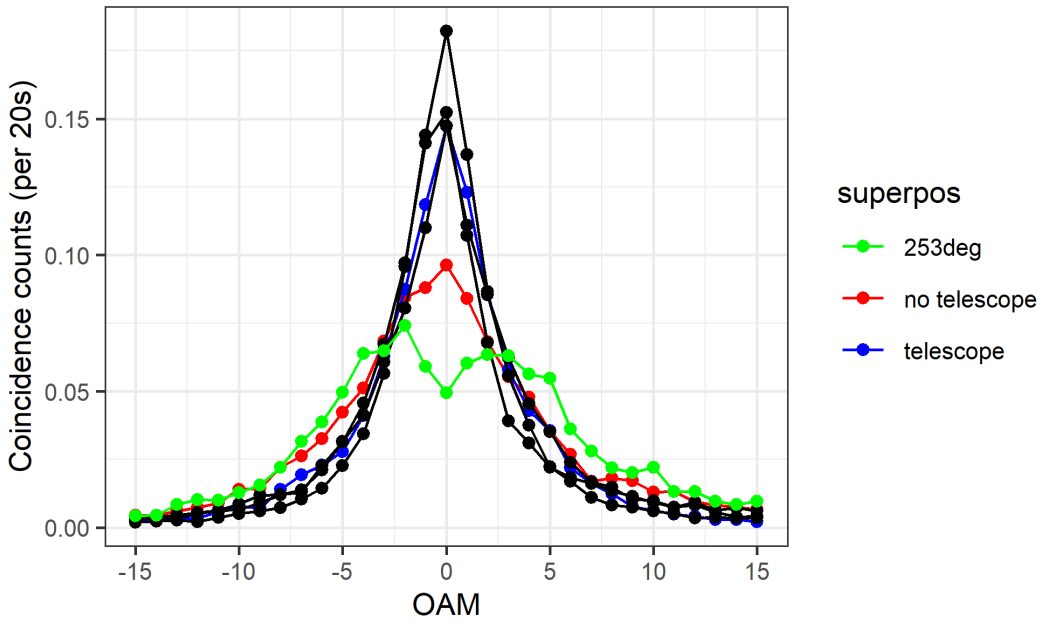

Figure 4.20: The pump beam is prepared in a superposition of Gaussian beams with different beam waists, using a Mach-Zehnder interferometer. The ratio of the superposition is determined by a HWP in front of the entrance of the interferometer. Red dots is the laser beam as pump, blue dots is the laser after passing through the telescope.

We measured the OAM distribution of the down-converted photons for different angles of the HWP at the entrance of the interferometer. The two measurements for the two arms of the interferometer without a superposition are shown for reference in red and blue. The measured OAM distributions for the superpositions are plotted in black. We expected the distributions to be *between* the blue and red distributions, as we prepared a mixture of the two for our pump beam. We highlighted one recorded distribution in green, which is also for superposition pump. This distribution seems completely out of equilibrium, but resembles the distribution generated by a pump beam containing OAM. This is caused by interference effects. When the pump beams with small and large beam waist interfere destructively they generate a ring-shaped intensity profile. This decreases the probability of generating modes close to $\ell = 0$ which have their peak intensity at the center.

Because the coherence length of the laser is longer than any path difference introduced by the Mach-Zehnder interferometer, the interference effects between the two recombined pump beams are non-negligible. A way to overcome this issue would be to use separate incoherent lasers. This would complicate the alignment of both pump beams to the subsequent setup on the other hand.

5. Applications

So far we have shown how to remotely prepare and how to modify a single photon thermal state. This lays the foundation for using thermal states for thermodynamic investigations of quantum systems. In this chapter we want to show the utility of such thermal states by presenting some applications of our simulated remotely prepared thermal states, to the field of thermodynamics.

5.1 Entropy

One application of thermal states is the investigation of the entropy of a system when a processes is acting on it. The results derived in this section are valid for the classical as well as for the quantum context. In the following we denote the density matrix of a (quantum) system with ρ.
If our system is in a thermal state, which is a completely mixed state, the density matrix has only diagonal elements that are non-zero in the energy eigenbasis. In this case the density matrix ρ can therefore be seen as a classical probability distribution function, where the diagonal elements are the probabilities of the system corresponding to a certain energy level. The matrix ρ is positive and satisfies Tr$\rho = 1$. We can then define the entropy of the system as

$$S(\rho) = -\mathrm{Tr}\rho \ln \rho \; . \tag{5.1}$$

In this definition we chose the natural logarithm, but in information theory for example the logarithm with base 2 is chosen, as we deal with bits of information. We can go on and define the so-called relative entropy

$$S(\rho|\rho') = \mathrm{Tr}(\rho(\ln \rho - \ln \rho')) \; , \tag{5.2}$$

where ρ and ρ' are the density matrices of two different states. The relative entropy is strictly positive

$$S(\rho|\rho') \geq 0 \; , \tag{5.3}$$

and zero only in the case of $\rho = \rho'$. This quantity of the relative entropy can be used as a measure of the distance between two density matrices or probability distributions. As a matter of fact, this is the same expression we stated earlier as the Kullback-Leibler divergence. If we take the state ρ' to be a thermal state $\rho' = \rho_\beta$ with

$$\rho_\beta = \frac{\mathrm{e}^{-\beta \mathrm{H}}}{Z(\rho_\beta)} \, , \tag{5.4}$$

where H is a given function or operator, usually the Hamiltonian of the system and Z is the partition function. We can then write the relative entropy as

$$S(\rho|\rho_\beta) = S(\rho_\beta) - S(\rho) + \beta \mathrm{Tr}((\rho - \rho_\beta)\mathrm{H}) \, , \tag{5.5}$$

By using the definition of the free energy of the state ρ

$$F(\rho, H) = \mathrm{Tr}(\rho \mathrm{H}) - \frac{1}{\beta}\mathrm{S}(\rho) \, , \tag{5.6}$$

we can also write the relative entropy in means of the free energy

$$S(\rho|\rho_\beta) = \beta(F(\rho, H) - F(\rho_\beta, H)) \, . \tag{5.7}$$

5.1.1 Entropy production for two interacting systems

We can now extend this formalism to the case of two systems interacting. For two subsystems $\rho_A = \mathrm{Tr_B}\rho$ and $\rho_B = \mathrm{Tr_A}\rho$, we can write the energy of the total system ρ as:

$$E(\rho) = \mathrm{Tr}(\rho \mathrm{H}) = \mathrm{E_A}(\rho) + \mathrm{E_B}(\rho) \tag{5.8}$$

Assuming that the initial system is in a product state

$$\rho_0 = \rho_{A,0} \otimes \rho_{B,0} \, . \tag{5.9}$$

In this case, the relative entropy $S(\rho|\rho_A \otimes \rho_B)$ is the same as the mutual information between the two distributions associated with the subsystems A and B. This amount of information can as well be seen as the information coming from the fact that the two systems are interacting. The relative entropy equals zero in the case of $\rho = \rho_A \otimes \rho_B$, which means the mutual information is zero and the two sub-systems are completely separable.

The total system can now evolve under the transformation U that preserves entropy and energy, for example a unitary evolution or process acting on the combined total system. We interpret this process as the interaction of the two subsystems. With the hypothesis that the variation of the total energy after the interaction is

$$\Delta^{(U)}E(\rho) = E(\rho(t)) - E(\rho_0) = 0 \,, \tag{5.10}$$

Here, ρ_0 is the initial state of the system and $\rho(t)$ is the system at an arbitrary time t after the process has occurred. In the same manner we will use the symbol $\Delta^{(U)}$ to express the difference of an entity before and after the process U has acted. We can use the conservation of the total entropy to derive the identity

$$\begin{aligned} \Delta^{(U)}S(\rho_A) + \Delta^{(U)}S(\rho_B) &= S(\rho_A(t)) + S(\rho_B(t)) - S(\rho_0) && (5.11)\\ &= S(\rho_A(t) + S(\rho_B(t)) - S(\rho(t)) && (5.12)\\ &= S(\rho(t)|\rho_A(t) \otimes \rho_B(t)) \,. && (5.13) \end{aligned}$$

This is true as we have $-\mathrm{Tr}(\rho(\mathrm{t}) \ln \rho_{\mathrm{A}}(\mathrm{t})) = -\mathrm{Tr}(\rho_{\mathrm{A}}(\mathrm{t}) \ln \rho_{\mathrm{A}}(\mathrm{t}))$, and we want to mention that the well-known identity

$$S(\rho(t)) \leq S(\rho_A(t)) + S(\rho_B(t)) \tag{5.14}$$

is valid as a special case of the inequality for any state ρ

$$S(\rho) \leq S(\rho_A) + S(\rho_B) \,. \tag{5.15}$$

Now we want to look at the result we obtained so far for the case of one of the subsystems to be initially in a thermal state. Lets say

$$\rho_{A,0} = \frac{\mathrm{e}^{-\beta_{\mathrm{A}}\mathrm{H}}}{Z_A(\beta_A)} \,. \tag{5.16}$$

We then get

$$\Delta^{(U)}S(\rho_A) - \beta_A \Delta^{(U)}E_A(\rho_A) = -S(\rho_A(t)|\rho_{A,0}) \,. \tag{5.17}$$

And as a result of this we have

$$\Delta^{(U)}S(\rho_A) - \beta_A \Delta^{(U)}E_A(\rho_A) \leq 0 \,. \tag{5.18}$$

These two equations do not require the process U to be an unitary evolution that conserves entropy or conserves energy, but it is required that the Hamiltonian H of the system be time-independent [92]. From Eq. (5.18) we can estimate the maximum change in entropy that can occur for a specific energy change of a thermal state that was initially at the inverse temperature β_A. With Eq. (5.17) we can calculate the change in entropy of the system A caused by the process U, if we know the change in energy of the subsystem A and the relative entropy between the initial thermal state and the final state of the system A after the process has occurred.
In our experimental scheme we showed how to prepare initially thermal states and we are able to measure the populations of each energy level. With those measurements we can calculate the energy of the system. As we are dealing with thermal states, which are completely mixed states and diagonal in the energy eigen-basis, we readily have the density matrix of the system only by measuring the energy probability distribution of our state. This is true assuming we didn't introduce coherences due to the interaction of the subsystems during the evolution U. So, in our experimental simulation, we can prepare a thermal state, apply a process and measure the energy probability distribution. We can therefore determine the energy, the entropy and the relative entropy between the states before and after the process occured. We are then able to use Eq. (5.17) to calculate the entropy production of the system A for a given process U.
If the process U conserves energy or entropy of the total system these results can be extended to the subsystem B.
As an example, suppose U conserves entropy and we couple the system B, initially in an arbitray state to system A initially in a thermal state, then we can find the inequality

$$\Delta^{(U)} E_A(\rho) \geq \frac{1}{\beta_A} |\Delta^{(U)} S(\rho_B)| \, . \tag{5.19}$$

If we wanted to lower the entropy of system B, then we know the energy of system A must be increased by at least the amount defined by the previous expression. Or if we measure the change in energy of the subsystem A after the process acted, we can calculate the maximum entropy change of subsystem B.

5.1.2 Example for Turbulence Mask

We can now apply those theoretical results to our experimental data. Let's look at the example of the turbulence mask applied to an initial thermal state shown in chapter 4.5.2. The temperature for the initial thermal state is $\beta = 0.34$ and after

the thermal state passed through the turbulence the temperature is $\beta = 0.28$. The average energy for the initial state is $\langle E \rangle = 3.56\ \hbar\omega$ and after the turbulence was applied the average energy is $\langle E \rangle = 4.19\ \hbar\omega$. We can then calculate the relative entropy between the two probability distributions, before $[p(\ell_i)]$ and after $[p(\ell_f)]$ the turbulence was acting.

$$S\left(p(\ell_i)|p(\ell_j)\right) = \sum_{\ell} p(\ell_i) \log \frac{p(\ell_i)}{p(\ell_f)} = 0.030\ . \tag{5.20}$$

If we use Eq. (5.18) we can already estimate the maximum entropy change of our system ρ caused by the turbulence, by only looking at the energy difference of the initial and final state.

$$\Delta^{(U)} S(\rho) \leq \beta \Delta^{(U)} E(\rho) = 0.34 * (4.19 - 3.56) = 0.214\ . \tag{5.21}$$

This tells us that the maximum entropy difference introduced by the applied turbulence is 0.214. As we have readily the probability distribution from the projective energy measurement we can directly calculate the actual entropy change in our initially in a thermal state prepared system ρ by using Eq. (5.17). We get

$$\Delta^{(U)} S(\rho) = \beta \Delta^{(U)} E(\rho) - S\left(p(\ell_f)|p(\ell_i)\right) = 0.34 * (4.19 - 3.56) - 0.03 = 0.184\ . \tag{5.22}$$

Therefore, the process of turbulence changed the entropy of the system by the amount 0.184.

We could just as well interpret the SLM that applied the turbulence as a subsystem ρ_B of a global system ρ and our thermal state as a subsystem ρ_A. The action of the phase mask projected on the SLM can then be seen as the two subsytems interacting or coupling. Then with eq. (5.19) we can determine an upper boundary for the maximum entropy change introduced by the coupling to our thermal state. We have

$$\Delta^{(U)} S(\rho_B) \leq \beta \Delta^{(U)} E(\rho_A) = 0.34 * (4.19 - 3.56) = 0.214\ . \tag{5.23}$$

This means by coupling the two systems ρ_A and ρ_B, the maximum entropy change for subsystem B is 0.214 .

5.1.3 Extension to Work

We can now extend this formalism to a thermal state interacting with an external work source, instead of two systems interacting. The amount of work a

external observer must then perform to change the state of the system is equivalent to the change of the energy of the system (if no energy is lost in the interaction). This motivates the definition of the two-measurement protocol. This protocol defines the work performed by a process as the difference between an initial energy measurement and a measurement after the process has taken place. In the notation established in the previous section we can write

$$W = -\Delta^{(U)} E(\rho) \ . \tag{5.24}$$

The macroscopic second law of thermodynamics says that for a system in contact with a heat bath, the required amount of work W to change the state of a system between two different equilibrium states, is at least equal to the corresponding increase in equilibrium free energy ΔF^{eq}:

$$W - \Delta F^{eq} \geq 0 \ . \tag{5.25}$$

With that inequality we can already establish an upper bound for the possible extractable work. The free energy of a non-equilibrium state is higher than that of the corresponding equilibrium state. That corresponding equilibirum state is the out-of-equilibrium state after it was allowed to thermalize. The difference of the free energy is an amount equal to the temperature times the information I needed to specify the non-equilibrium state. We can express that information differences with the relative entropy, as it is common in information theory and get

$$\beta_0 \Delta F^{eq} = \beta_0 \left(F^{(U)} - F^{eq} \right) = S(\rho^{(U)} | \rho_{\beta_0}) \geq 0 \ . \tag{5.26}$$

Applying this to our experimental scheme, we can therefore by measuring the energy of the system before and after a process was applied, calculate the work performed by the process directly through the 2-measurement protocol. This is valid for reversible processes. For irreversible processes however, for example if the process U is a heat exchange rather then an external agent performing work on the system, we can then, by calculating the relative entropy, calculate the change in free equilibrium energy and determine an upper bound for the maximum extractable work.
This way of expressing a boundary for work, in terms of the free energy can then be used to derive the Jarzynski fluctuation theorem.

5.2 Jarzynski fluctuation theorem

We want to use our experimental platform to study the field of quantum thermodynamics. In thermodynamics at the quantum level, fluctuations become crucial and have to be taken into consideration. Therefore quantum thermodynamics are concerned with small systems in the non-equilibrium regime for short time scales. As we have shown in the previous chapter, the process of turbulence simulates such a type of random fluctuations that still leaves our thermal system in thermal equilibrium. The generation of our thermal states as well as the process of turbulence is completely determined by its statistical nature. With our experimental platform, though, we have access to every single energy level of our system and can as well control all parameters of the simulated fluctuation through the turbulence mask. This gives us the possibility to use our setup to study quantum thermodynamics.

5.2.1 Work probability distribution

We know from thermodynamics, that when a reversible process drives a system from a initial state to a final state, then the work W is performed, with $W = -\Delta F$ (isothermal process). But if the process is irreversible, the performed work is in general different from the free energy difference. This is because there are many possible irreversible processes connecting an initial state to a final state (but only one isothermal reversible) and each process having a different amount of performed work. This is exactly the reason we have the inequality instead of equality in Eq. (5.25), and in general for irreversible processes we have

$$W = \Delta E + W_l \, , \tag{5.27}$$

where W_l is some lost work, depending on the process. Therefore, if we want to think of all possible processes connecting an initial to a final state, we have to think in averages

$$\langle W \rangle \geq \Delta F \, , \tag{5.28}$$

where the left-hand-side is the average of the work for all possible processes that drive the initial to the final state. Now, without knowing the specific motions of the microscopic degrees of freedom that constitute the system, and determine the work performed by each different process connecting the initial state to the final state, we

can only determine a work probability distribution $P(W)$ for all processes.
Specifically, for our quantum system we can use the same simulation of thermal states as shown before. This means we prepare a thermal state in the OAM degree of freedom through the process of SPDC. We then apply a process to our initial prepared state. In the measurements shown in this chapter we use the process of atmospheric turbulence how it was explained in chapter 4.5. The turbulence mask couples the OAM input modes to output modes based on the Kolmogorov statistics shown in the same chapter. We can then define the work performed by the process on the system by comparing the input state with the final output state. As the eigenenergies of our simulated system are $\varepsilon_\ell = (|\ell| + 1)\hbar\omega$, a projection on the OAM eigenbasis is equivalent to a projection on the energy eigenbasis of the simulated system (see chap. 2.4).
There are different definitions about what work actually is in the quantum context, but a widely accepted definition is work as the difference between two energy measurements. One measurement before the process acted on the system and one after; the 2-measurement protocol mentioned in the previous section. The work therefore only depends on the energy change and in our simulated system only on the change of $|\ell|$. We can define the work as

$$W_{\ell\ell'} = (|\ell'| - |\ell|)\hbar\omega \ . \tag{5.29}$$

This is the work that was performed by the process on a photon initially in the mode associated with ℓ and then ended up in the final state ℓ' after a process has acted.
Using this definition for work, we can go on to write the work probability distribution. This function $P(W)$ gives the probability that the process performed the work W on the system. We can write it as

$$P(W) = \sum_{\ell,\ell'} p_{\ell\ell'} \ \delta(W - W_{\ell\ell'}) \ , \tag{5.30}$$

where $p_{\ell\ell'}$ is the probability of observing the transition $\ell \to \ell'$. This probability is given by

$$p_{\ell\ell'} = p_\ell \ p_{\ell'|\ell} \ , \tag{5.31}$$

where p_ℓ is the probability of the first projective measurement obtaining the OAM ℓ, and $p_{\ell'|\ell}$ is the conditional probability of ending up with OAM ℓ' given that the system was initially with OAM ℓ.
In our case these probabilities p_ℓ are given by the populations of the density matrix of

the thermal state represented in the energy eigenbasis.

$$p_\ell = \frac{\mathrm{e}^{-\beta(|\ell|+1)\hbar\omega}}{Z} \ . \tag{5.32}$$

The probabilities $p_{\ell'|\ell}$ is what we actually measure in the experiment. We measure the OAM distribution for a given initial OAM mode.

5.2.2 Jarzynski's theorem

In the thermodynamic regime where fluctuations are important and quantities like work become stochastic, the usual laws of thermodynamics don't hold. However when we take such fluctuations correctly into consideration, stronger laws can be found in the form of fluctuation relations such as the Crook's theorem [93] or the Jarzynski equality [26]. The latter writes:

$$\langle \mathrm{e}^{-\beta \mathrm{W}} \rangle = \mathrm{e}^{-\beta \Delta \mathrm{F}} \tag{5.33}$$

$$= \int dW \ P(W) \mathrm{e}^{-\beta \mathrm{W}} \ . \tag{5.34}$$

ΔF is the free energy difference between the final and initial states. The usual form of the second law of thermodynamics in Eq. (5.28) follows from the convexity of the exponential function. This fluctuation relation is of statistical nature of the second law. It must hold only on average and not on every single realization of a process. The relation expressed in this form holds for all processes that are unital and therefore preserve the identity. Later this result was extended to all processes described by completely positive and trace-preserving maps [94]

$$\langle \mathrm{e}^{\beta \mathrm{W}} \rangle = \mathrm{e}^{-\beta \Delta \mathrm{F}} (1 + \delta) \ , \tag{5.35}$$

where $\delta = \mathrm{Tr}[\rho_\beta G_\Phi]$, with $G_\Phi = \Phi(\rho\ *) - \rho^*$ (ρ^* is the maximally mixed state) being a measure of how much the dynamical map Φ deviates from a unital one. For unital maps, $\Phi(\rho^*) = \rho^*$, thus implying $\delta = 0$. Again we get the modified second law of thermodynamics:

$$\langle W \rangle - \Delta F \geq -\beta^{-1} \ln(1 + \delta) \ . \tag{5.36}$$

A special case of this equation is when, for example an external perturbation is turned on, acts on the system and is then turned off. In this case we have $\Delta F = 0$ and we get

$$\langle \mathrm{e}^{-\beta \mathrm{W}} \rangle = \int \mathrm{dW}\ \mathrm{P(W)} \mathrm{e}^{-\beta \mathrm{W}} = 1\ .$$

This is the case for the process of atmospheric turbulence we will investigate here.

5.2.3 Experimental setup

The experimental setup is in principle the same as in Fig. 3.1. While we were performing the measurements on the setup we became aware that the group of Prof. Forbes was performing the same kind of measurements. In a collaboration of our two laboratories we published the results together [25], and decided to use the data recorded in the laboratory of Prof. Forbes. For this reason the setup that was used is shown in Fig. 5.1. In this setup a $355\ \mathrm{nm}$ mode-locked laser pumped a type-I BBO

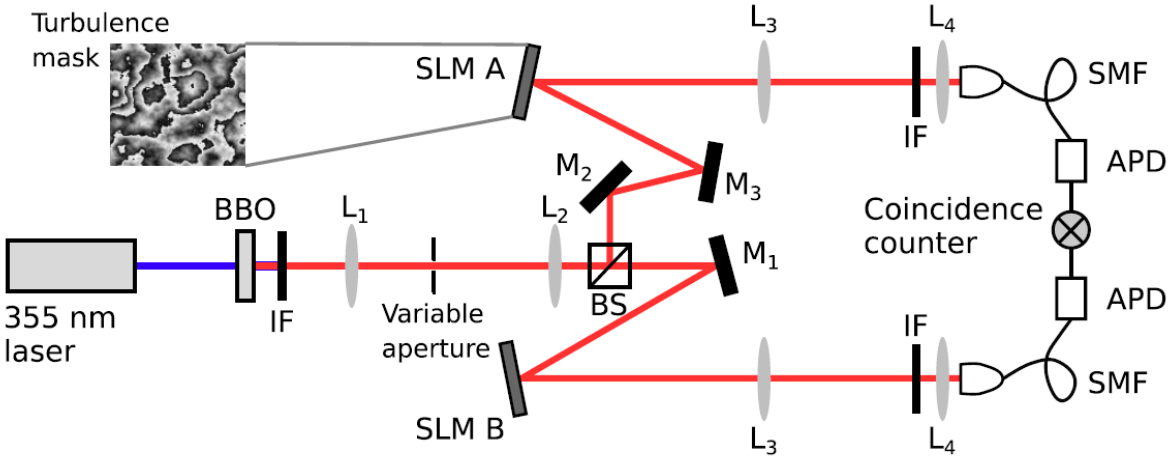

Figure 5.1: Experimental setup: A BBO-crystal is pumped with a $355\ nm$ laser. The generated signal and idler beams are separated by a beam splitter and imaged onto two separate SLM. The SLMs and single-mode optical fibers are used to measure the OAM of the signal and idler photons. At the output of the fiber, they are detected by single-photon counting modules and coincidences are recorded. Image taken from Ref. [25].

crystal, generating the signal and idler photon pairs in the SPDC process. The twin photons are emitted in the same direction in the colinear setup and seperated with a beam splitter. Each photon was passed through a $4f$ telescope. Lenses L_1 and L_2 have $200\ \mathrm{mm}$ and $400\ \mathrm{mm}$ focal length respectively. This telescope images the crystal plane onto the two separate SLMs. The SLM plane was then imaged on the entrance

of the single-mode optical fibers with lenses L_3 and L_4 (with focal lengths $f_3 = 500\ \mathrm{mm}$ and $f_4 = 2\ \mathrm{mm}$). The output of the single-mode fibers was detected by avalanche photodiodes and connected to a coincidence counting module. To measure the OAM of the signal and idler photons we project forked hologram masks on SLM A and SLM B. In two separate measurements we want to simulate atmospheric turbulence in one (signal beam) side and in both sides (signal and idler beam). For that end we can project a superposition of the forked holograms together with the turbulence masks onto the SLMs. Like this we can use a single SLM to simulate the turbulence process and utilize it to measure the OAM of the signal beam. The coincidence counts were measured with $10\ \mathrm{s}$ sampling times and a coincidence window of $12\ \mathrm{ns}$. In order to measure the conditional transition probabilities necessary for the calculation of the Jarzynski equality we have to measure the OAM of signal and idler photons at the same time. By measuring the OAM of the idler photon we remotely prepare the OAM of the signal photon as explained in the previous section. The signal photon is therefore prepared with the OAM ℓ and then subjected to the turbulence process which couples to different OAM modes. The OAM spectrum (all possible values ℓ') of the signal photons are measured. This results in a coincidence matrix. On the vertical axis are the initial, remotely prepared OAM modes ℓ and on the horizontal axis are the final OAM modes ℓ'. Each row of the matrix is a complete OAM distribution measurement for a prepared initial OAM of ℓ.

Those recorded coincidence matrices are shown in Fig. 5.2. The left column are the measurements where only SLM A was applying the turbulence process, the right column is for the case where both SLMs where used to simulate atmospheric turbulence.

5.2.4 Results

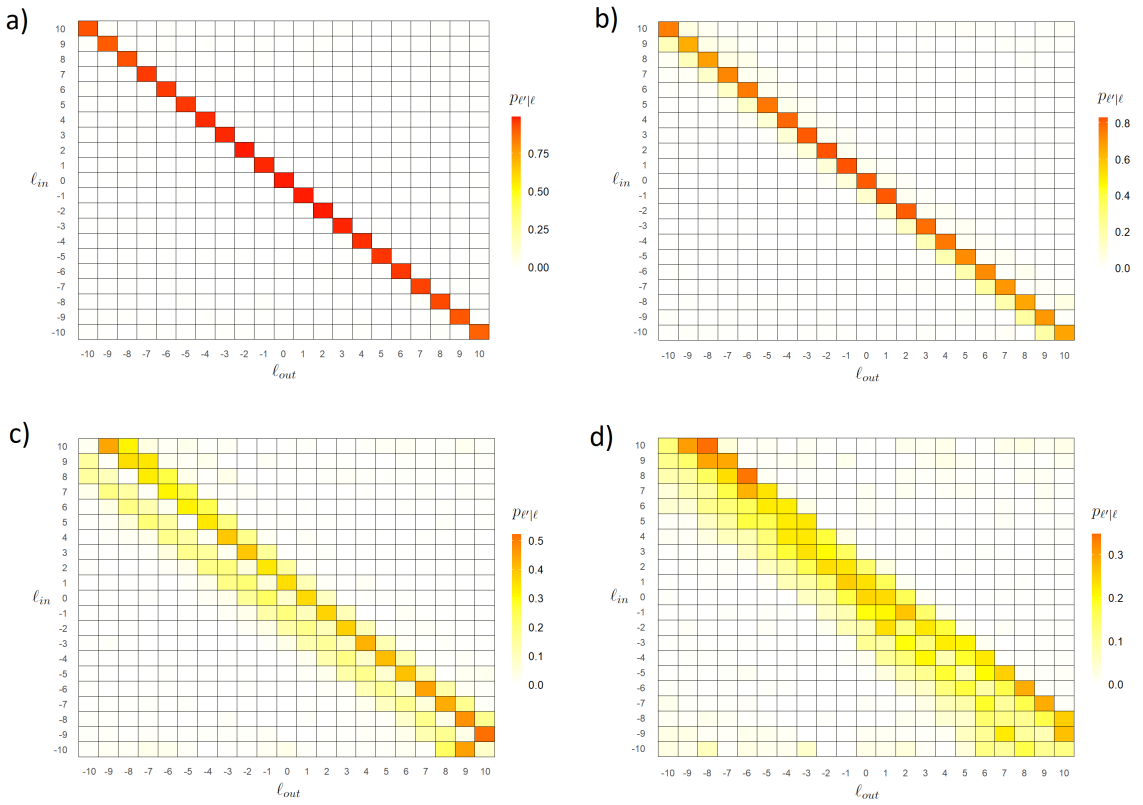

Figure 5.2: Measured and normalized conditional transition probabilities $p_{\ell'|\ell}$. Coincidence counts have been recorded for simultaneous measurements of modes with azimuthal index ℓ_{in} in the signal beam and ℓ_{out} in the idler beam. a) No turbulence was applied. b), c) and d) A turbulence mask with increasing scintillation strength has been applied to the idler photons before their OAM was measured.

The measurement results of the conditional transition probabilities $p_{\ell'|\ell}$ are shown in Fig. 5.2. The OAM was measured for the signal and for the idler photons simultaneously. The OAM measurement of the idler photons remotely prepares the OAM of the signal photons. The signal photons have then been directed onto a SLM screen, subjecting them to an atmospheric turbulence mask. Coincidence events have been post-selected and counted. In each matrix, each line, representing the remote preparation of a single OAM per photon (ℓ_{in}), has been normalized in order to compensate for losses in the experimental apparatus. The measurements shown in tile a) are for a blank SLM screen and therefore no turbulence. From the results with no turbulence we can see almost perfect correlation, showing that the remote state preparation is working as intended. This measurement can also be seen as

a calibration and as an experimental proof that the free energy does indeed not change. We can see that a state prepared in ℓ_{in} is projected onto the final state ℓ_{out} and without turbulence we have $\ell_{in} = \ell_{out}$. We can then prepare the same states again, but this time subject the states to a simulated atmospheric turbulence. With increasing scintillation strengths [b)→c)→d)] for the turbulence masks, we notice a loss of correlation, because the atmospheric turbulence masks couple the input modes ℓ_{in} to different output modes which can be different from the initial state.

Instead of directly using the thermal probabilities for each mode determined by the SPDC process we can calculate the Jarzynski quantity $\langle \mathrm{e}^{-\beta \mathrm{W}} \rangle$ for different inverse temperatures β by only using the transition probabilities. To do so we can use the measured transition probabilities $p_{\ell'|\ell}$ from Fig. 5.2 and calculate the probabilities p_ℓ like in Eq. (5.31) by multiplying the transition probabilities with the calculated thermal coefficients p_ℓ for different temperatures β. We then go on to calculate the work probability distribution in Eq. (5.30). The averages over those work probability distributions are then calculated to determine the Jarzynski equation for different temperatures. The result is shown in Fig. 5.3. On the vertical axis is the Jarzysnki quantity $\langle \mathrm{e}^{-\beta \mathrm{W}} \rangle$ and on the horizontal axis are the different inverse temperatures β.

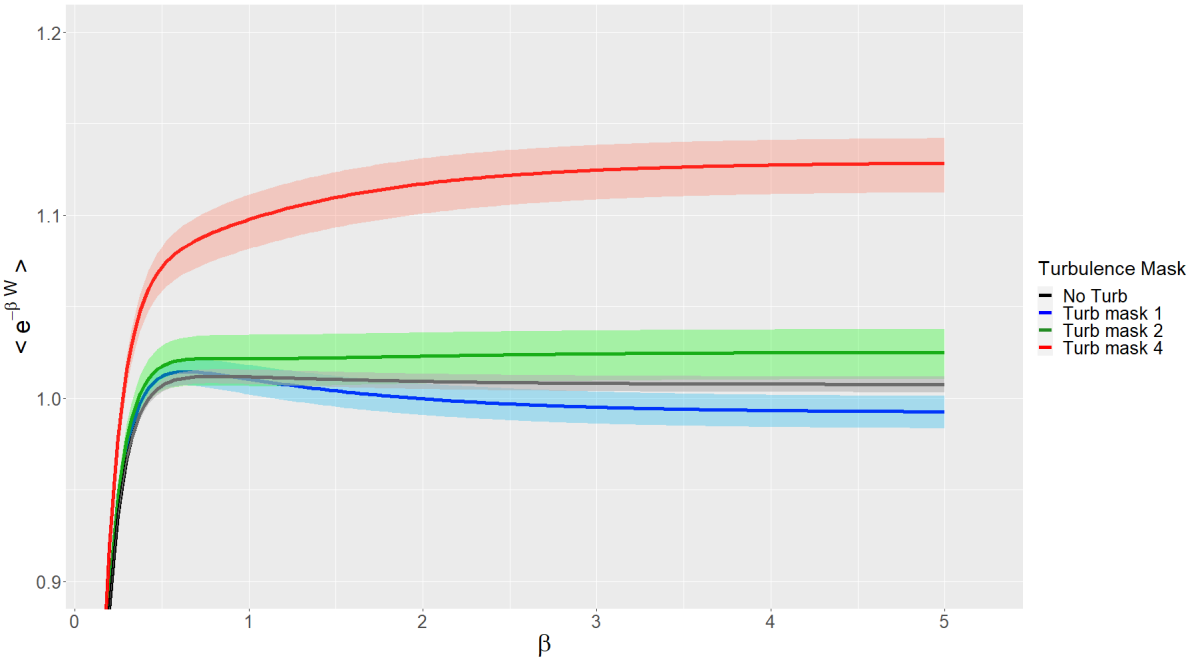

Figure 5.3: Plot of the Jarzynski equation $\langle \mathrm{e}^{-\beta W} \rangle$ as a function of β. The conditional transition probabilities have been used to calculate the work probability distribution and to finally determine the Jarzynski quantity. The shaded areas around the plotted lines are the measurement uncertainties.

From Eq. (5.37) we predicted that the Jarzynski equation equals one for the process of atmospheric turbulence. But for higher turbulence strengths, the quantity $\langle \mathrm{e}^{-\beta \mathrm{W}} \rangle$ deviates from one. The shaded areas around the plotted lines are representing the measurement uncertainties within the 95% confidence interval. This error has been calculated by propagating the uncertainty in the coincidence counting rate through Monte Carlo processing.

Instead of only calculating the Jarzynski equation we can compare it with the generalized version defined in Eq. (5.35). Again, for the turbulent process that is *turned off* after its action, we have $\Delta F = 0$. We can then check the validity of the theorem by calculating the following expression for different values of β:

$$\langle \mathrm{e}^{-\beta W} \rangle - (1 - \delta) = 0 \, . \tag{5.37}$$

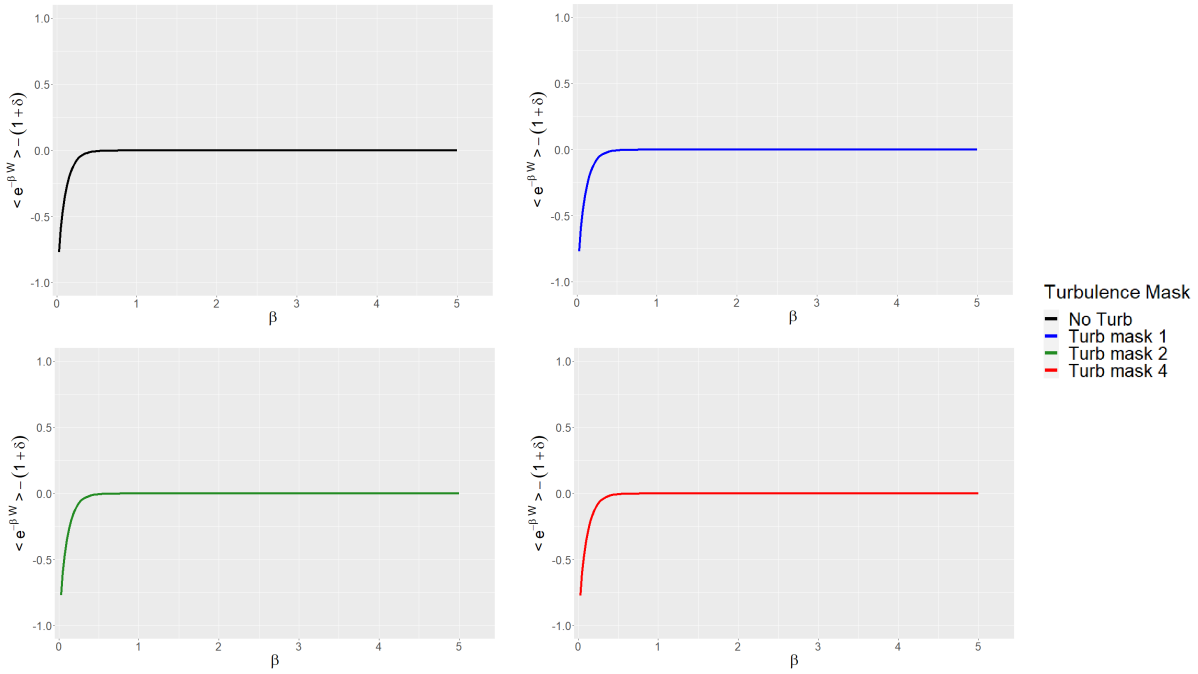

Figure 5.4: Plot of the deviation of the Jarzynski equation $\langle \mathrm{e}^{-\beta W} \rangle$ ad the generalized Jarzysnki relation for any completely positive and trace-preserving map. For all three turbulence masks with different scintillation strengths as well as when no turbulence was present, the deviation from the Jarzynski relation is nearly perfect zero.

In Fig. 5.4 are the plots of this deviation for the different turbulence masks. They are plotted in different graphs as their overlap was too great. We see all four plots are almost perfect zero. Therefore the generalized Jarzynski fluctuation relation is respected for all turbulence masks. This leads to the conclusion that the turbulence

process acts as a slightly non-unital process as we got $\langle \mathrm{e}^{-\beta W} \rangle$ different from 1, while still obeying the generalized relation for completely positive and trace-preserving maps.
In the region of very small values of β the plots for the Jarzynski equation and the gerneralized version show results different from 1 and 0, respectfully. Technically our system is of infinite dimension, but in our experimental scheme the system is truncated in $|\ell| \leq 10$. As larger energy levels have a greater contribution to thermal states with inverse temperatures especially below 2, those truncation effects are stronger in that region and may introduce nonphysical features. For temperatures $\beta \geq 2$ the contributions of $|\ell| \geq 10$ are small enough to be negligible.

6. Conclusions and Outlook

In this work, we presented the complete experimental platform on how to remotely prepare single-photon thermal states, how to use this approach for investigations of thermodynamic processes acting on a system and for quantum thermodyanmics. The simulation scheme based on the analogy between the paraxial Helmholtz equation and the Schrödinger equation allows us to emulate quantum systems through light beams in LG modes. Their OAM degree of freedom is used to simulate the energy levels of the quantum system. We have shown the possibilities in remotely generating single photon thermal states, by using the process of spontaneous parametric down-conversion and the entanglement in the orbital angular momentum degree of freedom. We showed that we can prepare photon states with exponentially decaying statistics, which can be fine-tuned into thermal distributions. By changing parameters such as the pump laser size, detection aperture size in the non-local process or the mode beam widths we were able to adjust the slope of the exponential decay and therefore the *temperature* of these distributions, which we interpret as thermal states in our analogy. Submitting those prepared states to the process of turbulence and analyzing the output, we could show that turbulence performs work on the system and drives it out of equilibrium. This is a first demonstration of how to apply our experimental scheme to the study of thermodynamics. One of the great advantage of this experimental scheme for simulation is its robustness. The light beams are propagated mostly in free space and no advanced stabilization against vibrations was needed. Also, it was not necessary to thermally stabilize the setup or even single components as all processes are robust against small temperature changes. This optical setup using the propagation of LG beams for simulation is also less complex and can be implemented by very few and rather inexpensive elements compared to schemes involving for example trapped ions and experiments involving spin. Again, resulting in a more stable experimental setup. Nevertheless we maintain a high degree of control over the experimental parameters necessary for a precise simulation of thermal states.

With this work, we took one step forward in the direction of further experimental investigations of quantum thermodynamics by using an optical setup and beam

propagation. The growing interest in beams containing OAM also motivates a further investigation with experimental setups using for example LG beams. Possible ideas continuing this line of research is the investigation of the effect of thermalization, and how to use our optical system to get further insights into this field of quantum thermodynamics. Another area of interest are thermal machines and closed thermodynamic cycles. This could be possible with our approach in the future by cascading thermodynamic processes using SLMs. There are a several quantum effects that include thermal states that could be verified in the laboratory with an experimental setup like the one presented in this work.

A. Overlap Integral

The probabilities of finding two down-converted twin photons in the LG modes characterized by the indices ℓ_i and p_i is

$$P_{p_s,p_i}^{\ell_s,\ell_i} = \left| C_{p_s,p_i}^{\ell_s,\ell_i} \right|^2 \ . \tag{A.1}$$

The coincidence amplitudes are determined by the spatial overlap integral mentioned in Eq. (3.15) [78]

$$\begin{aligned} C_{p_s,p_i}^{\ell_s,\ell_i} &= \langle \psi_i, \psi_s | \psi_{SPDC} \rangle \\ &\propto \int_0^{2\pi} d\phi \int_0^{\infty} r \ dr \ LG_{p_p}^{\ell_p} \left(LG_{p_s}^{\ell_s} \right)^* \left(LG_{p_i}^{\ell_i} \right)^* \ . \end{aligned} \tag{A.2}$$

This integral determines the nonlinear coupling between the pump mode (ℓ_p, p_p) and the signal (ℓ_s, p_s) and idler (ℓ_i, p_i) modes. Inserting the mode function for the LG beams yields:

$$\begin{aligned} \mathcal{O}_{p_p,p_s,p_i}^{\ell_p,\ell_s,\ell_i} = & \frac{c_{p_p,\ell_p} c_{p_s,\ell_s} c_{p_i,\ell_i}}{\omega_p \omega_s \omega_i} \int_0^{\infty} r \ dr \frac{(\sqrt{2}r)^{|\ell_p|+|\ell_s|+|\ell_i|}}{\omega_p^{|\ell_p|} \omega_s^{|\ell_s|} \omega_i^{|\ell_i|}} \\ & \times L_{p_p}^{|\ell_p|} \left(\frac{2r^2}{\omega_p^2} \right) L_{p_s}^{|\ell_s|} \left(\frac{2r^2}{\omega_s^2} \right) L_{p_i}^{|\ell_i|} \left(\frac{2r^2}{\omega_i^2} \right) \\ & \times \mathrm{e}^{-\left(\frac{r^2}{\omega_p^2} + \frac{r^2}{\omega_s^2} + \frac{r^2}{\omega_i^2} \right)} \int_0^{2\pi} d\phi \ \mathrm{e}^{i(\ell_p - \ell_s - \ell_i)\phi} \ , \end{aligned} \tag{A.3}$$

with

$$c_{p,\ell} = \sqrt{\frac{2p!}{\pi(p+|\ell|)!}} \tag{A.4}$$

We can directly calculate the angular integral

$$\int_0^{2\pi} d\phi \ \mathrm{e}^{i(\ell_p - \ell_s - \ell_i)\phi} = 2\pi \ \delta_{\ell_p, \ell_s + \ell_i} \ , \tag{A.5}$$

which gives us the well-known OAM conservation $\ell_p = \ell_s + \ell_i$ in the process of SPDC. Solving the radial integral is rather cumbersome if we include all possible modes with $p \neq 0$. The mode-mixing rules for modes with $p \neq 0$ are discussed in Ref. [81].
For our purpose we are only interested in the OAM of the down-converted photons, which is determined by the indices ℓ only. Therefore we can consider the case for $p_p = p_s = p_i = 0$. The generalized Laguerre polynomials reduce to

$$L_0^{\ell}(x) = 1 \,, \tag{A.6}$$

for any value ℓ.
We then have

$$\begin{aligned}\mathcal{O}_{0,0,0}^{\ell_p,\ell_s,\ell_i} = &\frac{\sqrt{32}\delta_{\ell_p,\ell_s+\ell_i}}{\sqrt{\pi|\ell_p|!|\ell_s|!|\ell_i|!}\,\omega_p\omega_s\omega_i} \\ &\int_0^\infty r\; dr \frac{(\sqrt{2}r)^{|\ell_p|+|\ell_s|+|\ell_i|}}{\omega_p^{|\ell_p|}\omega_s^{|\ell_s|}\omega_i^{|\ell_i|}} \times \mathrm{e}^{-\left(\frac{r^2}{\omega_p^2}+\frac{r^2}{\omega_s^2}+\frac{r^2}{\omega_i^2}\right)} \,.\end{aligned} \tag{A.7}$$

Now we can solve the radial integral. This yields

$$\begin{aligned}\mathcal{O}_{0,0,0}^{\ell_p,\ell_s,\ell_i} = &\sqrt{\frac{8}{\pi}}\delta_{\ell_p,\ell_s+\ell_i}\sqrt{2}^{(|\ell_p|+|\ell_s|+|\ell_i|)}\;\frac{(\frac{1}{2}(|\ell_p|+|\ell_s|+|\ell_i|))!}{\sqrt{|\ell_p|!|\ell_s|!|\ell_i|!}} \\ &\times \frac{\left(\frac{1}{\omega_p^2}+\frac{1}{\omega_s^2}+\frac{1}{\omega_i^2}\right)^{-1-\frac{1}{2}(|\ell_p|+|\ell_s|+|\ell_i|)}}{\omega_p^{|\ell_p|+1}\omega_s^{|\ell_s|+1}\omega_i^{|\ell_i|+1}} \,.\end{aligned} \tag{A.8}$$

To further simplify the expression we can normalize the overlap by the fundamental overlap

$$\mathcal{O}_{0,0,0}^{0,0,0} = \sqrt{\frac{8}{\pi}}\frac{\left(\frac{1}{\omega_p^2}+\frac{1}{\omega_s^2}+\frac{1}{\omega_i^2}\right)^{-1}}{\omega_p\omega_s\omega_i} \,, \tag{A.9}$$

leading to the normalized overlap integral

$$\begin{aligned}\Omega_{0,0,0}^{\ell_p,\ell_s,\ell_i} =&\frac{\mathcal{O}_{0,0,0}^{\ell_p,\ell_s,\ell_i}}{\mathcal{O}_{0,0,0}^{0,0,0}} \\ =&\,\delta_{\ell_p,\ell_s+\ell_i}\sqrt{2}^{(|\ell_p|+|\ell_s|+|\ell_i|)}\;\frac{(\frac{1}{2}(|\ell_p|+|\ell_s|+|\ell_i|))!}{\sqrt{|\ell_p|!|\ell_s|!|\ell_i|!}} \\ &\times \frac{\left(\frac{1}{\omega_p^2}+\frac{1}{\omega_s^2}+\frac{1}{\omega_i^2}\right)^{-\frac{1}{2}(|\ell_p|+|\ell_s|+|\ell_i|)}}{\omega_p^{|\ell_p|}\omega_s^{|\ell_s|}\omega_i^{|\ell_i|}} \,,\end{aligned} \tag{A.10}$$

If we execute the Kronecker-delta we can eliminate one of the three ℓ indices. For example we can substitute $\ell_i = \ell_p - \ell_s$. This substitution yields

$$\Omega_{0,0,0}^{\ell_p,\ell_s,\ell_p-\ell_s} = \sqrt{2}^{(|\ell_p|+|\ell_s|+|\ell_p-\ell_s|)} \frac{(\frac{1}{2}(|\ell_p|+|\ell_s|+|\ell_p-\ell_s|))!}{\sqrt{|\ell_p|!|\ell_s|!|\ell_p-\ell_s|!}} \times \frac{\left(\frac{1}{\omega_p^2}+\frac{1}{\omega_s^2}+\frac{1}{\omega_i^2}\right)^{-\frac{1}{2}(|\ell_p|+|\ell_s|+|\ell_p-\ell_s|)}}{\omega_p^{|\ell_p|}\omega_s^{|\ell_s|}\omega_i^{|\ell_p-\ell_s|}} , \tag{A.11}$$

Because the expression for the overlap integral has several terms including absolute values, this result can only be further simplified by distinguishing different cases for positive and negative values of ℓ_p, ℓ_s and ℓ_i. For example, if signal and idler modes have an OAM rotating in the same direction ($\ell_s \cdot \ell_i \geq 0$) and $|\ell_p| \geq |\ell_s|, |\ell_i|$ we get $|\ell_p| + |\ell_s| + |\ell_p - \ell_s| = 2|\ell_p|$.

For some applications it can be interesting to look at these different cases, but in most of the experiments presented in this work the pump beam has a zero OAM. This means $\ell_p = 0$, which means the vortexes of the down-converted photons are always counter-rotating ($\ell_s \cdot \ell_i < 0$). With $\ell_p = 0$ we get:

$$\Omega_{0,0,0}^{0,\ell_s,-\ell_s} = \sqrt{2}^{2|\ell_s|} \frac{\left(\frac{1}{\omega_p^2}+\frac{1}{\omega_s^2}+\frac{1}{\omega_i^2}\right)^{-|\ell_s|}}{\omega_p\, \omega_s^{|\ell_s|}\omega_i^{|\ell_s|}} . \tag{A.12}$$

When we couple to single mode fiber we fix the size of the beam waists of the signal and idler LG modes. Therefore we can further assume $\omega_s = \omega_i = \omega$ and we get

$$\Omega_{0,0,0}^{0,\ell_s,-\ell_s} = \sqrt{2}^{2|\ell_s|} \frac{\left(\frac{1}{\omega_p^2}+\frac{2}{\omega^2}\right)^{-|\ell_s|}}{\omega_p\, \omega^{2|\ell_s|}} . \tag{A.13}$$

If we look at a more specific example, where the phase matching ($k_p = k_s + k_i$) and the wave-front matching ($z_{R_p} = z_{R_s} = z_{R_i}$ suggest the relationship between the mode widths

$$\frac{1}{\omega_p^2} = \frac{1}{\omega_s^2} + \frac{1}{\omega_i^2} . \tag{A.14}$$

With this we get the normalized overlap integral as:

$$\Omega_{0,0,0}^{0,\ell_s,-\ell_s} = \left(\frac{1}{2}\right)^{|\ell_s|} \frac{1}{\omega_p} . \tag{A.15}$$

With this result we can easily see that the overlap follows a exponential decay for growing values of $|\ell_s|$.
Therefore, for a Gaussian pump with zero OAM ($\ell_p = 0$) the probability of generating two down-converted signal and idler photons with OAM of $\ell_s| = |\ell_i|$ exhibits an exponential decay for increasing values of $|\ell_s|$. This means that we can always identify this with the exponential thermal distribution. If we ignore the factors and include them in the normalization we can identify in this specific case with the assumptions we have made

$$\left(\frac{1}{2}\right)^{|\ell|} = A \cdot \mathrm{e}^{-\beta|\ell|} \tag{A.16}$$

$$\Rightarrow \beta = A \cdot \log(2) \; . \tag{A.17}$$

Without any assumptions on the mode waists we get from eq. (A.12) the inverse temperature of a thermal distribution up to a normalization constant as

$$\beta = \log\left(\frac{1}{2}\left(\frac{1}{\omega_{\mathrm{p}}^2} + \frac{1}{\omega_{\mathrm{s}}^2} + \frac{1}{\omega_{\mathrm{i}}^2}\right) \cdot \omega_{\mathrm{s}}\omega_{\mathrm{i}}\right) \; . \tag{A.18}$$

We see we can change and determine the decay and therefore the inverse temperature of our simulated thermal states by changing the mode widths of the pump, signal and idler beams.

Bibliography

[1] M. Planck, "Über das gesetz der energieverteilung im normalspektrum," *Annalen der Physik*, vol. 309, no. 3, pp. 553–563, 1901.

[2] A. Einstein, "Über einen die erzeugung und verwandlung des lichtes betreffenden heuristischen gesichtspunkt," *Annalen der Physik*, vol. 322, no. 6, pp. 132–148, 1905.

[3] M. Born, E. Wolf, A. B. Bhatia, P. C. Clemmow, D. Gabor, A. R. Stokes, A. M. Taylor, P. A. Wayman, and W. L. Wilcock, *Principles of Optics: Electromagnetic Theory of Propagation, Interference and Diffraction of Light*. Cambridge University Press, 7 ed., 1999.

[4] T. H. Maiman, "Stimulated optical radiation in ruby," *Nature*, vol. 187, pp. 493–494, Aug 1960.

[5] R. Loudon, *The Quantum Theory of Light*. OUP Oxford, 2000.

[6] D. N. Klishko and D. P. Krindach, "Observation of parametric luminescence in a lithium niobate crystal excited by an argon laser," *JETP*, vol. 27, no. 3, p. 371, 1968.

[7] D. C. Burnham and D. L. Weinberg, "Observation of Simultaneity in Parametric Production of Optical Photon Pairs," *Phys. Rev. Lett.*, vol. 25, pp. 84–87, July 1970.

[8] A. Einstein, B. Podolsky, and N. Rosen, "Can quantum-mechanical description of physical reality be considered complete?," *Phys. Rev.*, vol. 47, pp. 777–780, May 1935.

[9] S. Friberg, C. K. Hong, and L. Mandel, "Measurement of time delays in the parametric production of photon pairs," *Phys. Rev. Lett.*, vol. 54, pp. 2011–2013, May 1985.

[10] C. K. Hong and L. Mandel, "Theory of parametric frequency down conversion of light," *Phys. Rev. A*, vol. 31, pp. 2409–2418, Apr. 1985.

[11] R. Ghosh and L. Mandel, “Observation of nonclassical effects in the interference of two photons,” *Phys. Rev. Lett.*, vol. 59, pp. 1903–1905, Oct 1987.

[12] S. Walborn, C. Monken, S. Pádua, and P. S. Ribeiro, “”Spatial correlations in parametric down-conversion,” *Physics Reports*, vol. 495, no. 4, pp. 87 – 139, 2010.

[13] P. H. S. Ribeiro, S. Pádua, J. C. Machado da Silva, and G. A. Barbosa, “Controlling the degree of visibility of young’s fringes with photon coincidence measurements,” *Phys. Rev. A*, vol. 49, pp. 4176–4179, May 1994.

[14] A. M. Yao and M. J. Padgett, “Orbital angular momentum: origins, behavior and applications,” *Adv. Opt. Photon.*, vol. 3, pp. 161–204, June 2011.

[15] M. Padgett and R. Bowman, “Tweezers with a twist,” *Nature Photonics*, vol. 5, no. 6, pp. 343–348, 2011.

[16] A. Mair, A. Vaziri, G. Weihs, and A. Zeilinger, “Entanglement of the orbital angular momentum states of photons,” *Nature*, vol. 412, no. 6844, pp. 313–316, 2001.

[17] A. Vaziri, G. Weihs, and A. Zeilinger, “Experimental Two-Photon, Three-Dimensional Entanglement for Quantum Communication,” *Phys. Rev. Lett.*, vol. 89, p. 240401, Nov 2002.

[18] J. H. Poynting, “The wave motion of a revolving shaft, and a suggestion as to the angular momentum in a beam of circularly polarised light,” *Proceedings of the Royal Society of London A: Mathematical, Physical and Engineering Sciences*, vol. 82, no. 557, pp. 560–567, 1909.

[19] L. Allen, M. W. Beijersbergen, R. J. C. Spreeuw, and J. P. Woerdman, “Orbital angular momentum of light and the transformation of Laguerre-Gaussian laser modes,” *Phys. Rev. A*, vol. 45, pp. 8185–8189, June 1992.

[20] G. Gibson, J. Courtial, M. J. Padgett, M. Vasnetsov, V. Pas’ko, S. M. Barnett, and S. Franke-Arnold, “Free-space information transfer using light beams carrying orbital angular momentum,” *Opt. Express*, vol. 12, pp. 5448–5456, Nov 2004.

[21] R. Chen, H. Zhou, M. Moretti, X. Wang, and J. Li, “Orbital angular momentum waves: Generation, detection, and emerging applications,” *IEEE Communications Surveys Tutorials*, vol. 22, no. 2, pp. 840–868, 2020.

[22] J. Anders and M. Esposito, “Focus on quantum thermodynamics,” *New Journal of Physics*, vol. 19, p. 010201, jan 2017.

[23] G. L. Zanin, T. Häffner, M. A. A. Talarico, E. I. Duzzioni, P. H. S. Ribeiro, G. T. Landi, and L. C. Céleri, "Experimental Quantum Thermodynamics with Linear Optics," *Brazilian Journal of Physics*, vol. 49, pp. 783–798, Oct 2019.

[24] R. M. de Araújo, T. Häffner, R. Bernardi, D. S. Tasca, M. P. J. Lavery, M. J. Padgett, A. Kanaan, L. C. Céleri, and P. H. S. Ribeiro, "Experimental study of quantum thermodynamics using optical vortices," *Journal of Physics Communications*, vol. 2, no. 3, p. 035012, 2018.

[25] P. H. S. Ribeiro, T. Häffner, G. L. Zanin, N. R. da Silva, R. M. de Araújo, W. C. Soares, R. J. de Assis, L. C. Céleri, and A. Forbes, "Experimental study of the generalized jarzynski fluctuation relation using entangled photons," *Phys. Rev. A*, vol. 101, p. 052113, May 2020.

[26] C. Jarzynski, "Nonequilibrium Equality for Free Energy Differences," *Phys. Rev. Lett.*, vol. 78, pp. 2690–2693, Apr 1997.

[27] H. Tasaki, "Jarzynski Relations for Quantum Systems and Some Applications," *eprint arXiv:cond-mat/0009244*, sep 2000.

[28] F. Tacchino, A. Auffèves, M. F. Santos, and D. Gerace, "Steady state entanglement beyond thermal limits," *Phys. Rev. Lett.*, vol. 120, p. 063604, Feb 2018.

[29] K. Micadei, J. P. S. Peterson, A. M. Souza, R. S. Sarthour, I. S. Oliveira, G. T. Landi, T. B. Batalhão, R. M. Serra, and E. Lutz, "Reversing the direction of heat flow using quantum correlations," *Nature Communications*, vol. 10, no. 1, p. 2456, 2019.

[30] J. P. Santos, L. C. Céleri, G. T. Landi, and M. Paternostro, "The role of quantum coherence in non-equilibrium entropy production," *npj Quantum Information*, vol. 5, no. 1, p. 23, 2019.

[31] F. T. Arecchi, "Measurement of the statistical distribution of gaussian and laser sources," *Phys. Rev. Lett.*, vol. 15, pp. 912–916, Dec 1965.

[32] G. Fowles, *Introduction to Modern Optics*. Dover Books on Physics Series, Dover Publications, 1975.

[33] B. E. A. Saleh and M. C. Teich, *Fundamentals of Photonics*. John Wiley and Sons, Inc., 2001.

[34] O. Svelto, *Principles of Lasers*. Springer US, 1976.

[35] M. Beijersbergen, L. Allen, H. van der Veen, and J. Woerdman, “Astigmatic laser mode converters and transfer of orbital angular momentum,” *Optics Communications*, vol. 96, no. 1, pp. 123 – 132, 1993.

[36] M. Padgett and L. Allen, “Light with a twist in its tail,” *Contemporary Physics*, vol. 41, no. 5, pp. 275–285, 2000.

[37] I. Kimel and L. R. Elias, “Relations between hermite and laguerre gaussian modes,” *IEEE Journal of Quantum Electronics*, vol. 29, pp. 2562–2567, Sept. 1993.

[38] M. A. Bandres and J. C. Gutiérrez-Vega, “Ince–gaussian beams,” *Opt. Lett.*, vol. 29, pp. 144–146, Jan. 2004.

[39] J. Arlt and K. Dholakia, “Generation of high-order bessel beams by use of an axicon,” *Optics Communications*, vol. 177, no. 1, pp. 297 – 301, 2000.

[40] H. J. Metcalf and P. van der Straten, *Laser Cooling and Trapping*. No. XVI in Graduate Texts in Contemporary Physics, Springer, New York, NY, 1999.

[41] R. A. Beth, “Mechanical detection and measurement of the angular momentum of light,” *Phys. Rev.*, vol. 50, pp. 115–125, Jul 1936.

[42] K. Gottfried and T.-M. Yan, *Quantum Mechanics: Fundamentals*. No. XVIII in Graduate Texts in Contemporary Physics, Springer, New York, NY, 1966.

[43] J. D. Jackson, *Classical electrodynamics; 2nd ed.* New York, NY: Wiley, 1975.

[44] J. W. Simmons and M. J. Guttmann, *States, waves, and photons: A modern introduction to light.* Addison-Wesley series in physics, Reading, Mass.: Addison-Wesley Pub. Co., 1970.

[45] L. Allen, M. Padgett, and M. Babiker, “Iv the orbital angular momentum of light,” in *Progress in Optics* (E. Wolf, ed.), vol. 39 of *Progress in Optics*, pp. 291–372, Elsevier, 1999.

[46] D. McGloin and K. Dholakia, “Bessel beams: Diffraction in a new light,” *Contemporary Physics*, vol. 46, no. 1, pp. 15–28, 2005.

[47] J. C. Gutiérrez-Vega, M. D. Iturbe-Castillo, and S. Chávez-Cerda, “Alternative formulation for invariant optical fields: Mathieu beams,” *Opt. Lett.*, vol. 25, pp. 1493–1495, Oct 2000.

[48] J. F. Nye and M. V. Berry, “Dislocations in wave trains,” *Proc. R. Soc. Lond. A*, vol. 336, pp. 165 – 190, 1974.

[49] M. Beijersbergen, R. Coerwinkel, M. Kristensen, and J. Woerdman, “Helical-wavefront laser beams produced with a spiral phaseplate,” *Optics Communications*, vol. 112, no. 5, pp. 321–327, 1994.

[50] V. Bazhenov, M. Vasnetsov, and M. Soskin, “Laser beams with screw dislocations in their wavefronts,” *JETP. Lett*, vol. 52, pp. 429–431, 01 1990.

[51] N. B. Simpson, K. Dholakia, L. Allen, and M. J. Padgett, “Mechanical equivalence of spin and orbital angular momentum of light: an optical spanner,” *Opt. Lett.*, vol. 22, pp. 52–54, Jan 1997.

[52] B. Jack, J. Leach, J. Romero, S. Franke-Arnold, M. Ritsch-Marte, S. M. Barnett, and M. J. Padgett, “Holographic ghost imaging and the violation of a bell inequality,” *Phys. Rev. Lett.*, vol. 103, p. 083602, Aug 2009.

[53] L. Torner, J. P. Torres, and S. Carrasco, “Digital spiral imaging,” *Opt. Express*, vol. 13, pp. 873–881, Feb 2005.

[54] S. Bernet, A. Jesacher, S. Fürhapter, C. Maurer, and M. Ritsch-Marte, “Quantitative imaging of complex samples by spiral phase contrast microscopy,” *Opt. Express*, vol. 14, pp. 3792–3805, May 2006.

[55] S. Fürhapter, A. Jesacher, S. Bernet, and M. Ritsch-Marte, “Spiral phase contrast imaging in microscopy,” *Opt. Express*, vol. 13, pp. 689–694, Feb 2005.

[56] S. Fürhapter, A. Jesacher, S. Bernet, and M. Ritsch-Marte, “Spiral interferometry,” *Opt. Lett.*, vol. 30, pp. 1953–1955, Aug 2005.

[57] L. T. Juan P. Torres, *Twisted Photons: Applications of Light with Orbital Angular Momentum*. Wiley-VCH, 1 ed., 2011.

[58] L. Gong, Q. Zhao, H. Zhang, X.-Y. Hu, K. Huang, J.-M. Yang, and Y.-M. Li, “Optical orbital-angular-momentum-multiplexed data transmission under high scattering,” *Light: Science & Applications*, vol. 8, p. 27, Mar 2019.

[59] A. Vaziri, J.-W. Pan, T. Jennewein, G. Weihs, and A. Zeilinger, “Concentration of higher dimensional entanglement: Qutrits of photon orbital angular momentum,” *Phys. Rev. Lett.*, vol. 91, p. 227902, Nov 2003.

[60] J. C. Garcia-Escartin and P. Chamorro-Posada, “Quantum computer networks with the orbital angular momentum of light,” *Phys. Rev. A*, vol. 86, p. 032334, Sep 2012.

[61] G. Nienhuis, “Analogies between optical and quantum mechanical angular momentum,” *Philosophical Transactions of the Royal Society A: Mathematical, Physical and Engineering Sciences*, vol. 375, no. 2087, p. 20150443, 2017.

[62] S. M. Barnett, M. Babiker, and M. J. Padgett, “Optical orbital angular momentum,” *Philosophical Transactions of the Royal Society A: Mathematical, Physical and Engineering Sciences*, vol. 375, no. 2087, p. 20150444, 2017.

[63] G. Nienhuis and J. Visser, “Angular momentum and vortices in paraxial beams,” *Journal of Optics A: Pure and Applied Optics*, vol. 6, pp. S248–S250, apr 2004.

[64] J. Arlt, K. Dholakia, L. Allen, and M. J. Padgett, “The production of multiringed laguerre–gaussian modes by computer-generated holograms,” *Journal of Modern Optics*, vol. 45, no. 6, pp. 1231–1237, 1998.

[65] J. A. Davis, D. M. Cottrell, J. Campos, M. J. Yzuel, and I. Moreno, “Encoding amplitude information onto phase-only filters,” *Appl. Opt.*, vol. 38, pp. 5004–5013, Aug. 1999.

[66] G. C. G. Berkhout, M. P. J. Lavery, J. Courtial, M. W. Beijersbergen, and M. J. Padgett, “Efficient Sorting of Orbital Angular Momentum States of Light,” *Phys. Rev. Lett.*, vol. 105, p. 153601, Oct 2010.

[67] Y. Wen, I. Chremmos, Y. Chen, J. Zhu, Y. Zhang, and S. Yu, “Spiral transformation for high-resolution and efficient sorting of optical vortex modes,” *Phys. Rev. Lett.*, vol. 120, p. 193904, May 2018.

[68] A. Zeilinger, *Dance of the Photons: From Einstein to Quantum Teleportation*. Farrar, Straus and Giroux, 2010.

[69] A. Zavatta, S. Viciani, and M. Bellini, “Tomographic reconstruction of the single-photon Fock state by high-frequency homodyne detection,” *Phys. Rev. A*, vol. 70, p. 053821, Nov. 2004.

[70] M. Beck, *Quantum Mechanics: Theory and Experiment*. OUP USA, 2012.

[71] M. Avenhaus, M. Chekhova, L. Krivitsky, G. Leuchs, and C. Silberhorn, “Experimental verification of high spectral entanglement for pulsed waveguided

spontaneous parametric down-conversion," *Physical Review A (Atomic, Molecular and Optical Physics)*, vol. 79, no. 4, p. 043836, 2009. Copyright 2009 American Physical Society.

[72] X. Guo, C.-l. Zou, C. Schuck, H. Jung, R. Cheng, and H. X. Tang, "Parametric down-conversion photon-pair source on a nanophotonic chip," *Light: Science & Applications*, vol. 6, no. 5, pp. e16249–e16249, 2017.

[73] S. P. Walborn, D. S. Lemelle, M. P. Almeida, and P. H. S. Ribeiro, "Quantum key distribution with higher-order alphabets using spatially encoded qudits," *Phys. Rev. Lett.*, vol. 96, p. 090501, Mar. 2006.

[74] P. H. Souto Ribeiro and G. A. Barbosa, "Direct and ghost interference in double-slit experiments with coincidence measurements," *Phys. Rev. A*, vol. 54, pp. 3489–3492, Oct. 1996.

[75] C. H. Monken, P. H. S. Ribeiro, and S. Pádua, "Transfer of angular spectrum and image formation in spontaneous parametric down-conversion," *Phys. Rev. A*, vol. 57, pp. 3123–3126, Apr. 1998.

[76] L. Zhang, C. Silberhorn, and I. A. Walmsley, "Secure quantum key distribution using continuous variables of single photons," *Phys. Rev. Lett.*, vol. 100, p. 110504, Mar. 2008.

[77] M. Krenn, M. Malik, M. Erhard, and A. Zeilinger, "Orbital angular momentum of photons and the entanglement of laguerre–gaussian modes," *Philosophical Transactions of the Royal Society A: Mathematical, Physical and Engineering Sciences*, vol. 375, no. 2087, p. 20150442, 2017.

[78] F. M. Miatto, A. M. Yao, and S. M. Barnett, "Full characterization of the quantum spiral bandwidth of entangled biphotons," *Phys. Rev. A*, vol. 83, p. 033816, Mar. 2011.

[79] S. Franke-Arnold, S. M. Barnett, M. J. Padgett, and L. Allen, "Two-photon entanglement of orbital angular momentum states," *Phys. Rev. A*, vol. 65, p. 033823, Feb. 2002.

[80] J. P. Torres, A. Alexandrescu, and L. Torner, "Quantum spiral bandwidth of entangled two-photon states," *Phys. Rev. A*, vol. 68, p. 050301, Nov. 2003.

[81] L. J. Pereira, W. T. Buono, D. S. Tasca, K. Dechoum, and A. Z. Khoury, "Orbital-angular-momentum mixing in type-ii second-harmonic generation," *Phys. Rev. A*, vol. 96, p. 053856, Nov 2017.

[82] M. Planck, "Zur Theorie der Wärmestrahlung," *Annalen der Physik*, vol. 4, 1910.

[83] S. N. Bose and A. Eisntein, "Plancks Gesetz und Lichtquantenhypothese," *Zeitschrift für Physik*, vol. 26, 1924.

[84] G. M. D.F. Walls, *Quantum Optics*. Springer-Verlag Berlin Heidelberg, 1994.

[85] Y. Wen, I. Chremmos, Y. Chen, Y. Zhang, and S. Yu, "Arbitrary multiplication and division of the orbital angular momentum of light," *Phys. Rev. Lett.*, vol. 124, p. 213901, May 2020.

[86] F. Roddier, "V the effects of atmospheric turbulence in optical astronomy," in *Progress in Optics* (E. Wolf, ed.), vol. 19 of *Progress in Optics*, pp. 281 – 376, Elsevier, 1981.

[87] A. N. Kolmogorov, V. Levin, J. C. R. Hunt, O. M. Phillips, and D. Williams, "The local structure of turbulence in incompressible viscous fluid for very large reynolds numbers," *Proceedings of the Royal Society of London. Series A: Mathematical and Physical Sciences*, vol. 434, no. 1890, pp. 9–13, 1991.

[88] D. L. Fried, "Statistics of a geometric representation of wavefront distortion," *J. Opt. Soc. Am.*, vol. 55, pp. 1427–1435, Nov. 1965.

[89] A. Hamadou Ibrahim, F. S. Roux, M. McLaren, T. Konrad, and A. Forbes, "Orbital-angular-momentum entanglement in turbulence," *Phys. Rev. A*, vol. 88, p. 012312, July 2013.

[90] B. Rodenburg, M. Mirhosseini, M. Malik, O. S. Magaña-Loaiza, M. Yanakas, L. Maher, N. K. Steinhoff, G. A. Tyler, and R. W. Boyd, "Simulating thick atmospheric turbulence in the lab with application to orbital angular momentum communication," *New Journal of Physics*, vol. 16, p. 033020, Mar. 2014.

[91] B.-J. Pors, C. H. Monken, E. R. Eliel, and J. P. Woerdman, "Transport of orbital-angular-momentum entanglement through a turbulent atmosphere," *Opt. Express*, vol. 19, pp. 6671–6683, Mar. 2011.

[92] B. Gaveau, L. Granger, M. Moreau, and L. S. Schulman, “Relative entropy, interaction energy and the nature of dissipation,” *Entropy*, vol. 16, no. 6, pp. 3173–3206, 2014.

[93] G. E. Crooks, “Nonequilibrium Measurements of Free Energy Differences for Microscopically Reversible Markovian Systems,” *Journal of Statistical Physics*, vol. 90, pp. 1481–1487, Mar 1998.

[94] A. E. Rastegin and K. Życzkowski, “Jarzynski equality for quantum stochastic maps,” *Phys. Rev. E*, vol. 89, p. 012127, Jan 2014.